Doctoral Dissertation

Study on advanced evaluation methods of fatigue strength for welded structures of LNG carriers and LNG fuel ships

（LNG 運搬船および LNG 燃料推進船における溶接構造部の疲労強度評価法の高度化）

Toru Shiratsuchi

July 2020

Graduate School of Engineering,

Osaka University

Contents

List of Abbreviations and Symbols

Abbreviations

ABS	American Bureau of Shipping
FAT	Classificaton reference to S-N curve in IIW recommendations
HAZ	Heat Affected Zone
HSS	Hot Spot Stress
IIW	International Institute of Welding
IMO	International Maritime Organization
JSSC	Japanese Society of Steel Construction
LNG	Liquefied Natural Gas
SWT	Smith-Watson-Topper

Symbols

a	Crack length
α	Stress concentration factor
b	Half crack width
β	Fatigue notch factor
C	Constant in equation of S-N curve with exponent m
c	Crack depth
χ	Stress gradient
χ^*	Relative stress gradient

CI	Confidence interval
d	Weld leg length
ΔK	Stress intensity factor range
$\Delta\sigma$	Stress range
$\Delta\sigma_{exp}$	Fatigue strength at 2×10^6cycle of fatigue data
$\Delta\sigma_{HSS}$	Hot spot stress range
$\Delta\sigma_n$	Nominal stress range
$\Delta\sigma_{pre}$	Predicted fatigue strength at 2×10^6cycle
E	Young's modulus
G	Geometric effect function
H	Attached plate height
h_i	Function on Siebel diagram for each material
k	Gusset length
$K_{\max}$	Maximum stress intensity factor
L	Sum of weld leg length and attached plate thickness
Λ	Constant in relation between stress range and main plate thickness with exponent n
m	Exponent of S-N curve
N	Number of cycles
n	Thickness correction exponent
ν	Poisson's ratio
N_f	Number of cycles to failure

p	Sample number
PI	Prediction interval
θ	Flank angle
R	Stress ratio
ρ	Weld toe radius
S^2	Sample variance
σ_{max}	Peak stress at a notch or weld toe
σ_n	Nominal stress
σ_{w0}	Fatigue limit of smooth specimens
σ_{wk}	Fatigue limit of noched specimens
σ_{wr}	Fatigue limit for smooth specimens with residual stress equal to welded joints
σ_{ww}	Fatigue limit for welded joints
t	Main plate thickness
t_{eff}	Effective thickness
t_p	Attached plate thickness
$T_{p\text{-}1}$	Student's t-distribution with $p - 1$ degrees of freedom
t_{ref}	Reference thickness
W	Main plate width

Chapter 1 Introduction

1.1 Background

The International Maritime Organization (IMO) divides types of liquefied natural gas (LNG) tank for ship into independent tanks and membrane tanks. Independent tanks are divided into Type A, Type B, and Type C. Type A and Type B tanks are non-pressurize tanks. Type A tanks employ a full secondary barrier. Type B tanks are permitted to adopt a reduced secondary barrier, since Type B tank are required refined stress analysis, fatigue life and fatigue crack propagation assessments [1, 2]. Thus, Type B tanks have high reliability on long term operation. The most common shape of Type B tank is a spherical shape tank, as shown in Fig. 1.1 [3, 4].

There is growing interest in LNG fuel ships, as shown in Fig1.2, to deal with the emission control requirements for ships by IMO. Figure1.3 shows the LNG fuel ship with the Type-B independent prismatic tank, which provides high volume efficiency.

Type B tanks are welded structures, similar to ship structures. Fatigue strength of welded structures are lower than that of un-notched parent materials, because welded structures include local stress concentration at weld toe, and welding residual stress. Fatigue strength assessment of welded joints is important for design of Type B tanks, since fatigue strength assessment is one of the basis of high reliability of Type B tanks. Some guides [1, 2] describe fatigue strength assessment for welded joints in Type B tanks. Table 1.1 lists guides for fatigue strength assessment for welded joints in Type B tanks, and guides, recommendations, and standard (hereinafter, these are called “guides”) for fatigue strength assessment for welded joint in ship structures or general welded structures [8-14]. Table 1.1 also lists stress types, which can be adopted fatigue strength assessment of welded joints. Almost the guides describe both

the nominal stress approach and the hot spot stress (HSS) approach. The HSS includes the stress raising effect of structural discontinuities, excluding localized notch stress due to weld toe.

Fatigue strength of welded joints are represented in terms of the S-N curves, which are the relationships between the number of cycles to failure and applied stress range. In the nominal stress approach, the design S-N curves are classified based on structural detail. The hot spot design S-N curves are expressed by a few curves, because the HSS includes the stress raising effect of structural discontinuities. The guides describe design S-N curves. Fatigue strength of welded joints is influenced by many factors, e.g. geometry, mean stress, material properties, environment, temperature, and post-weld treatment. Almost the guides consider these effects.

The cryogenic metallic materials, such as aluminum alloy (5083-O), nickel alloy steel (9 % Ni steel), and stainless steel (SUS304 stainless steel) are candidate materials for type B tanks, because these materials has superior fracture toughness at cryogenic temperatures. To achieve excellent structural safety of type B tanks, it is necessary to accurate assess the fatigue strength for welded joints of these material.

However, there are cases when design S-N curve for aluminum welded joints gives un-conservative assessment [15]. Moreover, the importance of the consideration of the thickness effect for aluminum welded joints even if main plate thickness is less than 25 mm, which is outside the scope of the thickness effect of guides, has been pointed out [16].

Although the guides gives the consideration method of the thickness effect on fatigue strength for welded joints, the bead profile effect including weld toe radius is NOT described in the guides, regardless type of parent material. It is important that the consideration of the

bead profile effect, since bead profile affect stress field around weld toe.

There are experimental studies on fatigue strength of 9% Ni steel welded joint [17-22]. However, the effects of many factors, e.g. geometry, mean stress, material properties, on fatigue strength for 9% Ni steel welded joints are NOT clarified. It is difficult to clarify these effects especially effects of mean stress and material properties, since 9% Ni steel welded joints have following features:

- 9% Ni steel shows the phase transformation during the welding (heating) and cooling process.
- 70% Ni alloy is usually adopted as weld metal for 9% Ni steel welded joints. Mechanical properties of 70% Ni are differ from that of 9% Ni steel.

  70% Ni alloy does not show the phase transformation during the welding (heating) and cooling process.

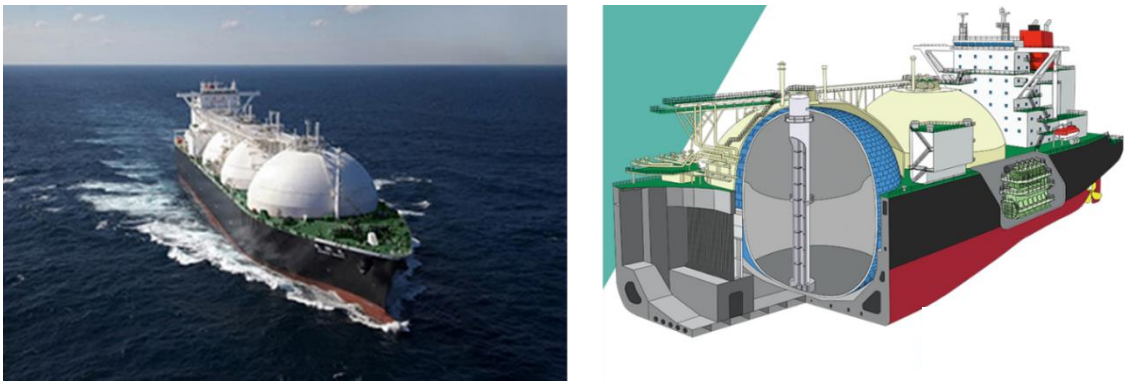

Fig. 1.1. LNG carrier with spherical shape Type B tank [3, 4].

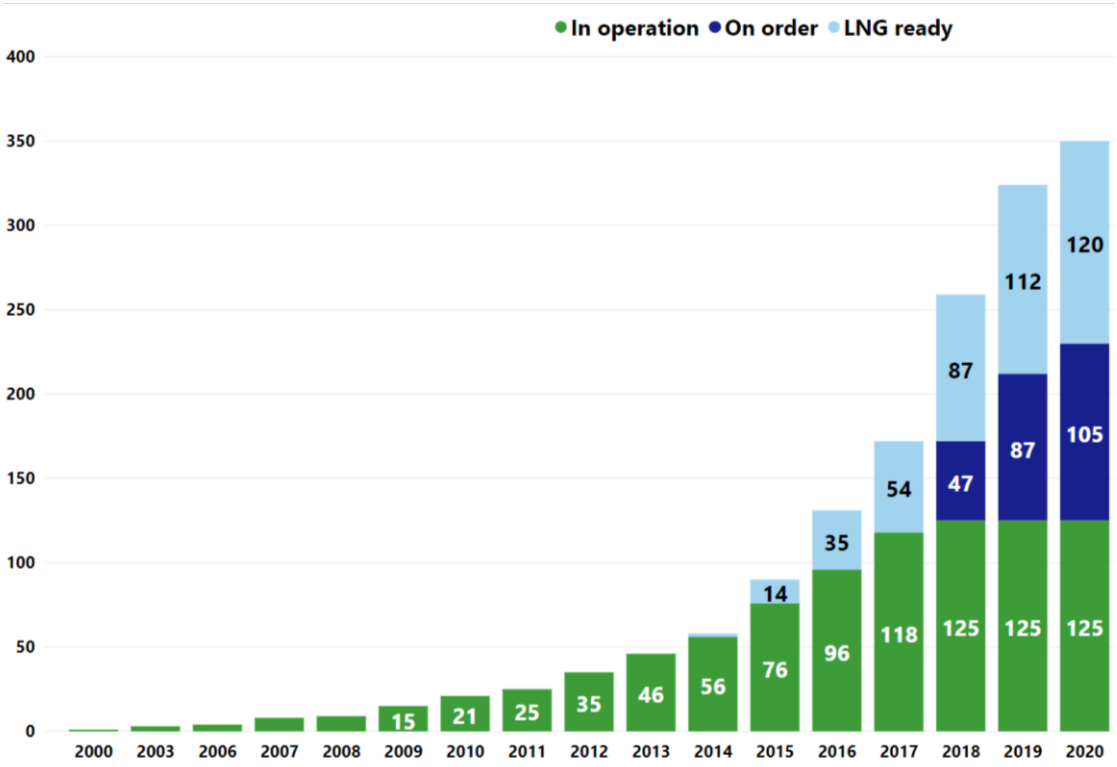

Fig. 1.2. Number of LNG fuel ship [5].

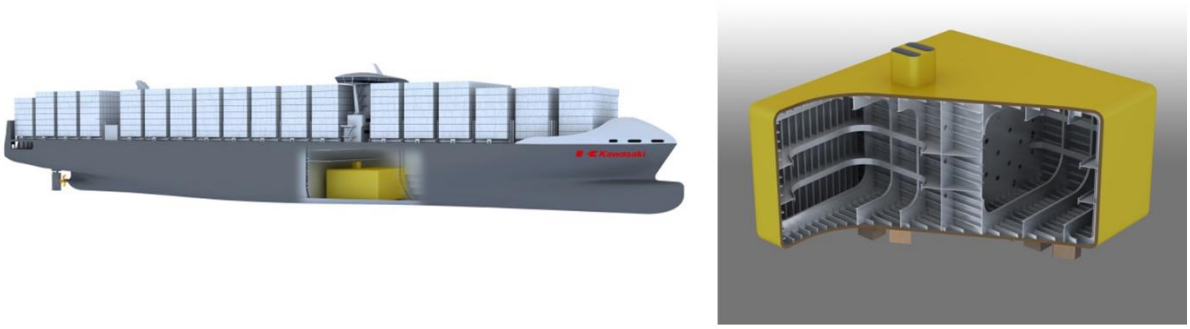

Fig. 1.3. LNG fuel ship with the Type-B independent prismatic tank [6, 7].

Table 1.1 Guides or recommendations for fatigue strength assessment for welded joints

	Stress type			Subject
	Nominal	HSS	Effective notch	
ABS guides [1]	✔	✔		Independent tanks
Lloyd's Register. Guidance notes [2]	✔	✔		Type B tanks
DNVGL-CG-0129 [8]	✔	✔		Ship structures
DNVGL-RP-C203 [9]	✔	✔	✔	Offshore steel structures
IIW recommendations [10]	✔	✔	✔	Welded structures
Eurocode 3 Part1-9 [11]	✔	✔		Steel structures
Eurocode 9 Part1-3 [12]	✔	✔		Aluminum structures
BS7608 [13]	✔	✔		Steel structures
JSSC [14]	✔	✔		Steel structures

1.2 Review of literature

1.2.1 Hot Spot S-N curves for welded aluminum joints

The Eurocode 9, the IIW recommendations, and the ABS guide describe the assessment of fatigue strength for aluminum welded joints. To the best of the author's knowledge, the IIW recommendations and the ABS guide give the design S-N curves on the basis of the HSS for welded aluminum joints. In the IIW recommendations, the fatigue strength class of the hot spot design S-N curve for butt welded joints and non- or partially load-carrying fillet welded joints is FAT 40 (FAT refers to the characteristic stress range at 2 million cycles), and that for load-carrying joints is FAT36.

The thickness effect is a decrease in the fatigue strength with an increase in the main plate thickness [23]. The cause of thickness effect is raising local stress at the weld toe with an increase in the main plate thickness. In the IIW recommendation, the thickness effect is considered in the case of the main plate thickness over 25 mm, the same as welded steel structures.

There exist much literature on fatigue strength of welded aluminum joints. Ribeiro, de Jesus and Feup [24] conduct fatigue test for butt welded joint and three types of fillet welded joints, and investigate prediction method of fatigue life for welded aluminum joints. Bloem et al. [25] propose models for mechanical response of welded aluminum joints under fatigue loading. Coughlin and Walbridge [26] summarize an investigation conducted to examine the fatigue behavior of aluminum welds under in-service highway bridge loading conditions.

Partanen and Niemi [27] report fatigue test results of welded aluminum joints with the main plate thickness up to 6 mm. The joint types in the reference [27] are butt welded joints, lap welded joints, non-load-carrying fillet welded joints, and panel welded model. They mention that the hot spot design S-N curve of the IIW recommendations is suitable. On the other hand, Tveiten, Xiaozhi and Berge [15] indicate that the fatigue strength of the welded aluminum ship structure model with main plate thickness of 10 mm was lower than the hot spot design S-N curve of the IIW recommendations. Zamzami and Susmel [28] investigated fatigue strength of welded aluminum joints which are non-load-carrying cruciform joints, non-load-carrying Tee joints, and load-carrying cruciform joints. They concluded that the hot spot design S-N curve of the IIW recommendations is at an adequate level of conservatism; however, the thickness effect for the HSS approach is not considered. Maddox [16] conducted fatigue tests for non-load carrying cruciform joints with main plate thickness between 3 and 24 mm, and pointed out that considering the thickness effect is the necessary even if main plate thickness is less than 25 mm.

1.2.2 Thickness and bead profile effects on fatigue strength of welded joints

Gurney [23] for the first time reported the thickness effect of fatigue strength for welded joints based on an analytical method of fracture mechanics. Johnston [29] carried out fatigue tests for non-load-carrying cruciform joints with different plate thicknesses, indicating a decreasing trend of fatigue strength alongside an increase in main plate thickness. Gurney [30] investigated existing fatigue test data and illustrated a double logarithmic linear relationship between fatigue strength and main plate thickness. A significant body of literature exists on the thickness effect of fatigue strength for welded joints [31-35].

Gurney [36] indicated the effect of weld leg length on the fatigue strength of welded cruciform joints via fatigue crack growth analysis, assuming that an initial crack existed at the weld toe, as well as the thickness effect. However, weld toe radius was not considered in this analysis. Zerbst et al. [37] presented a method for determining the fatigue strength of welded joints by fracture mechanics. This method called the IBESS method can be considered the geometric effect including weld toe radius. The acronym IBESS stands for “Integrale Bruchmechanische Ermittlung der Schwingfestigkeit von Schweißverbindungen“ which means integral fracture mechanics determination of the fatigue strength of welded joints. However, prediction results based on this method indicate over-conservative or non-conservative estimations for cruciform welded joints and out-of-plane gusset joints. The reasons for these results have to date not been clearly identified.

With a focus on the relationship between stress gradient and stress concentration factor, Yamamoto et al. [38] and Tatsuta et al. [39] studied geometric effect on fatigue strength for welded joints, including weld bead profiles. They pointed out that weld toe radius affects the

relationship between stress gradient and stress concentration factor. However, the effect of weld toe radius was not investigated in detail.

1.2.3 Fatigue strength for 9 % Ni steel welded joints

ABS guide [1] describes the design S-N curves for 9% Ni steel welded joints. Many experiments were conducted on the fatigue strength of 9% Ni steel welded joints [17, 18–22]. Gioielli et al. [18, 19] presented fatigue test results for typical welded joints of 9% Ni steel. Lee et al. [17] showed the improvement rates of fatigue life at LNG temperatures compared to room temperature. Tsunenari [20] studied the influence of welding distortion for fatigue strength on 9% Ni steel welded joint. Kishimoto [21] investigated the effect of undercut for fatigue strength on 9% Ni steel.

To investigate the effects of many factors, e.g. geometry, mean stress, material properties, on fatigue strength for 9% Ni steel welded joints, use of the fatigue life prediction method is an effective means. Lawrence et al. [40] reported assessment of fatigue crack initiation life for steel welded joints by focusing on local strain at the weld toe. Similarly, Usami et al. [41] reported about the fatigue crack initiation life of steel welded joints. These references, however, did not consider the details of welding residual stress distribution. Teng et al. [42] investigated the mean stress correction method for crack initiation fatigue life. They pointed out that the Smith-Watson-Topper (SWT) mean stress correction approach [43] approximates experimental data better than the Manson-Halford correction [44], which is the modified Morrow correction [45]. Levieil et al. [46] applied the Morrow criterion to show the assessment results of the fatigue crack initiation life for steel welded T-joints. Some results indicated over-

conservative estimations compared with experimental results. Ince et al. [47] investigated the prediction capabilities of Morrow correction and SWT approach for parent materials. They revealed that the prediction results using the SWT approach is good agreement with the experimental results of parent materials. Ladinek et al. [48] assessed the fatigue crack initiation life for steel welded test specimens by considering the real weld geometry. They obtained the weld geometry by using a 3D laser scanner. Hiraide et al. [49] simulated the stress-strain behavior for a steel welded joint under fatigue loading. This study considered the effect of the stress-strain response of HAZ. Tsutsumi et al. [50] investigated fatigue crack initiation life of welded joints via weld pool analysis and cyclic plasticity stress analysis, and discuss the effects of bead shape and thermal history.

Maddox [51] investigated fatigue crack propagation for a semi-elliptical surface crack at the toe of a longitudinal non-load-carrying gussets fillet steel weld. Gurney [36] described the effect of the weld leg length on the fatigue strength of steel welded cruciform joints by using fatigue crack growth analysis, assuming that an initial crack existed at the weld toe. Gadallah et al. [52] studied the effect of welding residual stress on the stress intensity factor and fatigue crack propagation.

Itoh et al. [53] showed the prediction results of the crack initiation life and the crack propagation life for steel butt welded joint. However, they did not consider the detail of welding residual stress distribution and the effect of the cyclic stress-strain property of HAZ. Zerbst et al. [54] proposed a method to determine the fatigue strength of steel welded joints based on fracture mechanics. The prediction results based on this method indicate over-conservative or non-conservative estimations for typical steel welded joints. The reasons for these results have

to date not been clearly identified. Tsutsumi et al. [55] examined the effects of bead shape and over-load on fatigue crack initiation and fatigue crack propagation for steel welded joints via thermal elastic-plastic analysis and stress analysis under fatigue loading, however, the mean stress effect on the characteristic curves of fatigue crack initiation life and fatigue crack propagation was not considered. Tsutsumi et al. [56] studied the fatigue life prediction for the root fracture the steel welded joint. This prediction was not considered the effect of welding residual stress distribution.

1.3 Problem statement

The thickness effect for welded aluminum joints based on HSS is not sufficiently clarified. To appropriately assess fatigue strength by the HSS approach for welded aluminum joints, further studies for the thickness effect are needed.

The geometric effect, which include thickness and bead profile effect, is not clear quantitatively, even for typical joint types made by steel.

There exists literature on investigation of each effect, which are mean stress effect, material properties effect, thickness effect, for fatigue strength of welded joints. However, to the best of the author's knowledge, no reports have comprehensively considered these effects on prediction of fatigue life for 9% Ni steel welded joints.

1.4 Objectives and Structure

Objectives of this study is proposing simplified engineering estimation methods for the thickness effect on Hot spot S-N curves for welded aluminum joints, and the geometric

effect on fatigue strength of welded joints regardless type of parent material. In addition, an estimation model of fatigue life for 9% Ni welded joints, which can be comprehensively considered the geometric effect, the material properties effect, and the mean stress effect, is proposed.

The present study is divided into six chapters; below is detailed the structure of this study:

Chapter 1 briefly gives the background on an importance of fatigue strength assessment for welded joints in LNG type B tanks and ship structures. A review of literature on many effects of fatigue strength for welded joints is also conducted. Objective and structure of this thesis are also addressed.

Chapter 2 presents the proposed HSS design S-N curve, which include the thickness effect, for aluminum welded joints. The proposed design S-N curve is based on experimental data. Additionally, the validity of the proposed hot spot design S-N curve was evaluated by comparing the fatigue test data of welded joint specimens and large scale model.

Chapter 3 presents the proposed estimation model for the geometric effect, which includes the thickness effect and bead profile effect, on fatigue strength of welded joints. The proposed model is based on the relative stress gradient and the stress concentration factor at weld toe. The validity of the proposed method was tested by comparing it with fatigue test data reported in the literatures.

Chapter 4 presents the proposed fatigue life prediction method of 9% Ni steel welded joints, which is considered the geometric effect, difference of cyclic stress-strain properties between parent material, HAZ, and weld metal, and the mean stress effect by welding residual

stress and applied stress. The proposed fatigue life prediction method for welded joints can successfully predict the fatigue life of 9% Ni steel butt welded joints.

Chapter 5 presents fatigue behavior and fatigue life of 9 % Ni steel cruciform welded joints. Fatigue life for 9 % Ni steel cruciform welded joints was predicted using proposed fatigue life prediction method of welded joints in chapter 4.

Chapter 6 summarizes the conclusions as well as the contributions in this study. Also, recommendations for further works.

Chapter 2 Thickness effect of Hot Spot S-N curves for welded aluminum joints

2.1 Introduction

The hot spot stress (HSS) includes the stress raising effect of structural discontinuities, excluding localized notch stress due to weld toe. The HSS depends on macro-structural effects and loading conditions. The fatigue strength assessment at weld toe based on the HSS approach is typically used where nominal stress is not clearly defined because of complex structural effect, or where the classification of the welded joint is difficult. The HSS approach is widely used for fatigue strength assessments of welded steel structures.

The Eurocode 9 [12], the International Institute of Welding (IIW) recommendations [10], and the guide for building and classing for liquefied gas carriers with independent tanks (American Bureau of Shipping (ABS)) [1] describe the assessment of fatigue strength for aluminum welded joints. To the best of the author's knowledge, the IIW recommendations and the ABS guide give the design S-N curves on the basis of the HSS for welded aluminum joints. In the IIW recommendations, the fatigue strength class of the hot spot design S-N curve for butt welded joints and non- or partially load-carrying fillet welded joints is FAT 40 (FAT refers to the characteristic stress range at 2 million cycles), and that for load-carrying joints is FAT36.

The thickness effect is a decrease in the fatigue strength with an increase in the main plate thickness [23]. The cause of thickness effect is raising local stress at the weld toe with an increase in the main plate thickness. In the IIW recommendation, the thickness effect is considered in the case of the main plate thickness over 25 mm, the same as welded steel structures.

There exist much literature on fatigue strength of welded aluminum joints. Ribeiro, de Jesus and Feup [24] conduct fatigue test for butt welded joint and three types of fillet welded joints, and investigate prediction method of fatigue life for welded aluminum joints. Bloem et al. [25] propose models for mechanical response of welded aluminum joints under fatigue loading. Coughlin and Walbridge [26] summarize an investigation conducted to examine the fatigue behavior of aluminum welds under in-service highway bridge loading conditions.

Partanen and Niemi [27] report fatigue test results of welded aluminum joints with the main plate thickness up to 6 mm. The joint types in the reference [27] are butt welded joints, lap welded joints, non-load-carrying fillet welded joints, and panel welded model. They mention that the hot spot design S-N curve of the IIW recommendations is suitable. On the other hand, Tveiten, Xiaozhi and Berge [15] indicate that the fatigue strength of the welded aluminum ship structure model with main plate thickness of 10 mm was lower than the hot spot design S-N curve of the IIW recommendations. Zamzami and Susmel [28] investigated fatigue strength of welded aluminum joints which are non-load-carrying cruciform joints, non-load-carrying Tee joints, and load-carrying cruciform joints. They concluded that the hot spot design S-N curve of the IIW recommendations is at an adequate level of conservatism; however, the thickness effect for the HSS approach is not considered. Maddox [16] conducted fatigue tests for non-load carrying cruciform joints with main plate thickness between 3 and 24 mm, and pointed out that considering the thickness effect is the necessary even if main plate thickness is less than 25 mm.

As mentioned above, the thickness effect for welded aluminum joints is not sufficiently clarified. To appropriately assess fatigue strength by the HSS approach for welded aluminum

joints, further studies for the thickness effect are needed. This study aims to clarify the thickness effect for welded aluminum joints and to propose a suitable hot spot design S-N curve for welded aluminum joints with various main plate thicknesses. The thickness effect is examined by using results of fatigue tests in this study and fatigue data of references. The fatigue tests are performed on 5083-O welded joint specimens with four main plate thicknesses, namely 12 mm, 16 mm, 20 mm, and 25 mm. Main plate thicknesses of the fatigue data of references ranged from 2.8 mm to 25 mm. Furthermore, fatigue tests on a welded aluminum structural model are conducted to validate the proposed HSS design S-N curve based on the fatigue data of welded aluminum joint specimens.

2.2 Fatigue strength assessment based on hot spot approach

2.2.1 Hot spot stress

In general, the HSS is determined by the extrapolation of stress to the weld toe from reference points, as shown in Fig. 2.1. Recommendations and guides describe the distance from the weld toe to reference points and the extrapolation method of stress. In guides for ship structures (e.g. ABS), the reference points are 0.5 t and 1.5 t, and the extrapolation method of stress is linear extrapolation. t means the main plate thickness. The HSS can be calculated by finite element analysis even for complicated structures. The HSS approach assumes that local stress at the weld toe can be divided into two parts. The first part is governed by structural stress increase, and the second part arises from localized notch stress due to weld toe. The HSS describes the stress increase in the first part. Thus, the S-N curve for the HSS approach considers the effect of the localized notch.

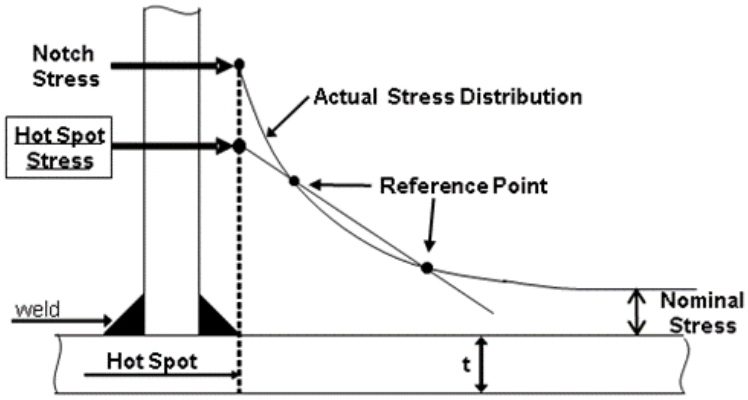

Fig. 2.1. Definition of hot spot stress.

2.2.2 Design S-N curves

S-N curves are described by the following equation.

$$\Delta\sigma^m \cdot N = C \qquad (2.1)$$

where $\Delta\sigma$ is the stress range, N is the number of cycles, C is the constant, and m is the slope of the S-N curve in the double logarithmic scale. The hot spot design S-N curves can be expressed by a few curves, because the HSS includes the stress raising effect of structural discontinuities. Figure 2.2 shows the hot spot design S-N curves for welded aluminum joints in the IIW recommendations and the ABS guide. The hot spot design S-N curves of the IIW recommendations are FAT40 for butt welded joints and non- or partially load-carrying fillet welded joints, and FAT36 for load-carrying joints. The hot spot design S-N curves of the ABS guide can be applied to stiffener or bracket attachments end with fillet weld. Table 2.1 lists the parameters of the hot spot design S-N curves of the IIW recommendations and the ABS guide.

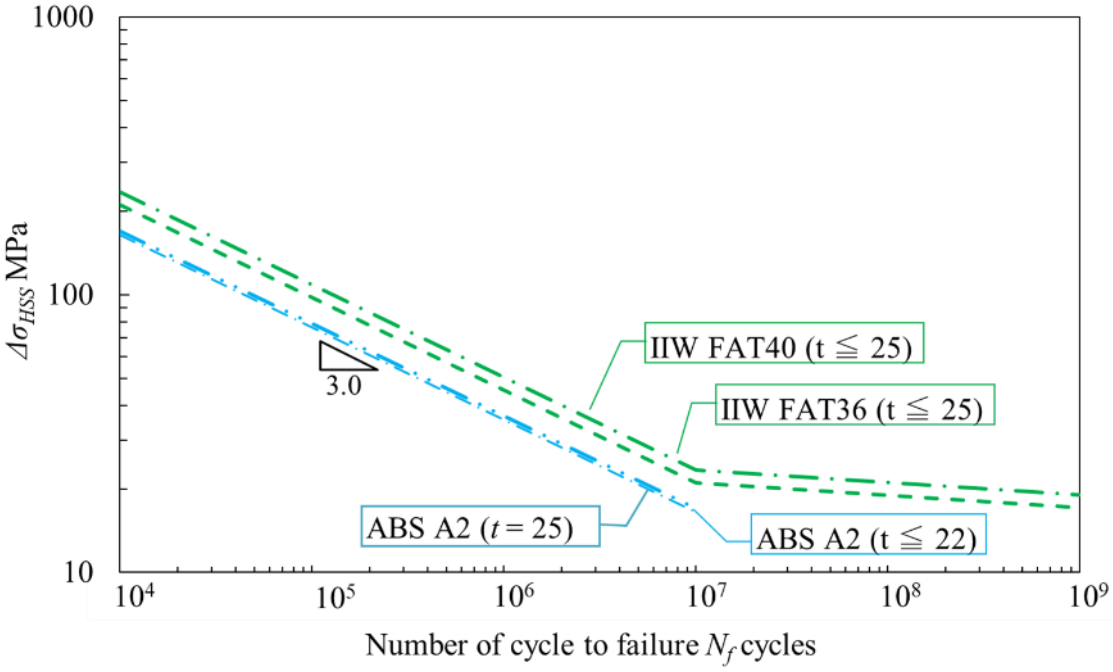

Fig. 2.2. Hot spot design S-N curves of the IIW recommendations and the ABS guide for welded aluminum joints.

Table 2.1 Parameters of the hot spot design S-N curves for welded aluminum joints in the IIW recommendations and the ABS guide.

Institution	Type of joint	Name of class	Slope of S-N curve m		Fatigue strength (MPa)	
			$< 10^7$ cycle	$> 10^7$ cycle	10^5 cycle	2×10^6 cycle
IIW [2]	Butt weld, non- or partially load-carrying fillet weld	FAT40	3.0	22	109	40
	Load-carrying weld	FAT36	3.0	22	98	36
ABS [3]	Stiffener or bracket attachments end with fillet weld	A2	3.0	-	79	27

2.2.3 Thickness Effect

The thickness effect should be considered in the fatigue strength assessment based on the HSS approach, because the HSS excludes the part of localized notch stress due to weld toe.

In the previous paper [12], we pointed out that the local stress field, including the localized notch stress at weld toe, affects the thickness effect on the fatigue strength of welded joints.

In the recommendation and the guide, the thickness effect is imposed for the main plate thickness greater than the reference thickness t_{ref}. In the IIW recommendations, the correction factor $f(t)$ of the FAT is given as:

$$f(t) = \left(\frac{t_{ref}}{t_{eff}}\right)^n \qquad (2.2)$$

$t_{ref} = 25 \text{ mm}$

if $L/t > 2$ then $t_{eff} = t$

if $L/t \leq 2$ then $t_{eff} = 0.5L$ or t which ever is the larger

where L is the sum of weld leg length and attached plate thickness. The thickness correction exponent n for as-welded joints excluding butt weld is 0.3.

In the ABS guide, the correction factor $g(t)$ of the stress range is given as:

$$g(t) = \left(\frac{t}{t_{ref}}\right)^n \qquad (2.3)$$

$t_{ref} = 22 \text{ mm}$

$n = 0.25$

In this paper, we multiply the hot spot design S-N curve of the ABS guide by $1/g(t)$ in order to discuss the thickness effect.

2.3 Fatigue test for welded specimens

We conducted fatigue tests for typically welded joints, which are non- or partially load-carrying fillet welded joints, of the main plate thickness between 12 mm and 24 mm.

2.3.1 Material

The parent material is 5083-O, which is based on the Japanese Industrial Standards (JIS) H 4000 [57], and the weld metal is 5183-WY, which is based on the JIS Z 3232 [58]. The chemical composition and mechanical properties of 5083-O and 5183-WY are listed in Table 2.2.

Table 2.2 Chemical composition and mechanical properties (as quoted from [57, 58]).

5083-O								
Chemical compositions (Weight percent)								
Si	Fe	Cu	Mn	Mg	Cr	Zn	Ti	Al
≤0.4	≤0.4	≤0.1	0.4~1.0	4.0~4.9	0.05~0.25	≤0.20	≤0.15	Bal.
Mechanical properties								
Tensile strength (MPa)			Yield strength (MPa)			Elongation (%)		
≥275			≥125			≥14		
5183-WY								
Chemical compositions (Weight percent)								
Si	Fe	Cu	Mn	Mg	Cr	Zn	Ti	Al
≤0.4	≤0.4	≤0.1	0.5~1.0	4.3~5.2	0.05~0.25	≤0.25	≤0.15	Bal.
Mechanical properties								
Tensile strength (MPa)			Yield strength (MPa)			Elongation (%)		
≥275			-			-		

2.3.2 Geometrical properties of test specimens

Figures 2.3-2.5 show the shapes of the three specimens. The types of welded joints are the non-load-carrying cruciform joint, the longitudinal fillet welded gusset with sharp end and

the longitudinal fillet welded gusset with soft end; they are designated by Type A, B and C, respectively.

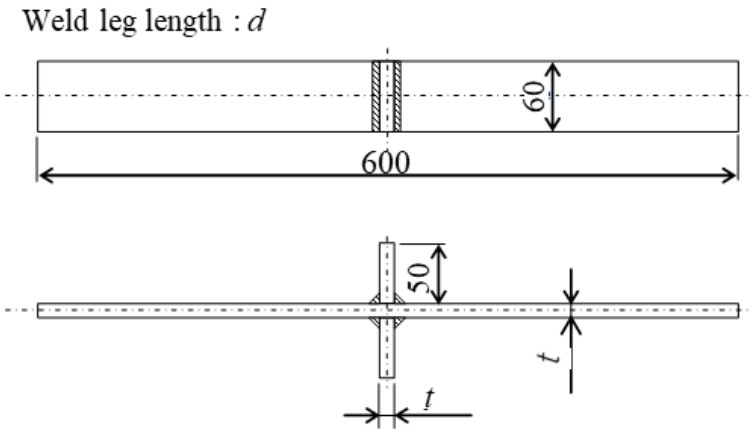

Fig. 2.3. Geometrical properties of Type A specimen.

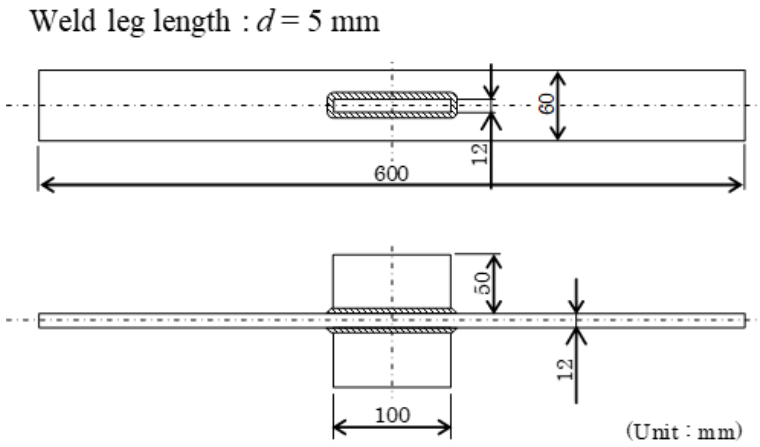

Fig. 2.4. Geometrical properties of Type B specimen.

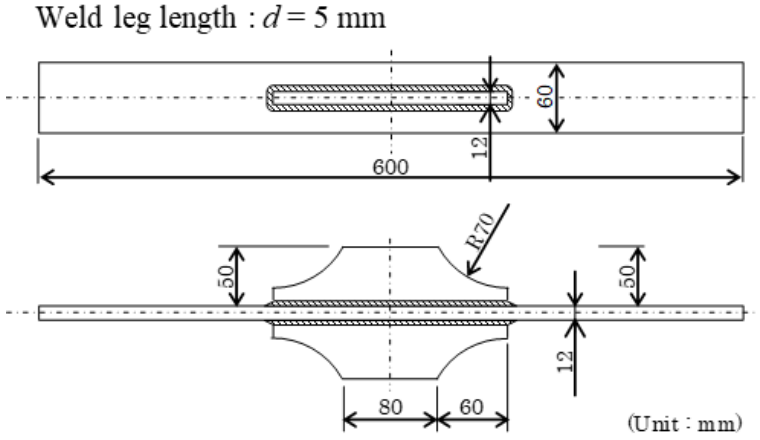

Fig. 2.5. Geometrical properties of Type C specimen.

Table 2.3 Dimensions and numbers of test specimens (Unit: mm).

	Dimensions of specimens				Number of specimens	HSS measurement
	W	*H*	*d*	*t*		
Type A2	60	50	5	12	5	0.5*t* - 1.5*t*
Type A4	60	50	7	20	4	0.5*t* - 1.5*t*
Type A5	60	50	6	16	5	0.5*t* - 1.5*t*
Type A6	60	50	7	25	5	0.5*t* - 1.5*t*
Type B	60	50	5	12	5	0.5*t* - 1.5*t*
Type C	60	50	5	12	5	0.5*t* - 1.5*t*

2.3.3 Fatigue test conditions of test specimens

The fatigue tests were conducted using servo-hydraulic actuators. Constant amplitude fatigue tests were conducted under load control at room temperature. Fatigue axial loading was applied to the welded joints with a stress ratio of 0.05 and a test frequency of 5–20 Hz. The cycle to failure N_f was defined as the complete separation of the main plate into two parts starting from the fatigue crack. The HSS was measured using strain gauges located at reference points, as shown in Fig. 2.6. We adopted the 0.5*t*-1.5*t* method based on the ABS guide. The applied constant HSS range $\Delta\sigma_{HSS}$ was in the range of 29 to 184 MPa. Secondary bending stress on clamping of specimens due to welding angular distortion affects hot spot stress ratio. Fig. 2.7 shows the box plot of hot spot stress ratio considering effect of secondary bending stress. Hot spot stress ratio are distributed vicinity of 0.05. Thus, we shall assume that the effects of secondary bending stress is small.

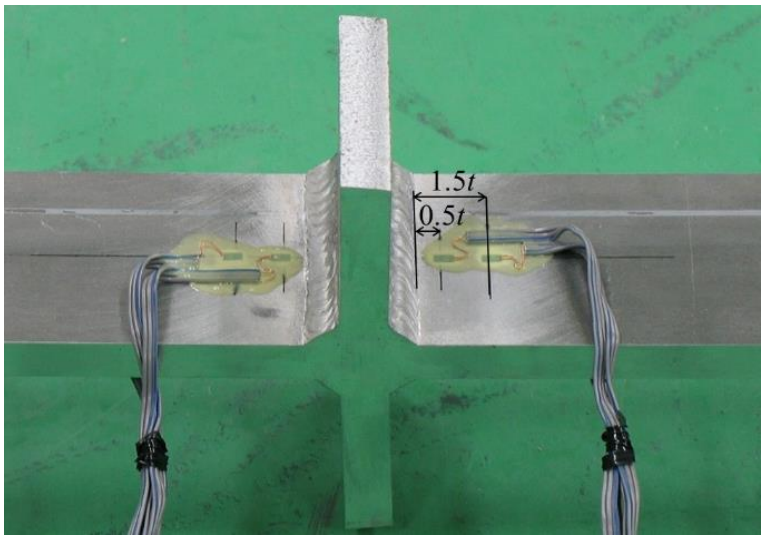

Fig. 2.6. Measurement of HSS using strain gauges.

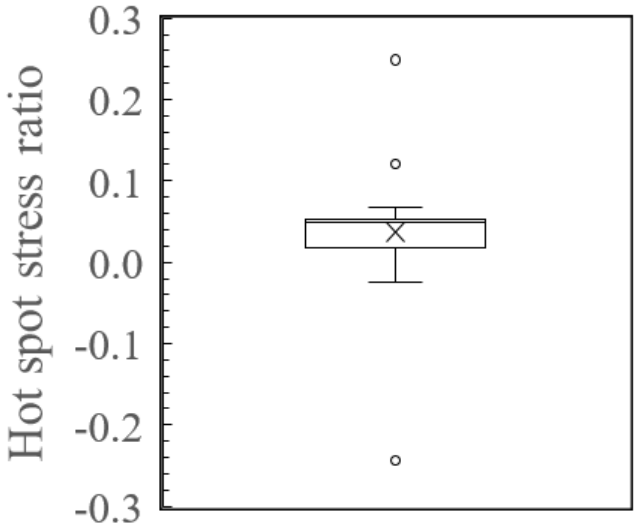

Fig. 2.7. Box plot of hot spot stress ratio.

2.3.4 Fatigue test results

For all the fractured specimens, fatigue crack initiated at the weld toe. Fig. 2.8 shows the fatigue test results based on the HSS approach. When the main plate thickness is the same, the fatigue strength based on the HSS approach indicates a small scattering, regardless of type of welded joint types. Therefore, it is reasonable to use the HSS approach to assess fatigue

strength for welded aluminum joints. Fatigue strength of t = 20 mm and 25 mm are obviously lower than t = 12 mm. Thus, the test results show the thickness effect.

The design S-N curves of the IIW recommendations and the ABS guide are also described in Fig. 2.8. Some of the test results show a lower fatigue strength than the design S-N curve of the IIW recommendations, specifically for thicker main plate thickness. The design S-N curve of the ABS guide gives a roughly plausible assessment of fatigue strength. However, some of the test results of t = 20 mm and t = 25 mm are lower than the design S-N curve of the ABS guide. The present results suggested that it is needed to examine carefully the thickness effect of aluminum joints with a thickness of less than 25 mm.

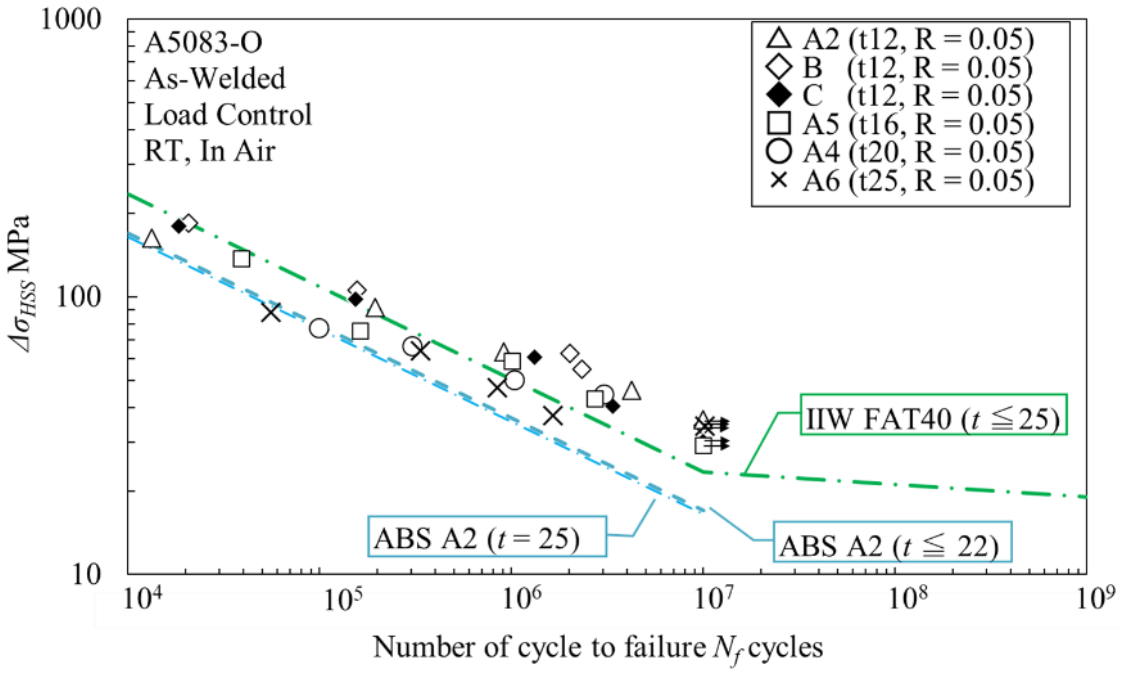

Fig. 2.8. Test results based on the HSS for welded joint specimens.

2.4 Hot spot design S-N curves based on fatigue test data

2.4.1 Research work for thickness effect

To clarify the thickness effect of welded aluminum joints, we conducted an accumulation of fatigue data, which employed the HSS approach, for butt welded joints and non- or partially load-carrying fillet welded joints. The loading condition of these fatigue data was axial loading. Fig. 2.9 shows relationships of fatigue strength based on the HSS approach and main plate thickness, where the main plate thickness of the fatigue test data ranges between 2.8 mm and 25 mm. The fatigue tests were carried out by Lihavainen [59], Hakuli [60], Maddox [16], and authors (Table 2.3). All of the HSSs of the fatigue data are determined by measurement using strain gauges. The reference points for the HSS calculation of some of the fatigue data are different from that of this study. The Japan Ship Technology Research Association reported the measurement of the HSS using the 0.5t-1.0t, the 0.5t-1.5t, and the 0.4t-2.0t method, respectively [61]. The results show that the differences in the values of the HSS because of the difference in the reference points are less than 10%. In this study, we shall assume that the effects of the differences in the reference points are small.

The data clearly show a decrease in fatigue strength with an increase in the main plate thickness. These results are described by following equation.

$$\Delta\sigma = \Lambda t^{-n} \qquad (2.4)$$

where n is the thickness correction exponent. By using least squares fitting, we obtained n = 0.37 at 10^5 cycle and n = 0.32 at 2×10^6 cycle, respectively. The design curves of the IIW

recommendations and ABS guide are also plotted in Fig. 2.9. The IIW recommendations and ABS guide do not impose the thickness effect up to the reference thickness. Thus, the design curves of the IIW recommendations and ABS guide in Fig. 2.9 are flat up to the reference thickness. Since the IIW recommendations and ABS guide consider the thickness effect in case of main plate thickness over the reference thickness, the design curves of the IIW recommendations and ABS guide above the reference thickness in Fig 2.9 have negative slopes that coincide with the thickness correction exponent *n*. The design curve of the IIW recommendations presents an un-conservative side assessment for thicker specimens. The design curve of the ABS guide gives over-conservative side assessment for the thin thickness specimens.

Table 2.4 Fatigue data based on the HSS approach.

Reference	Base metal	Type of joint	*t* (mm)	No of data	Stress ratio	Slope of S-N curve *m*	Fatigue strength $\Delta\sigma_{HSS}$(MPa)		Reference point of HSS
							10^5 cycle	2×10^6 cycle	
[59]	A6005a	Butt weld	2.8	12	0-0.6	3.0	215	79	Unknown
[60]	A6082	Round pad	6	18	0.1-0.5	3.6	147	64	Unknown
[16]	6061-T6	Fillet weld	3	8	0.1	4.6	158	82	5 mm
[16]	6061-T6	Fillet weld	6	8	0.1	4.9	112	61	5 mm
[16]	6061-T6	Fillet weld	12	13	0.1	3.9	122	57	5 mm
[16]	6061-T6	Fillet weld	24	9	0.1	3.9	85	40	5 mm
This study	A5083	Cruciform weld	12	5	0.05	4.0	105	54	0.5*t*-1.5*t*
This study	A5083	Gusset	12	5	0.05	3.6	123	59	0.5*t*-1.5*t*
This study	A5083	Gusset Soft Toe	12	5	0.05	3.4	113	50	0.5*t*-1.5*t*
This study	A5083	Cruciform weld	16	5	0.05	4.0	97	46	0.5*t*-1.5*t*
This study	A5083	Cruciform weld	20	4	0.05	6.0	77	47	0.5*t*-1.5*t*
This study	A5083	Cruciform weld	25	5	0.05	4.0	79	38	0.5*t*-1.5*t*

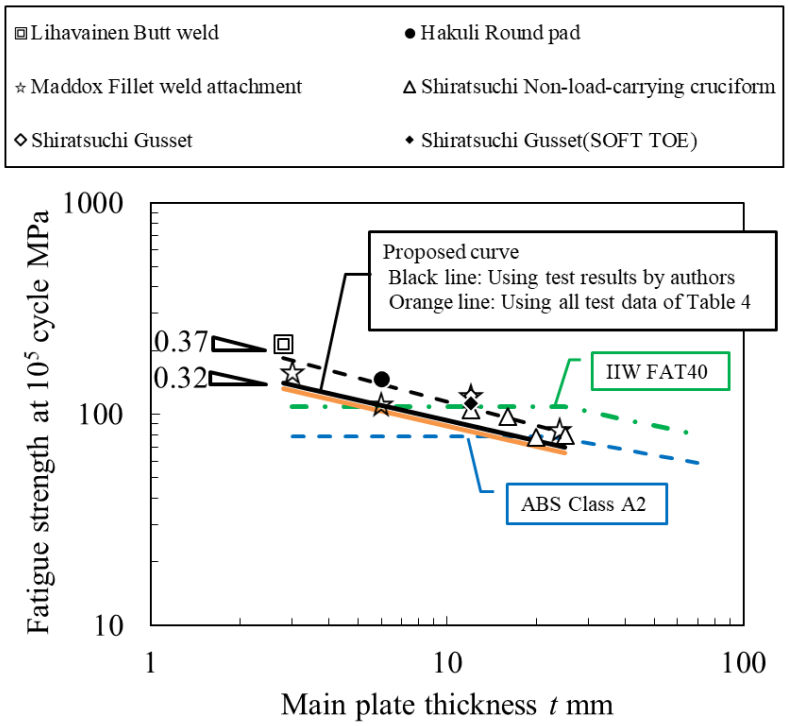

(a) Fatigue strength at 10^5 cycle.

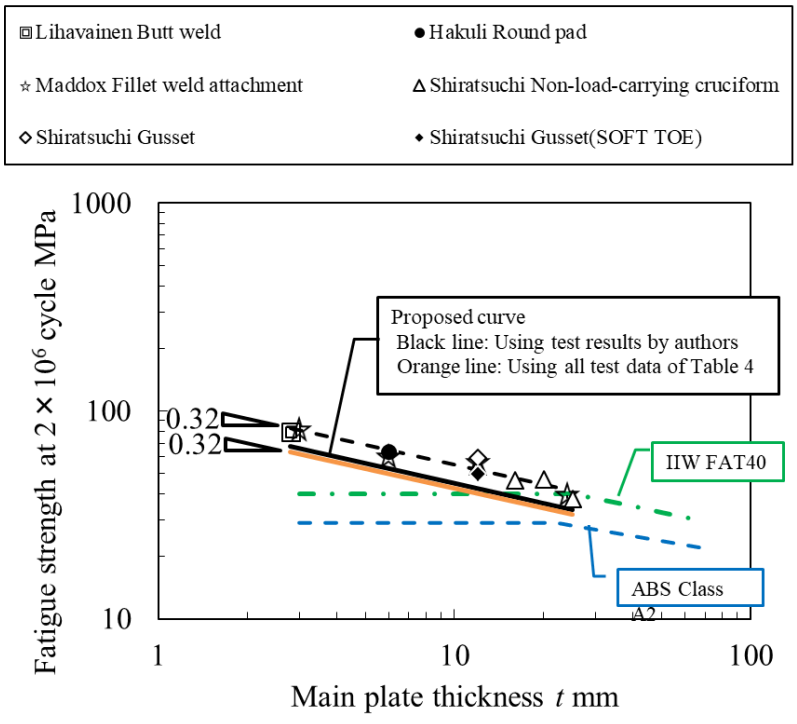

(b) Fatigue strength at 2×10^6 cycle

Fig. 2.9. Relationships of fatigue strength and the main plate thickness based on the HSS approach.

2.4.2 Proposed hot spot design S-N curve

We investigate a more suitable hot spot design S-N curve as the basis for the research of the thickness effect. In this study, we propose a hot spot design S-N curve based on the following procedure:

a) We employ that the value of the thickness correction exponent *n* is 0.32, which is experiment data at 2×10^6 cycle.

b) The fatigue strength of the fatigue tests in this study are converted to that for the reference thickness. The converting equation is given as:

$$\Delta\sigma(t_{ref}) = \Delta\sigma(t) \times \left(\frac{t}{t_{ref}}\right)^{0.32} \qquad (2.5)$$

where the reference thickness t_{ref} is 25mm.

c) The proposed hot spot design S-N curve is defined as a mean-minus-two-standard-deviation curve for the fatigue test results that are converted to that for the reference thickness using Eq. 2.5.

The mean curve and standard deviation are evaluated using the fatigue test results by authors and all fatigue data listed in Table 2.4, respectively. According to the IIW recommendations, to calculate a mean-minus-two-standard-deviation curve based on statistical analysis, it is needed to perform fatigue tests at about 20 specimens. Number of failure occurrence test data by

authors is 24, that listed in Table 2.4 is 92.

Fig. 2.10 shows the fatigue test results by authors converted to that of the reference thickness using Eq. 2.5. The converted fatigue test results show a small scattering, regardless of the main plate thickness and types of welded joint types. The proposed hot spot design curve using fatigue test results by authors is indicated by solid line in Fig. 2.10. We note that this design curve is derived from the deviation of the fatigue test results by authors. The slope of the proposed design S-N curve using the fatigue test results by authors is 4.14 and the fatigue strength for t = 25 mm of that is 33.6 MPa at 2×10^6 cycle.

Fig. 2.11 shows all the fatigue data listed in Table 2.4 converted to that of the reference thickness using Eq. 2.5, and the proposed design S-N curve using all fatigue data listed in Table 2.4. The proposed design S-N curve using all the fatigue data listed in Table 2.4 indicate almost the same as those using the fatigue test results by authors.

Table 2.5 gives the parameters and fatigue strength of the proposed design S-N curves. The limitations of the proposed design curve are as follow:

- The environment is in air at room temperature.
- The type of joints are butt welded joints and non- or partially load-carrying fillet welded joints.
- The fatigue life ranges from 10^4 to 10^7 cycle.

Table 2.5 Proposed S-N curves based on the HSS approach.

Employed test data	Design curve for t = 25mm			
	Constants of S-N curve		Fatigue strength (MPa)	
	C	m	10^5 cycle	2×10^6 cycle
Test results by authors	4.19×10^{12}	4.14	69.4	33.6
All test data listed in Table 4	3.27×10^{12}	4.14	65.2	31.6

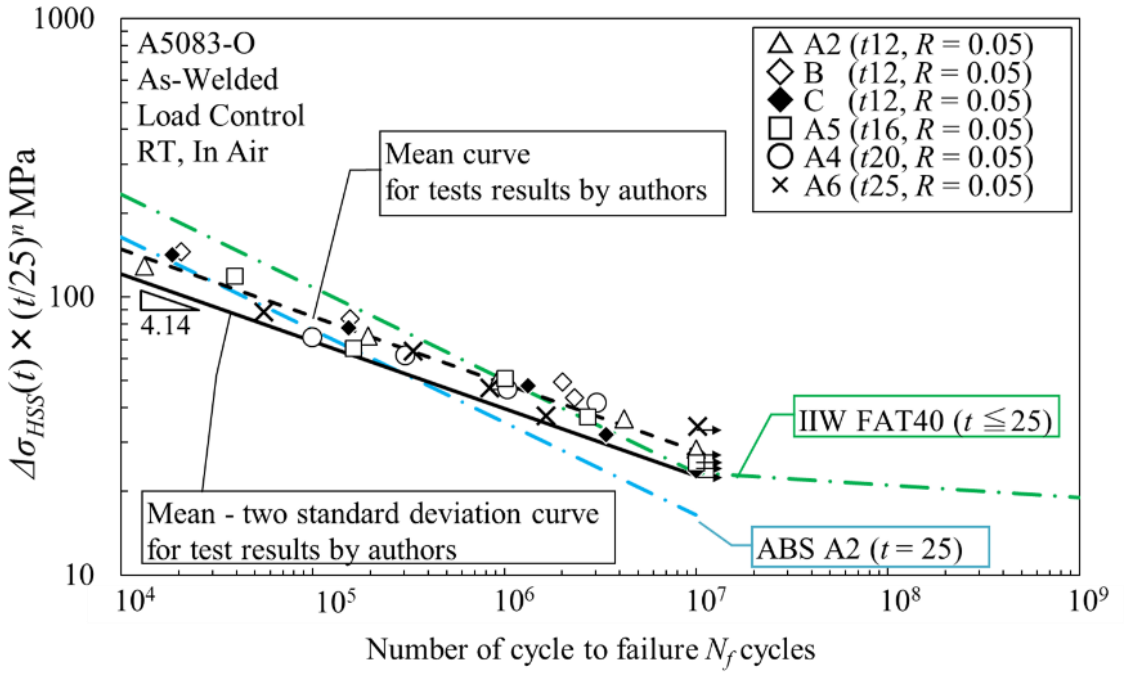

Fig. 2.10 Proposed hot spot design S-N curve based on fatigue test results by authors.

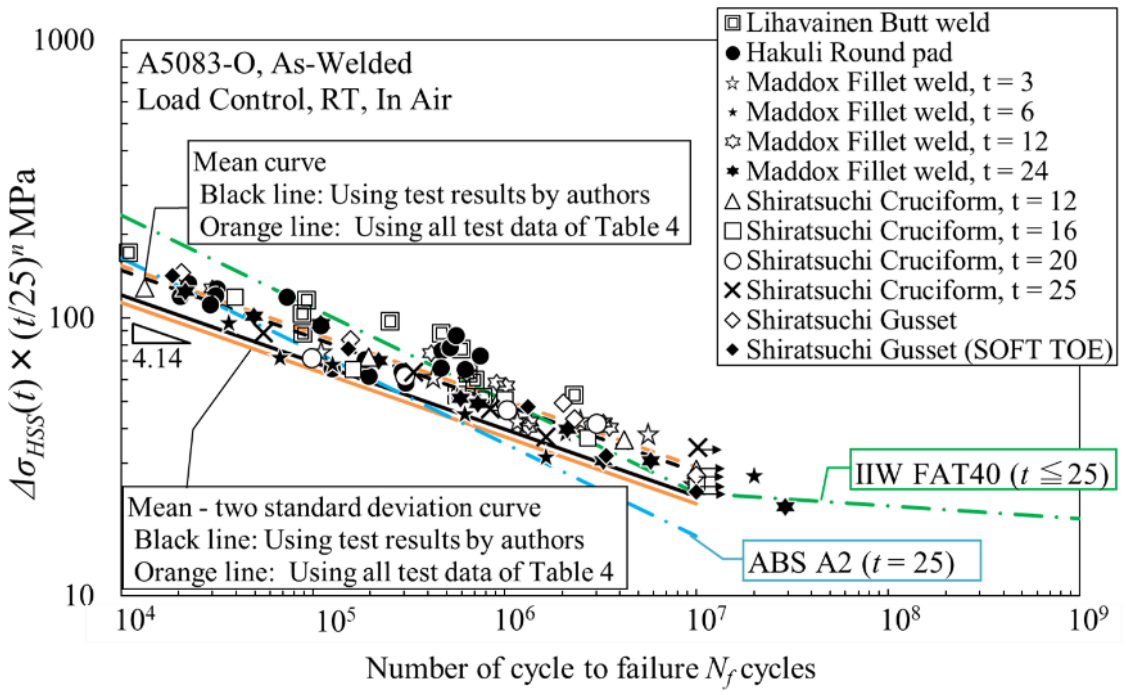

Fig. 2.11. Proposed hot spot design S-N curve based on all fatigue data listed in Table 2.4.

2.5 Validation of design S-N curve for welded structures

To test the validity of the proposed design curve for welded aluminum structures, we conducted fatigue tests with a large scale structural test model. For the same purpose, fatigue data of literature [15], which use a full scale model of a ship structure detail, was investigated.

2.5.1 Large scale test model

The parent material is 5083-O, which based on the JIS H 4000, and the weld metal is 5183-WY, which based on the JIS Z 3232. These are same as materials of the welded joint specimens. Fig. 2.12 shows schematic drawing and the appearance of the large scale test model.

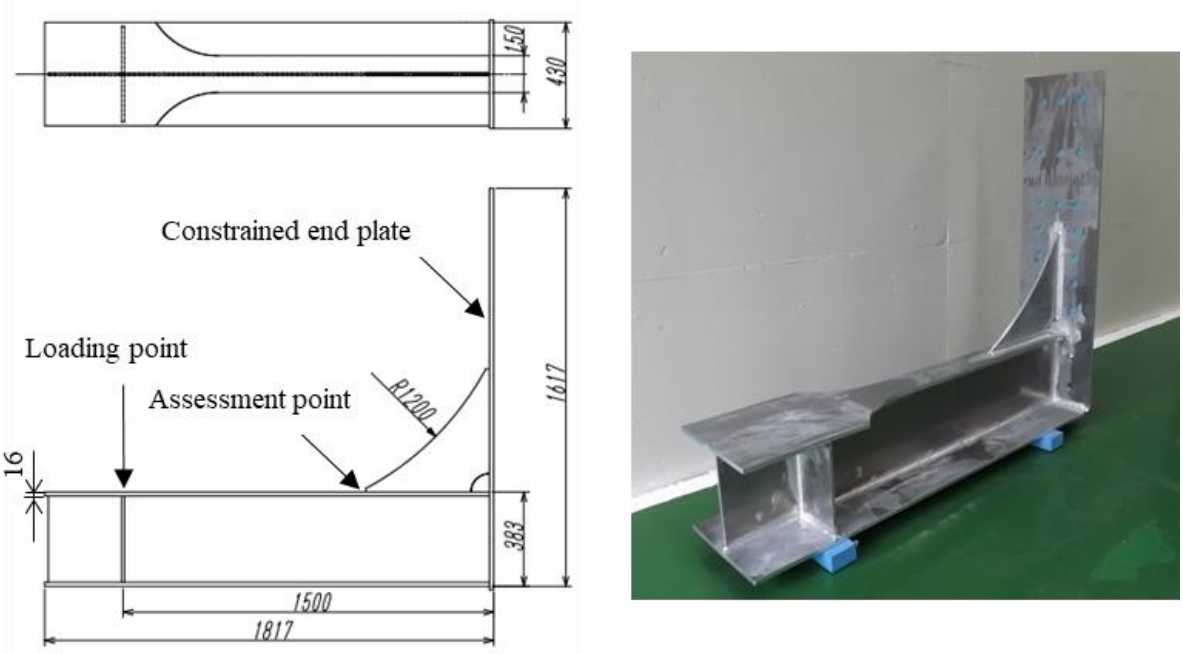

Fig. 2.12. Large scale test model.

2.5.2 Fatigue test conditions of the large scale test model

The endplate of the test model was constrained to a reaction wall, and cantilever mode load was applied to the large scale model. The assessment point is the weld toe at the end of the

bracket.

Constant amplitude fatigue tests were conducted load control at room temperature. Fatigue load was applied to the large scale model in a sinusoidal waveform with a frequency of 1 Hz and a stress ratio of $R = 0.05$. The frequency of 1 Hz was used as a maximum frequency possible to obtain a stable controlled sinusoidal loading waveform. The frequency of the fatigue tests for the large scale model was different from that for welded joint specimens. Davidson, Griffiths and Machin [62] report that no effect of the test frequency was detected for fatigue tests of aluminum material conducted at 1 and 60 Hz. Thus, we shall assume that the effects of the difference in the test frequency can be ignored.

The HSS was measured using strain gauges located at reference points. We adopted the 0.5t-1.5t method, the same as the fatigue tests of welded joint specimens. The applied constant HSS range $\Delta\sigma_{HSS}$ was in the range of 33 to 98 MPa.

It was difficult to conduct the fatigue test by reaching failure of large scale model due to lack of funds and time. Instead of continuation of fatigue test, we measured a surface fatigue crack width at terminated fatigue test; then fatigue crack propagation analysis from crack size at terminated fatigue test to failure were conducted. The fatigue crack propagation analysis was based on the linear elastic fracture mechanics and the Paris law. Unfortunately, the fatigue crack depth at the terminated fatigue test was unclear. We assumed that the relationship between the surface half crack width b and crack depth c, as shown in Fig. 2.13 which were reported literatures [63-65] based on fatigue test results for welded joints. The relationship between the surface half crack width b and the crack depth c are described by following equation.

$$b = 4c \qquad (2.6)$$

For the fracture of the large test model, we assumed that the maximum value of the stress intensity factor K_{max} reaches fracture toughness at 50 MPa$\sqrt{m}$ [66].

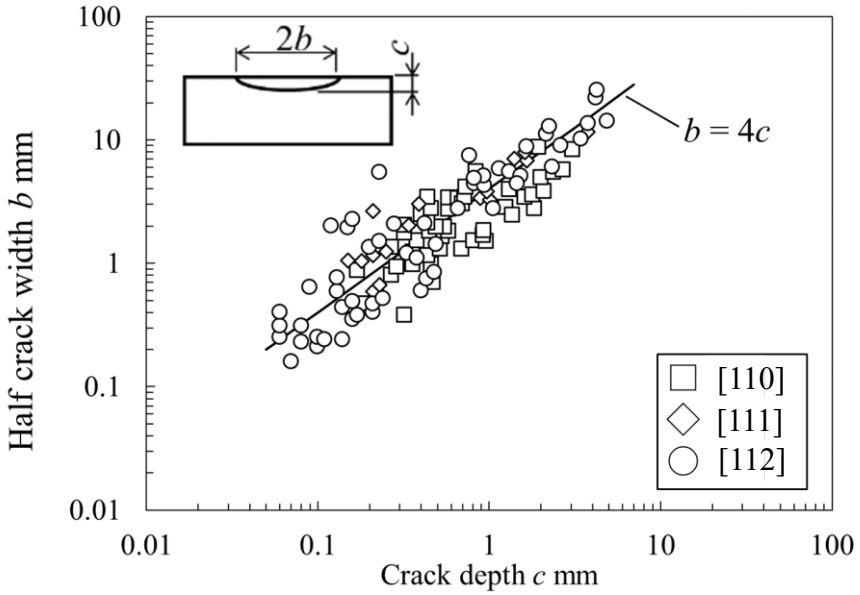

Fig. 2.13. Relationship between surface half crack width b and crack depth c.

2.5.3 Test results

Table 2.6 lists the fatigue test results for the large scale model. The fatigue cracks of the test models initiated at the weld toe of the assessment point.

Table 2.6 Fatigue test results for the large scale model

No.	Applied HSS range $\Delta\sigma_{HSS}$ (MPa)	Half crack width at terminated test b (mm)	Cycle to terminated test (cycle)	Crack propagation life from terminated test to failure test model (cycle)	Total fatigue life (cycle)
1	98	22.5	7.77×10^4	4.88×10^4	1.27×10^5
2	54	25.0	7.61×10^5	3.84×10^5	1.14×10^6
3	40	13.5	1.15×10^6	1.17×10^6	2.32×10^6
4	33	10.0	3.07×10^6	2.43×10^6	5.50×10^6

2.5.3.1 Fatigue crack propagation analysis

A fatigue crack propagation analysis was conducted using the FRacture ANalysis Code 3D (FRANC3D) with the stress analysis code NASTRAN. First, FRANC3D made mesh to calculate the stress intensity factor at the crack tip. Second, stress analysis was conducted using NASTRAN, and the resulting displacements of the stress analysis were read back into FRANC3D, which then calculated the stress intensity factors. The stress intensity factors were used to predict the amount of crack propagation basis of the Paris law. FRANC3D re-meshed based on the extended crack, and the stress analysis of the next step was conducted. This process was repeated. FRANC3D calculates stress intensity factors using the M-integral approach [67]. The M-integral approach is similar to the J-integral approach [68]. Fig. 2.14 shows the finite element model for the No. 2 test model at the first step of crack propagation analysis. The finite element models employ solid secondary elements. Fig. 2.15 shows boundary and loading conditions of the stress analysis. Young's modulus of E = 69 GPa and Poisson's ratio of ν = 0.28 were applied.

To clarify the characteristic of crack propagation for A5083-O, the crack propagation test based on ASTM E 647-08[69] was conducted with a stress ratio of 0.1 and the accumulation of crack propagation data [70]. Fig. 2.16 indicates the relationship between the crack

propagation rate and the stress intensity factor range for 5083-O. Similar to reference [16] which is reported crack propagation characteristic for 6061-T6, there was no significant effect of the stress ratio on linear region in the double logarithmic scale for relationship between crack propagation rate and stress intensity factor range. In the low stress intensity factor range, the stress ratio affects the crack propagation rate. In this study, it is assumed that a high tensile residual stress occur in large scale model, the crack propagation characteristics employ following equation which shown in Fig. 2.16.

$$\frac{da}{dN} = 4.36 \times 10^{-11} \Delta K^{3.44} \qquad (2.7)$$

Fig. 2.17 shows the history of the crack propagation that was obtained by the crack propagation analysis using FRANC3D with NASTRAN. Figure 2.18 shows the relationship between the stress intensity factors and the crack depth in the fatigue crack analysis for the No.2 large scale model condition. The results of estimations of the crack propagation life from the terminated fatigue test to the failure test model are listed in Table 2.6.

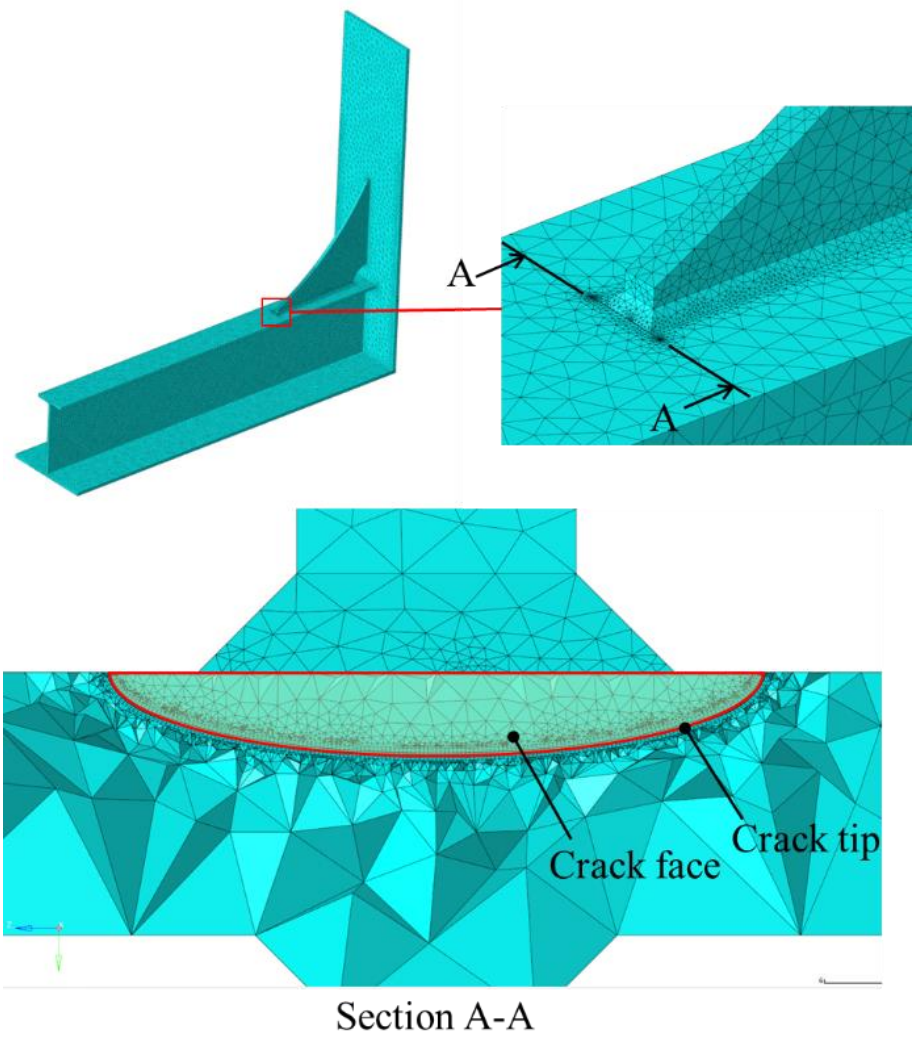

Fig. 2.14. Finite element model to calculate the stress intensity factor.

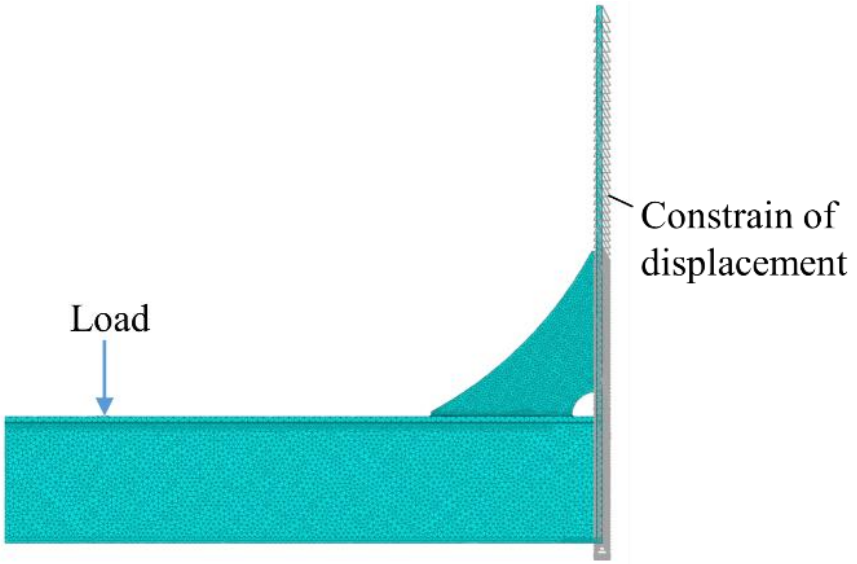

Fig. 2.15 Boundary and loading conditions of the stress analysis.

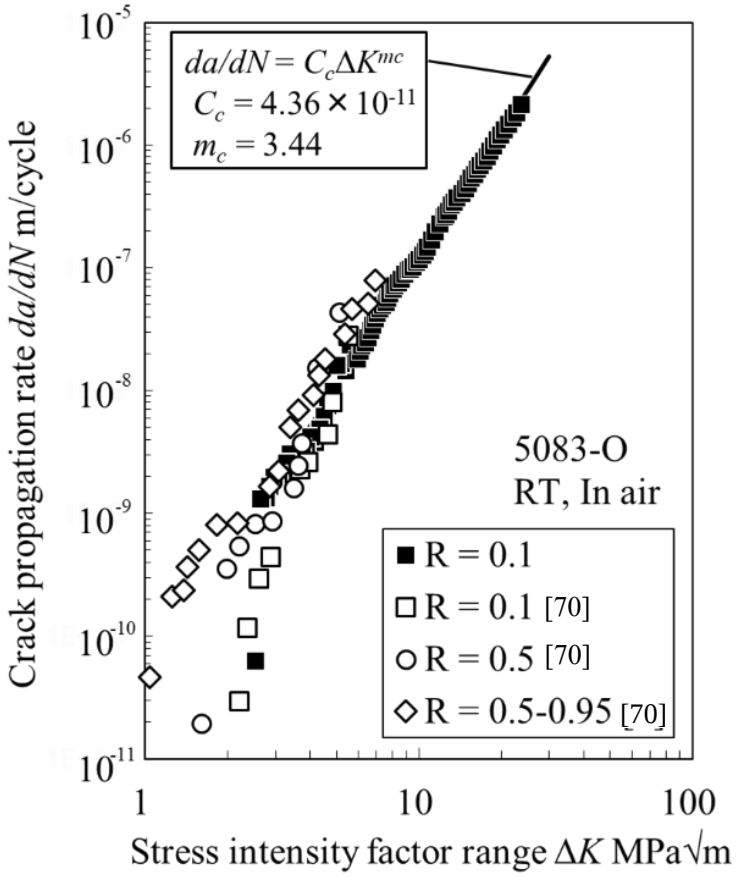

Fig. 2.16. Relationship between the crack propagation rate and the stress intensity factor range.

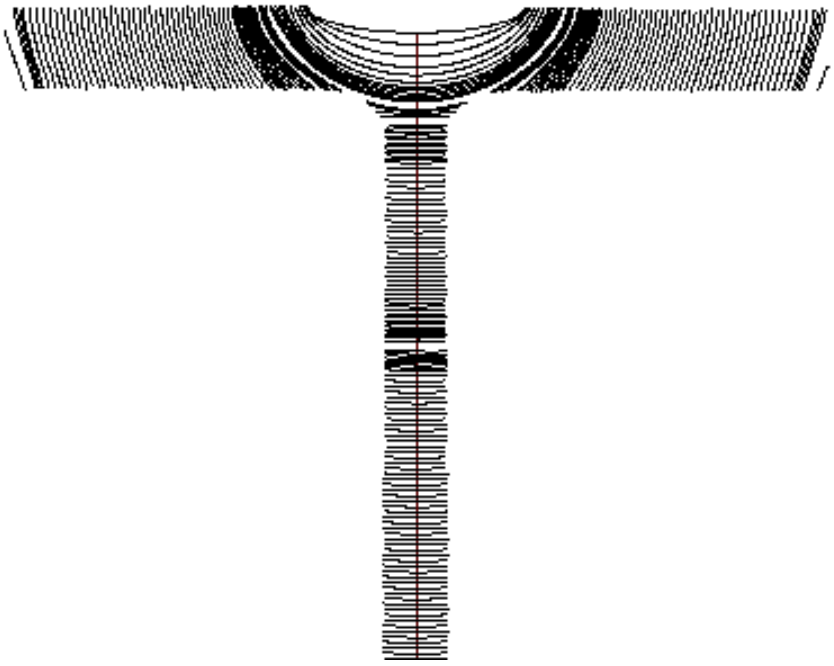

Fig. 2.17. History of crack propagation for the No. 2 large scale model.

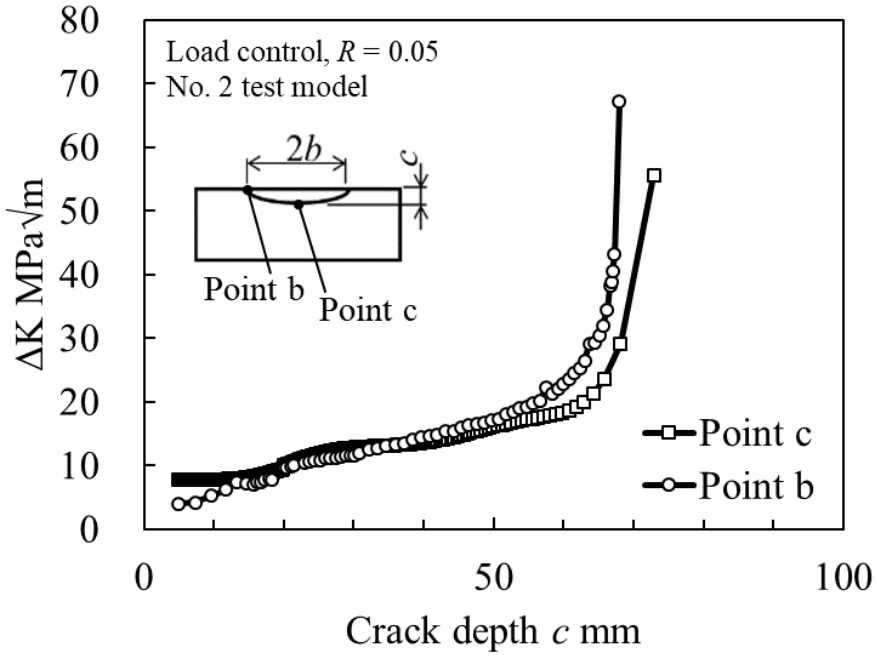

Fig. 2.18. Relationship between stress intensity factors and crack depth.

2.5.3.2 S-N curve

Fig. 2.19 shows the S-N relationship of the large scale model. The ordinate of Fig. 2.19 indicates the HSS converted to that of reference thickness using Eq. 2.5. Fatigue data of literature [15], which use full scale model of ship structure detail, was shown Fig. 2.19. The cycle to failure N_f for fatigue data of the literature was defined as the complete loss of the load carrying capacity. Table 2.7 lists the fatigue test results for the large scale model and full scale model. The converted fatigue strength to that of the reference thickness is at the same level, regardless of the main plate thickness. Moreover, the proposed hot spot S-N curves provide roughly suitable assessment for welded structures.

Table 2.7 Fatigue data based on the HSS approach.

Reference	Base metal	Main plate thickness t (mm)	No of data	Stress ratio	Slope of S-N curve m	Fatigue strength $\Delta\sigma_{HSS}$ (MPa)		Reference point of HSS
						10^5 cycle	2×10^6 cycle	
This study	A5083-O	16	4	0.05	3.4	92	38	0.5t-1.5t
[15]	A6082	10	8	0.1	3.5	137	58	0.5t-1.5t

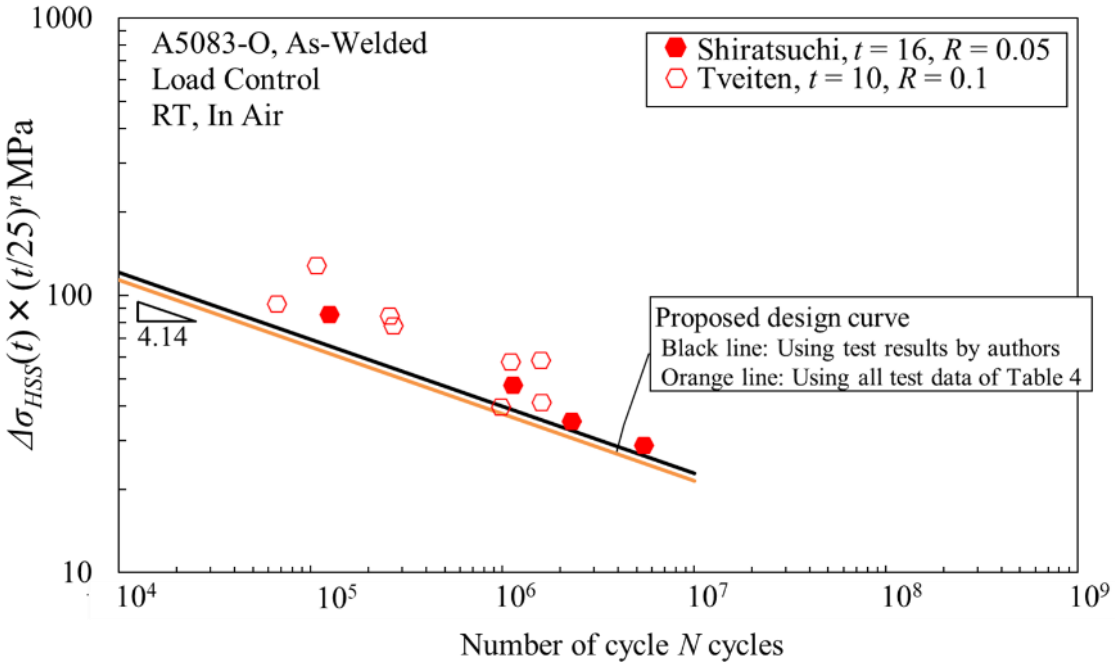

Fig. 2.19. Fatigue test results of large scale models.

2.6 Discussion

2.6.1 Mean stress effect

The proposed hot spot design S-N curves, which are based on experimental data for butt welded joints and non- or partially load-carrying fillet welded joints, provide a roughly suitable assessment for welded structures. However, the above investigation does not consider the mean stress effect. In general, welded structures indicate higher residual stress than welded joint specimens. Thus, to appropriately assess the fatigue strength of welded structures, the

mean stress effect should be considered. Fig. 2.20 shows mean stress (stress ratio) effect for fatigue strength of welded aluminum butt joint at 2×10^6cycle [71]. Fatigue strength with stress ratio of 0.7 was 85 percent of that with a stress ratio of 0.0. This value is close to 80 percent that is described in the IIW recommendations. Fig. 2.21 shows the 80 percent line of proposed design S-N curves. The 80 percent line of the proposed design S-N curves is over-conservative around the region of 10^5 cycle. More experimental or analytical work is necessary to clarify the mean stress effect.

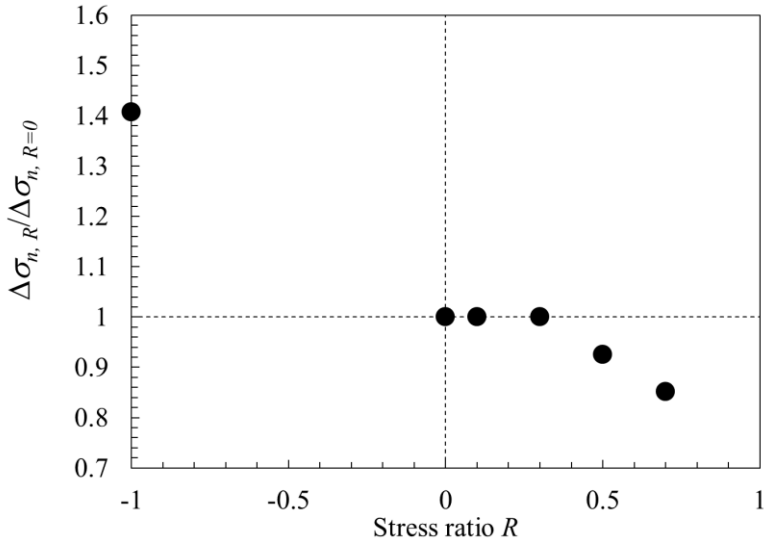

Fig. 2.20. Mean stress effect for fatigue strength of welded aluminum butt joint at 2×10^6 cycle.

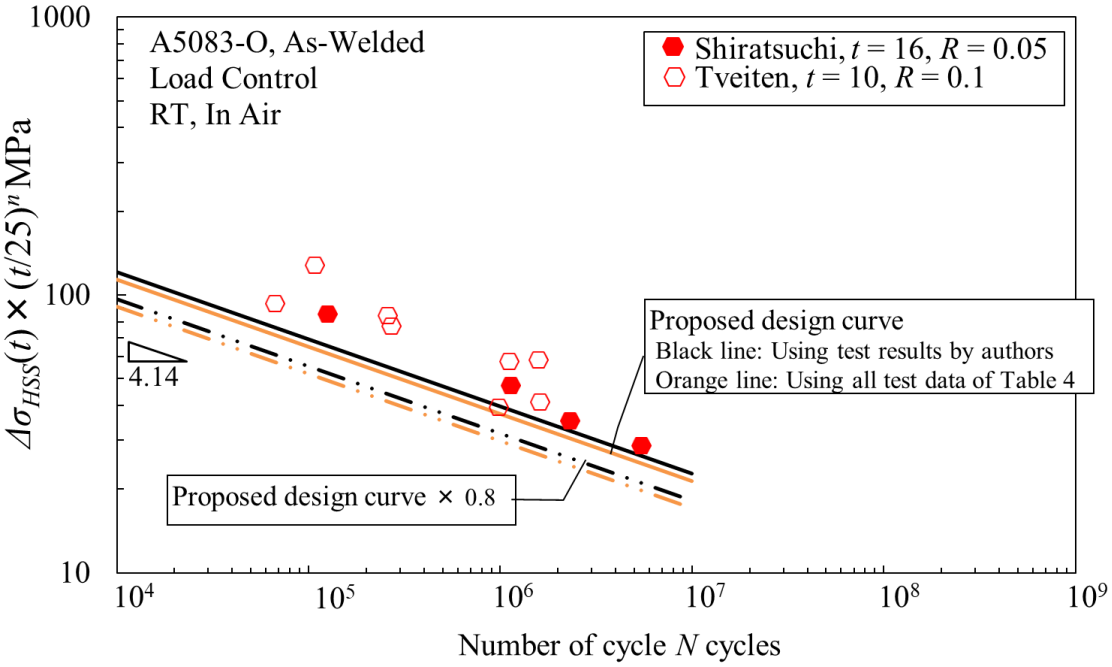

Fig. 2.21. Proposed design curves considering mean stress effect.

2.6.2 Load carrying welded joints

In the IIW recommendations, design hot spot S-N curves are distinguished between that for load-carrying joints and that for another joints. The proposed hot spot design S-N curves are based on experimental data for butt welded joints and non- or partially load-carrying fillet welded joints. Figure 2.22 shows the comparison between the fatigue test data of load-carrying cruciform joints and the proposed design curves. Table 2.8 lists the fatigue test data of load-carrying cruciform joints. The proposed design curves are appropriate for the fatigue strength assessment of load-carrying cruciform joints at 2×10^6 cycle. On the other hand, the proposed design curves indicate slightly un-conservative assessment for load-carrying cruciform joints at 10^5cyle. The reason of this related to difference of the slope of S-N curve. Fig. 2.23 shows relationship between the slope of the S-N curve and main plate thickness. The slope of the S-N curve is independent to the main plate thickness regardless for joint type. On the whole, the

slope of the S-N curve *m* for load-carrying cruciform joints were higher than that for butt welded joints and non- or partially load-carrying fillet welded joints. The direct cause for deference of the slope of the S-N curve need to be further investigated in order to appropriately assess fatigue strength of load-carrying aluminum welded joints.

Table 2.8 Fatigue data for load-carrying cruciform joints based on the HSS approach

Reference	Base metal	Type of joint	t (mm)	No of data	Stress ratio	Slope of S-N curve m	Fatigue strength $\Delta\sigma_{HSS}$(MPa)		Reference point of HSS
							10^5 cycle	2×10^6 cycle	
[72]	Al Mg Si	Load-carrying	4	31	0	6.0	137	83	0.4t-1.0t
[72]	Al Mg Si	Load-carrying	8	23	0	6.0	97	59	0.4t-1.0t
[72]	Al Mg Si	Load-carrying	8	25	0	5.9	83	50	0.4t-1.0t
[73]	Al Zn Mg1	Load-carrying	12	12	0.08	5.8	96	58	0.4t-1.0t
[73]	Al Zn Mg1	Load-carrying	12	14	0.08	4.6	103	54	0.4t-1.0t
[72]	Al Zn4 Mg1	Load-carrying	4	27	0	3.5	179	76	0.4t-1.0t
[72]	Al Zn4 Mg1	Load-carrying	8	27	0	4.2	120	59	0.4t-1.0t
[72]	Al Zn4 Mg1	Load-carrying	8	18	0	4.1	106	51	0.4t-1.0t
[74]	6061-T651	Load-carrying	12	12	0.1	5.3	81	46	0.4t-1.0t
[74]	Al Zn Mg1	Load-carrying	12	18	0.1	4.4	97	49	0.4t-1.0t

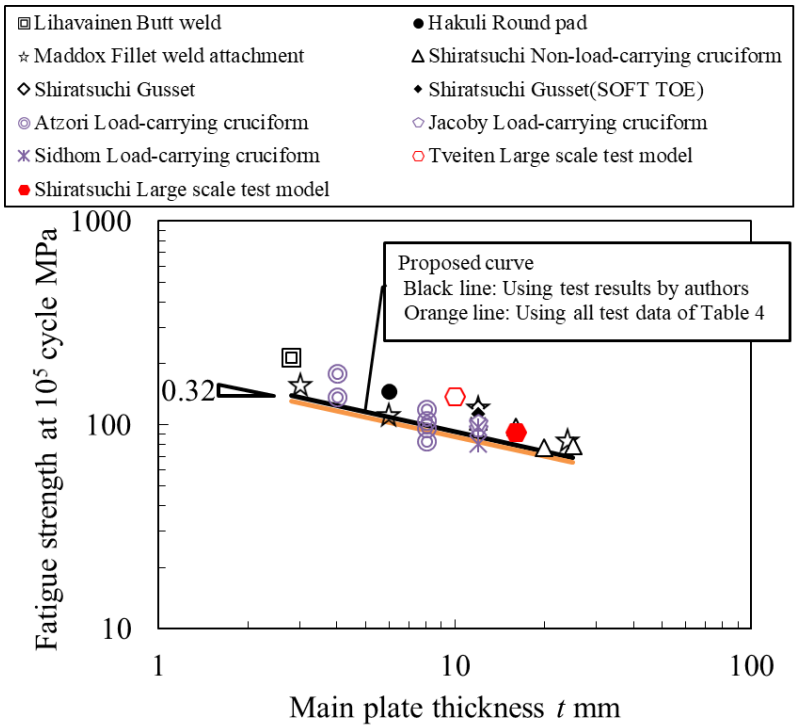

(a) Fatigue strength at 10^5 cycle

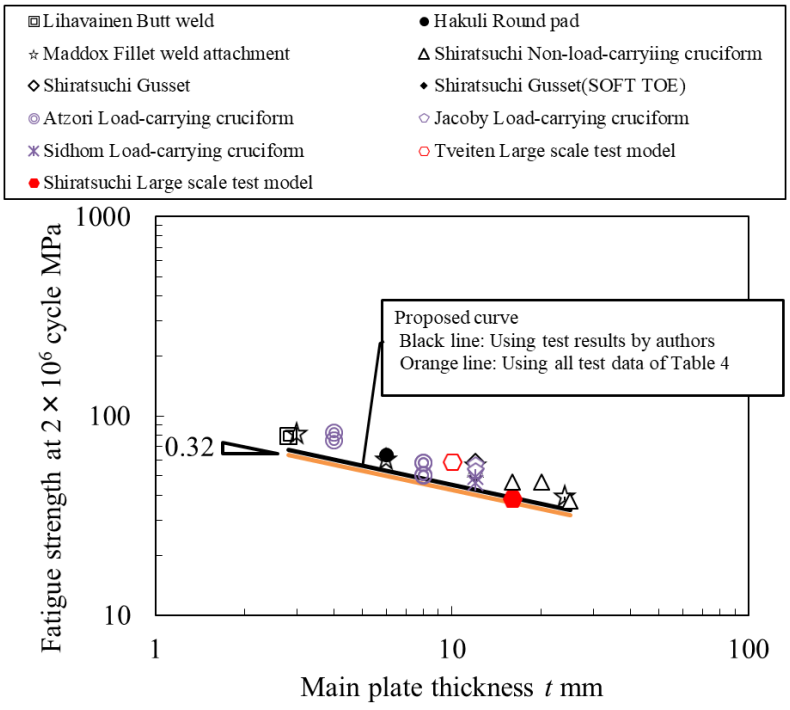

(b) Fatigue strength at 2×10^6 cycle

Fig. 2.22. Thickness effect of fatigue strength for load-carrying cruciform joints.

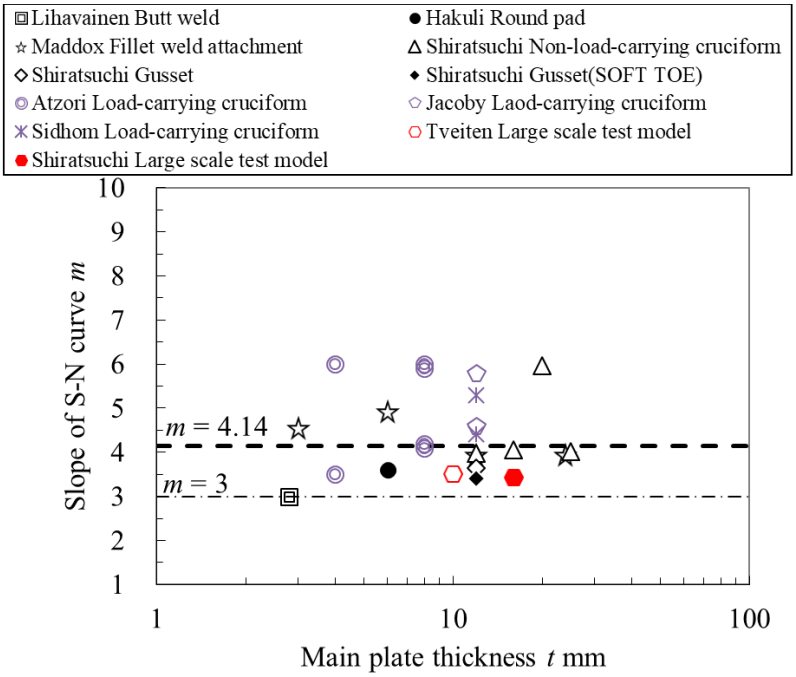

Fig. 2.23. Relationship between slope of S-N curve and main plate thickness.

2.6.3 Slope of hot spot design S-N curve

The slope of the proposed hot spot design S-N curves, which is 4.14, differ from 3.0 which is employed to the design S-N curves in the IIW recommendations and ABS guide. In this section, assuming the fixed slope of S-N curves which is 3, the thickness correction exponent n and mean-minus-two-standard-deviation curves for the fatigue test results are assessed.

Figure 2.24 shows the relationships between the fatigue strength and the main plate thickness. The thickness correction exponent n is 0.36, which is similar value in the case of free slope of the S-N curve. The mean-minus-two-standard-deviation curves in the case of m = 3 indicate over-conservative, as shown in Fig. 2.25. It is presumed that the IIW recommendations and the ABS guide employ safe-side slope for the design S-N curves.

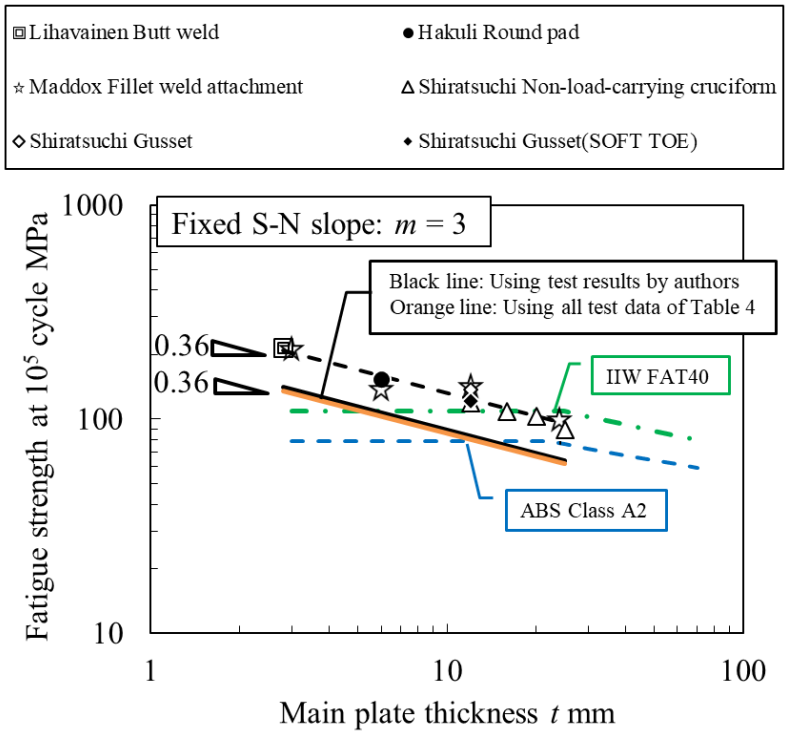

(a) Fatigue strength at 10^5 cycle

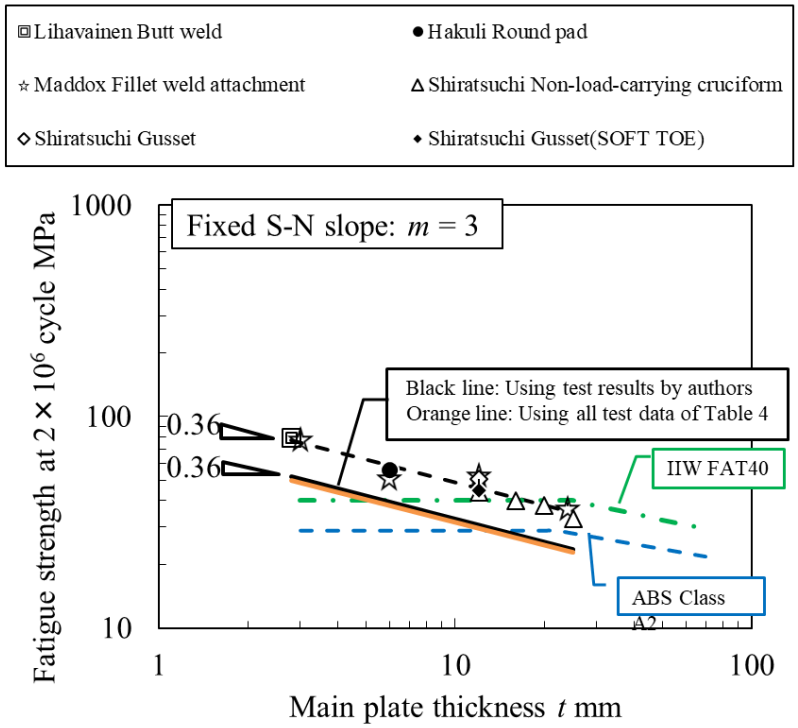

(b) Fatigue strength at 2×10^6 cycle

Fig. 2.24. Thickness effect of fatigue strength in the case of fixed S-N slope: $m = 3$.

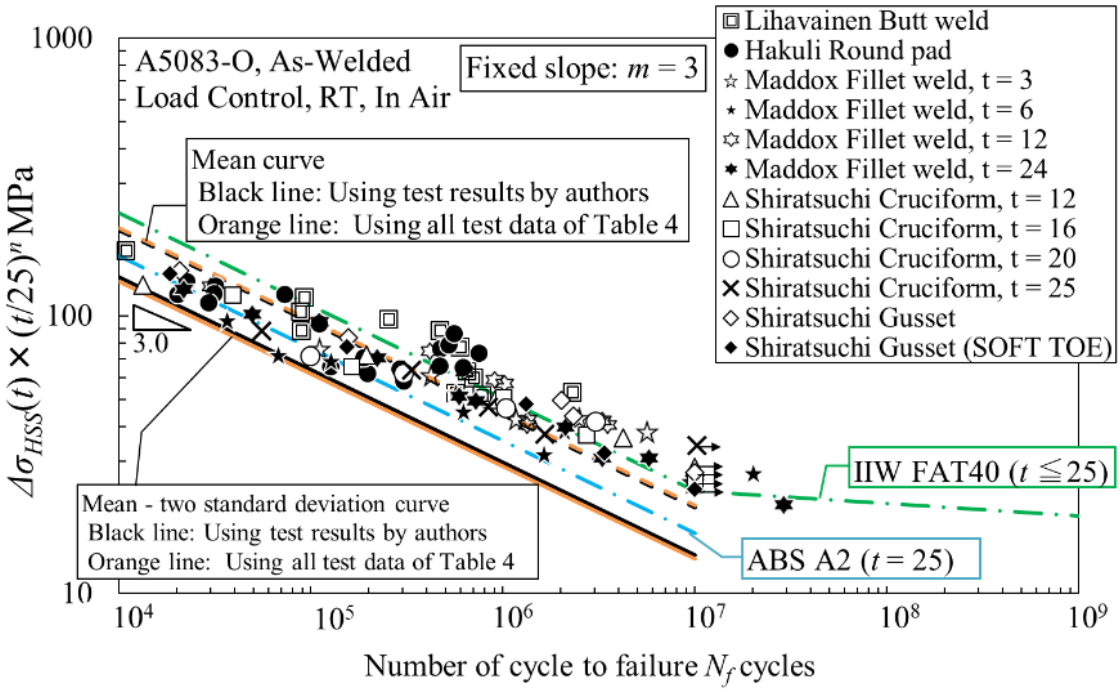

Fig. 2.25 Mean-minus-two-standard-deviation curves in the case of fixed S-N slope: $m = 3$

2.7 Conclusions

The fatigue tests of welded aluminum joint specimens with four main plate thicknesses, 12 mm, 16 mm, 20 mm, and 25 mm were conducted to obtain the fatigue data. The thickness effect up to $t = 25$ mm was examined through experimental results in this study and fatigue data from references. The hot spot design S-N curve based on the research work on the thickness effect was presented. Finally, the validity of the proposed hot spot design S-N curve was evaluated by comparing the fatigue test data of welded joint specimens and large scale model. The results obtained can be summarized as follow:

- The fatigue strength of aluminum welded joint specimen decreases with an increase in the main plate thickness. This result obviously indicated the thickness effect on aluminum

welded joints up to t = 25 mm.

- The thickness correction exponent n on the basis of the HSS approach are 0.37 at 10^5 cycle and 0.32 at 2×10^6 cycle, respectively.

- The hot spot design S-N curve was presented which is based on the research work on thickness effect and statistical analysis of the fatigue test results.

- The proposed hot spot S-N curves provide a roughly suitable assessment for welded structures. To appropriately assess the fatigue strength of real welded structures, more experimental or analytical work is necessary to clarify the mean stress effect.

Chapter 3 Thickness and bead profile effects on fatigue strength of welded joints based on relative stress gradient

3.1 Introduction

Gurney [23] for the first time reported the thickness effect of fatigue strength for welded joints based on an analytical method of fracture mechanics. Johnston [29] carried out fatigue tests for non-load-carrying cruciform joints with different plate thicknesses, indicating a decreasing trend of fatigue strength alongside an increase in main plate thickness. Gurney [30] investigated existing fatigue test data and illustrated a double logarithmic linear relationship between fatigue strength and main plate thickness, as described in Eq. (3.1) below:

$$\Delta\sigma(t) = \Delta\sigma\left(t_{ref}\right) \times \left(\frac{t_{ref}}{t}\right)^{n} \qquad (3.1)$$

where t is main plate thickness, t_{ref} is reference plate thickness, $\Delta\sigma$ is fatigue strength and n is the thickness correction exponent. A significant body of literature exists on the thickness effect of fatigue strength for welded joints [31-35].

In the standards, the thickness effect is imposed based on Eq. (3.1). According to the International Institute of Welding (IIW) recommendations [10], the lower fatigue strength for thicker members is taken into consideration by multiplying the fatigue strength class of the structural detail by the thickness reduction factor $f(t)$:

$$f(t) = \left(\frac{t_{ref}}{t_{eff}}\right)^{n} \qquad (3.2)$$

$t_{ref} = 25 \text{ mm}$

if $L/t > 2$ then $t_{eff} = t$

if $L/t \leq 2$ then $t_{eff} = 0.5L$ or t, whichever is the larger

where L is the sum of weld leg length and attached plate thickness. Thickness correction exponent n for as-welded joints excluding transverse butt welded joints is 0.3. In a guide for building and classing for liquefied gas carriers with independent tanks [1], correction factor g (t) multiplying stress range is given as:

$$g(t) = \left(\frac{t}{t_{ref}}\right)^n \qquad (3.3)$$

$t_{ref} = 22 \text{ mm}$

$n = 0.25$

Gurney [36] indicated the effect of weld leg length on the fatigue strength of welded cruciform joints via fatigue crack growth analysis, assuming that an initial crack existed at the weld toe, as well as the thickness effect. However, weld toe radius was not considered in this analysis. Zerbst et al. [37] presented a method for determining the fatigue strength of welded joints by fracture mechanics. This method called the IBESS method can be considered the geometric effect including weld toe radius. The acronym IBESS stands for “Integrale Bruchmechanische Ermittlung der Schwingfestigkeit von Schweißverbindungen“ which means integral fracture mechanics determination of the fatigue strength of welded joints. However,

prediction results based on this method indicate over-conservative or non-conservative estimations for cruciform welded joints and out-of-plane gusset joints. The reasons for these results have to date not been clearly identified.

With a focus on the relationship between stress gradient and stress concentration factor, Yamamoto et al. [38] and Tatsuta et al. [39] studied geometric effect on fatigue strength for welded joints, including weld bead profiles. Stress gradient χ used by Yamamoto et al. [38] and Tatsuta et al. [39] is given as

$$\chi = \left|\frac{d\sigma}{dx}\right|_{x=0} \qquad (3.4)$$

where x is distance along the normal path indicating the direction of peak stress at the weld toe and σ is stress distribution on the x-axis, as shown Fig. 3.1. Yamamoto et al. [38] and Tatsuta et al. [39] pointed out that weld toe radius affects the relationship between stress gradient and stress concentration factor. However, the effect of weld toe radius was not investigated in detail. Siebel et al. [75] discussed the relationships between relative stress gradient χ^* and the ratio of stress concentration factor α to fatigue notch factor β for parent materials. Relative stress gradient χ^* indicated degree of stress decrease against peak stress σ_{max} in the vicinity of a notch. The formula for relative stress gradient can be described as

$$\chi^* = \frac{\chi}{\sigma_{max}} = \frac{1}{\sigma_{max}}\left|\frac{d\sigma}{dx}\right|_{x=0} \qquad (3.5)$$

where σ_{max} is peak stress at a notch. Fatigue notch factor β is given as

$$\beta = \frac{\sigma_{w0}}{\sigma_{wk}} \qquad (3.6)$$

where σ_{w0} is the fatigue limit of smooth specimens and σ_{wk} is that of notched specimens. Siebel et al. [75] pointed out that the geometric effect, including notch radius, on fatigue limit of notched specimens are related to relative stress gradient χ^*.

The purpose of the present study was to investigate the thickness and the bead profile effects, including weld toe radius, on fatigue strength for welded joints. In this study, we focused on relative stress gradient χ^*, because relative stress gradient χ^* is an important parameter for prediction of the geometric effect on fatigue limit for notched specimens. We employed the relationships between relative stress gradient χ^* and the ratio of stress concentration factor α to fatigue notch factor β to predict the thickness and the bead profile effects. We first clarify the characteristics of relative stress gradient χ^* for welded joints using the results of stress analyses and then propose a prediction method for establishing the geometric effect on fatigue strength for welded joints. The validity of the proposed method was tested by comparing it with fatigue test data reported in the literatures. Finally, based on the proposed method, parametric studies of the geometric effect on fatigue strength for welded joints were conducted for typical welded joints.

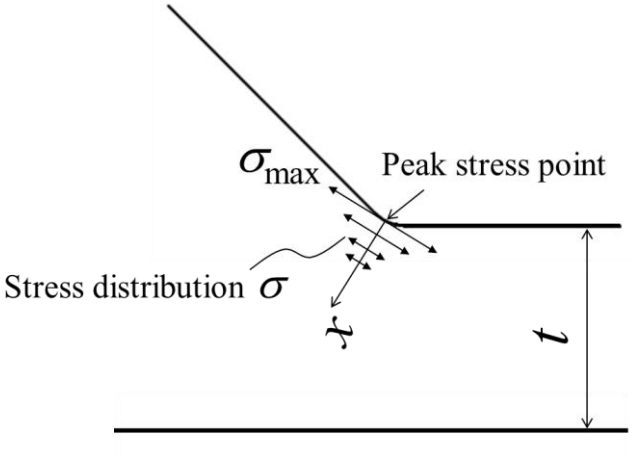

Fig. 3.1. Schematic drawing of stress distribution at the weld toe.

3.2 Prediction method of fatigue limit for notched specimens based on relative stress gradient

Figure 3.2 shows the relationships between relative stress gradient χ^* and the ratio of stress concentration factor α to fatigue notch factor β for parent materials [75]. The equation below indicates this as follows:

$$h_i(\chi^*) = \frac{\alpha}{\beta} \qquad (3.7)$$

where h_i (χ*) for each material i is as indicated in Fig. 3.2. Fatigue limit for notched specimens is derived from Eq. (3.6) and Eq. (3.7) as follows:

$$\sigma_{wk} = \frac{\sigma_{w0}}{\alpha} h_i(\chi^*) \qquad (3.8)$$

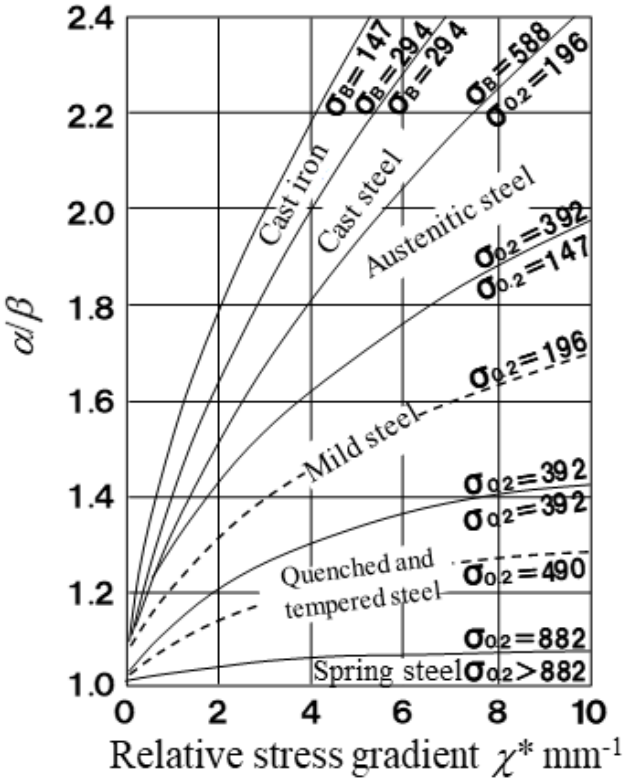

Fig. 3.2. Siebel diagram [75].

3.3 Relative stress gradient at weld toe

To clarify characteristics of relative stress gradient χ^* for welded joints, relative stress gradient χ^* at weld toe was calculated based on results of stress analyses reported in the literature [38, 76]. Types of welded joints which were conducted stress analyses were non-load-carrying cruciform joints, out-of-plane gusset joints, and welded structural models, as shown in Fig. 3.3. The dimensions of the welded joints are described in Appendix 1. Finite element elastic analyses were performed using the MSC/Nastran, in order to determine relative stress gradient χ^*. Plane strain elements were used for non-load-carrying cruciform joints. Solid elements were used for out-of-plane gusset joints and welded structural models. The size of elements around the weld toe was about 0.05 mm. Young's modulus of E = 206 GPa and Poisson's ratio of ν = 0.3 were applied. Loading conditions were as follows:

- non-load-carrying cruciform joints : axial loading and bending loading, respectively;
- out-of-plane gusset joints : axial loading;
- structural models : bending loading.

Relative stress gradient χ^* was calculated using stress distribution, from the peak stress point to a 1 mm depth along the normal direction of peak stress. Figure 3.4 shows the relationship between weld toe radius ρ and relative stress gradient χ^* at the weld toe for all stress analyses results (57 cases). As shown Fig. 3.4, relative stress gradient χ^* depends on markedly weld toe radius. Relative stress gradient χ^* is almost independence on joint types, loading conditions, geometric parameters excluding weld toe radius. The relationship between weld toe radius ρ and relative stress gradients χ^* showed good agreement with relative stress gradient χ^* for the plate containing a circular hole (Fig. 3.5), which can be described as Eq. (3.9) [77] below:

$$\chi^* = \frac{1}{\rho} \times \frac{7}{3} \qquad (3.9)$$

Based on the context of the current investigation, from the above results, relative stress gradient χ^* at the weld toe can be almost regarded as the function of weld toe radius only.

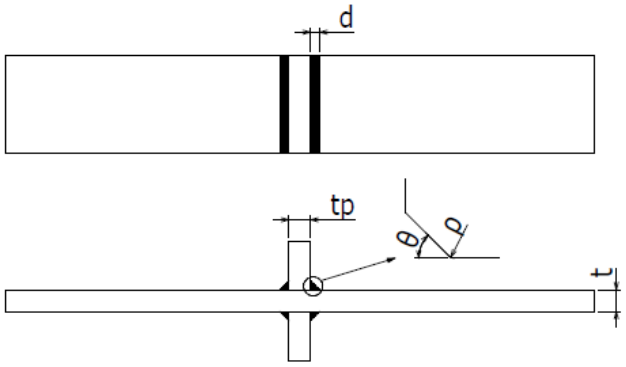

(a) Non-load-carrying cruciform welded joint.

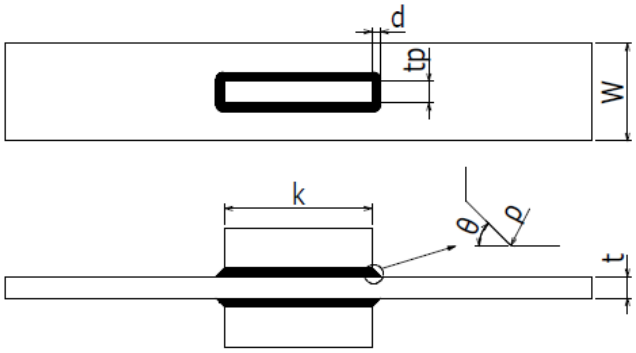

(b) Out-of-plane gusset welded joint.

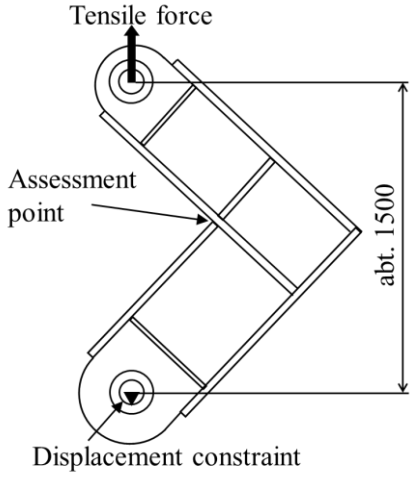

(c) L-type structural model [38].

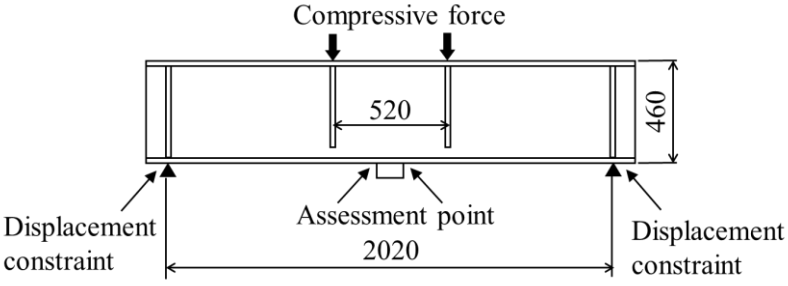

(d) I-type structural model [38].

Fig. 3.3. Geometry of welded joints.

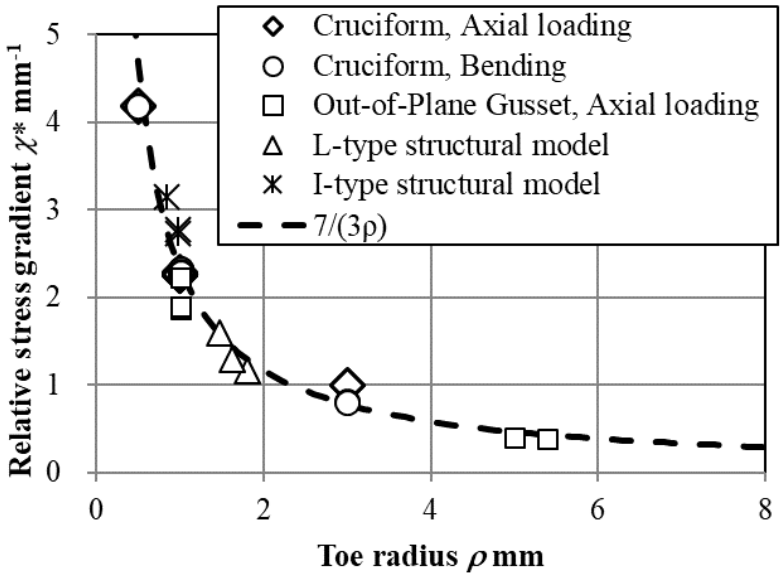

Fig. 3.4. Relationship between relative stress gradient $\chi*$ and weld toe radius ρ for welded joints.

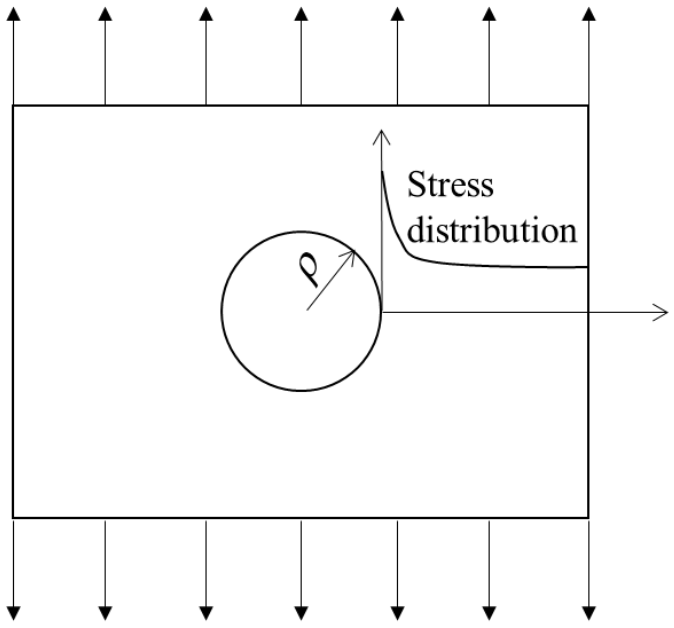

Fig. 3.5. Plate containing a circular hole.

3.4 Prediction method for the geometric effect of welded joints on fatigue strength

From Eq. (3.8) and Eq. (3.9), fatigue limit for welded joints σ_{ww} can be described as follows:

$$\sigma_{ww} = \frac{\sigma_{wr}}{\alpha} h_i(\chi^*) = \frac{\sigma_{wr}}{\alpha} J_i(\rho) \qquad (3.10)$$

where σ_{wr} is fatigue limit for smooth specimens with residual stress equal to welded joints. The geometric effect on fatigue limit for welded joints can be expressed by stress concentration factor α and the function of weld toe radius ρ as follows:

$$\sigma_{ww} = \frac{\alpha_{(ref)}}{\alpha} \frac{J_i(\rho)}{J_i\left(\rho_{(ref)}\right)} \sigma_{ww(ref)} \qquad (3.11)$$

where the subscript *ref* indicates reference welded joints. We defined the geometric effect function on fatigue limit for welded joints as G:

$$G_i = \frac{\alpha_{(ref)}}{\alpha} \frac{J_i(\rho)}{J_i\left(\rho_{(ref)}\right)} \qquad (3.12)$$

If $\rho = \rho_{(ref)}$, then the geometric effect function G is a function only of stress concentration factor α:

$$G = \frac{\alpha_{(ref)}}{\alpha} \qquad (3.13)$$

3.5 Validity of the proposed method

The validity of the proposed the geometric effect function *G* was tested by comparing it with fatigue strength at 2×10^6cycle of fatigue test data. Fatigue strength at 2×10^6cycle of fatigue data, as reported in literature, was calculated by least squares fitting using Eq. (3.14) to yield the following:

$$\Delta\sigma^m \cdot N_f = C \qquad (3.14)$$

where N_f is the number of cycles to failure, and *m* and *C* are constants. Firstly, we conducted a validity investigation for the fatigue strength of imitation specimens that mimicked the shape of cruciform joints. The imitation specimens were cut from a steel plate without welding, so that the imitation specimens did not have weld residual stress. We then examined the validity of the fatigue strength of welded joints. In this investigation, relative the stress gradient χ^* was calculated using Eq. (3.9).

3.5.1. Imitation specimen of the cruciform joint

Test specimens were cut from a normalizing KA32 steel plate, the chemical composition, and mechanical properties of which are listed in Table 3.1. Table 3.2 lists the

dimensions of test specimens and fatigue test results for imitation specimens [38]. Fatigue test conditions were as follows: load control with a test frequency of 5 Hz, a stress ratio of 0.05 and applied constant stress range $\Delta\sigma$ in the range of 120 to 310 MPa. Figure 3.6 shows function $h_i(\chi^*)$ for steel, the yield strength of which was 350 MPa, comparable with KA32 steel. The reference series for the prediction of fatigue strength is indicated by specimen number 9, listed in Table 3.2. Figure 3.7 indicates the prediction results for the fatigue strength of imitation specimens, based on proposed geometric effect function G: Figure 3.7 (a) indicates the results based on stress concentration factors calculated by finite element analyses, the conditions of that were the same as in section 3.3. Figure 3.7 (b) indicates the results based on stress concentration factors calculated by the formula presented in Tsuji [18] (described in Appendix 2). The solid line in Fig. 3.7 indicates an ideal line, which refers to the fatigue test data $\Delta\sigma_{exp}$ as being equal to prediction results $\Delta\sigma_{pre}$. In Fig. 3.7, fatigue test data $\Delta\sigma_{exp}$ are shown as distributed around an ideal line. To assess the scatter of fatigue test data $\Delta\sigma_{exp}$ against prediction results $\Delta\sigma_{pre}$, statistical analyses were conducted. Sample mean $\bar{X}$ is described as:

$$\bar{X} = \frac{1}{p}\sum_{j=1}^{p} X_j \qquad (3.15)$$

where p is sample number and $X = \Delta\sigma_{exp}/\Delta\sigma_{pre}$. Sample variance S^2 is described as:

$$S^2 = \frac{1}{p-1}\sum_{j=1}^{p}\left(X_j - \bar{X}\right)^2 \qquad (3.16)$$

A confidence interval (CI) and a prediction interval (PI) are given as

$$\mathrm{CI} = \bar{X} \pm T_{p-1} S \frac{1}{\sqrt{p}} \qquad (3.17)$$

$$\mathrm{PI} = \bar{X} \pm T_{p-1} S \sqrt{1 + \frac{1}{p}} \qquad (3.18)$$

where $T_{p\text{-}1}$ has a Student's t-distribution with $p - 1$ degrees of freedom. Table 3.3 summarizes the results of the statistical analyses. The 90% PI for $\Delta\sigma_{exp}/\Delta\sigma_{pre}$ in Fig. 3.7(a) is 0.94 $\pm$ 0.15, and that in Fig. 3.7(b) is 1.00 $\pm$ 0.20.

Table 3.1 Chemical composition and mechanical properties of KA32.

Chemical composition %				Mechanical properties		
C	Si	Mn	P	Yield strength MPa	Tensile strength MPa	Elongation at fracture %
0.17	0.37-0.39	1.34-1.36	0.016-0.018	347-352	519-523	27-30

Table 3.2 Dimensions of test specimens and fatigue test results for imitation specimens [39].

No.	Load type	Main plate thickness t mm	Attached plate thickness t_p mm	Weld leg length d mm	Flank angle θ degree	Weld toe radius ρ mm	$\Delta\sigma$ at 2×10^6cycle MPa
1	Axial	12	12	6.4	45	1	205
2	Axial	22	12	6.4	45	1	208
4	Axial	80	12	6.4	45	1	196
5	Axial	40	22	8.4	45	1	140
6	Axial	40	40	12	45	1	141
7	Axial	40	80	20	45	1	130
8	Axial	22	22	8.4	45	1	162
9	Axial	80	80	20	45	1	123
11	Axial	22	12	6.4	45	3	242
12	Axial	40	22	8.4	45	0.5	122
13	Axial	40	22	8.4	45	3	223
5b	Bending	40	22	8.4	45	1	180
6b	Bending	40	40	12	45	1	182
8b	Bending	22	22	8.4	45	1	222

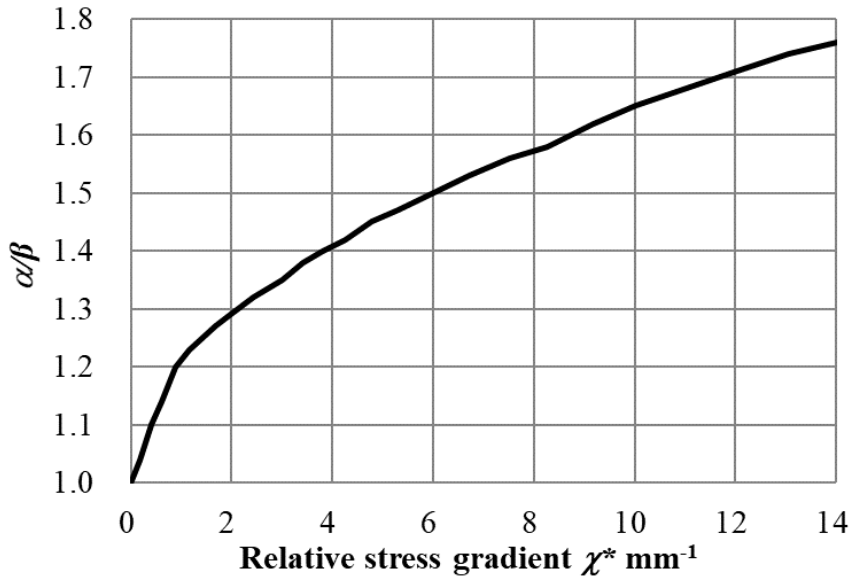

Fig. 3.6. Relationship between χ and α/β for steel with a yield stress class of 350 MPa [39].

Table 3.3 Results of the statistical analyses for $X = \Delta\sigma_{exp}/\Delta\sigma_{pre}$.

Series	Sample number p	Sample mean $\bar{X}$	Standard deviation S	90 % confidence interval	90 % prediction interval
Imitation specimen (FEM, Fig. 7(a))	13	0.94	0.08	$\bar{X} \pm 0.039$	$\bar{X} \pm 0.15$
Imitation specimen (Tsuji's formula, Fig. 7(b))	13	1.00	0.11	$\bar{X} \pm 0.055$	$\bar{X} \pm 0.20$
Cruciform welded joint (Tsuji's formula, Fig. 8)	12	1.00	0.12	$\bar{X} \pm 0.060$	$\bar{X} \pm 0.22$

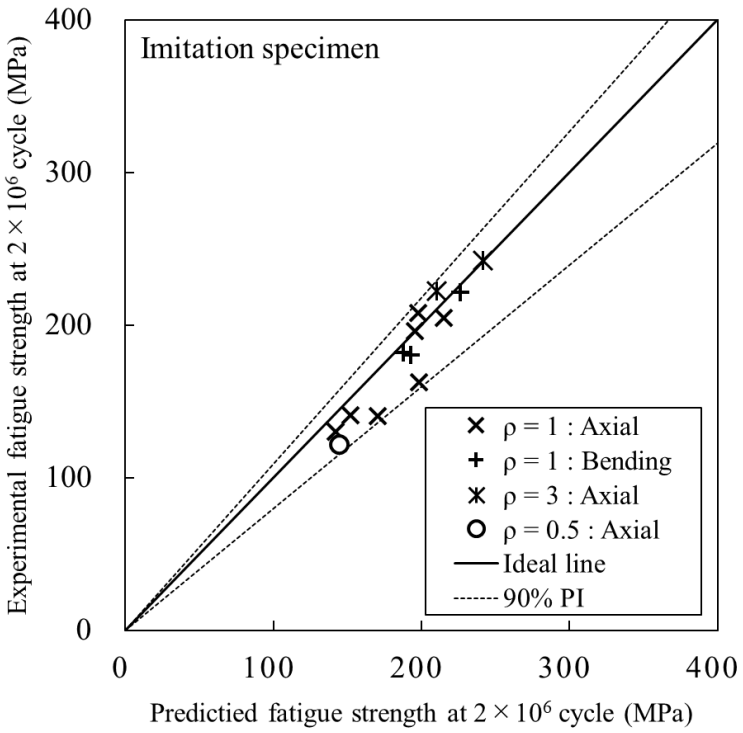

(a) Stress concentration factor calculated by FEM.

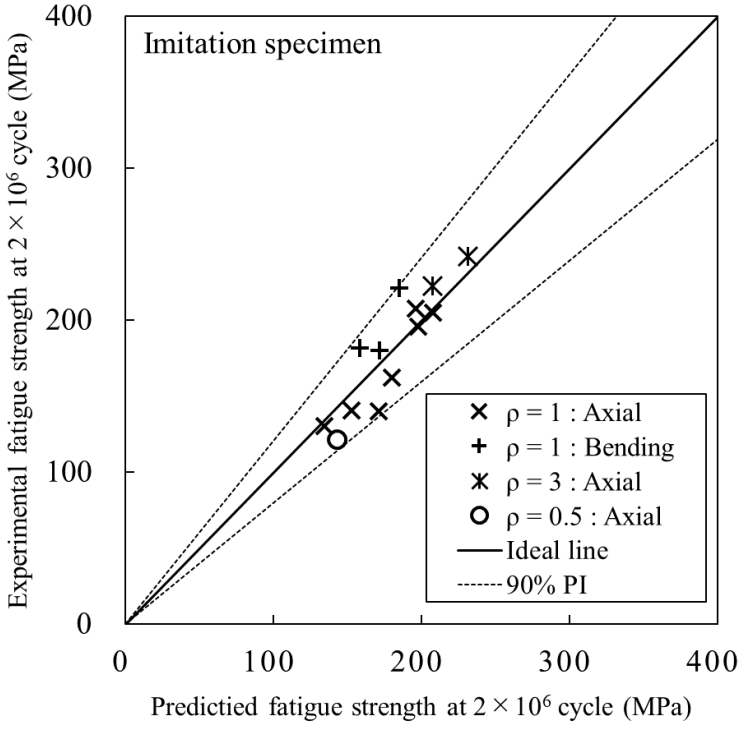

(b) Stress concentration factor calculated by formula.

Fig.3.7. Prediction results of fatigue strength for imitation specimens.

3.5.2. Welded joints

Parent materials were rolled steel SM490A for welded structures, the chemical composition, and mechanical properties of which are listed in Table 3.4 or alternatively, thermo-mechanically controlled processed (TMCP) YP32 steel (rule specified yield strength is 315 MPa and tensile strength is 440-590 MPa). Conditions of welded joints were as-welded, burr grinding, high frequency mechanical impact (HFMI), shot peening, and stress relief heat treatment (SR), respectively. Table 3.5 lists the dimensions of test specimens and fatigue test results for welded joints [39, 79]. Fatigue axial loading was applied to welded joints with stress ratio of 0.05 and test frequency of 1–5 Hz. Applied constant stress range $\Delta\sigma$ was in the range of 60 to 350 MPa. Reference specimens for the prediction of fatigue strength were as follows:

- Series B, G, U, S : t = 50 mm
- Series AW, and SR : t_p = 80 mm
- Series AWG : t = 80 mm

Fig. 3.8 shows the prediction results for the fatigue strength of welded joints, based on proposed geometric effect function G. Stress concentration factors of non-load-carrying cruciform welded joints were calculated using a formula reported by Tsuji [78] (see Appendix 2), for out-of-gusset welded joints, stress concentration factors were calculated by finite element analyses, the conditions of that were the same as in section 3.3. Fatigue test data $\Delta\sigma_{exp}$ were distributed around the ideal line shown in Fig. 3.8. Statistical analyses for the results of non-load-carrying cruciform welded joints were conducted to assess the scatter of fatigue test data $\Delta\sigma_{exp}$ against

prediction results $\Delta\sigma_{pre}$. The procedure for conducting statistical analyses was same as in section 3.5.1. The results of the statistical analyses are listed in Table 3.3. The 90% PI for $\Delta\sigma_{exp}/\Delta\sigma_{pre}$ of non-load-carrying cruciform welded joints was 1.00 ± 0.22, which was nearly the same as the results for imitation specimens when α was calculated using Tsuji's formula.

Table 3.4 Chemical composition mechanical properties of SM490A.

Chemical composition %				Mechanical properties			
C	Mn	P	S	Plate thickness mm	Yield strength MPa	Tensile strength MPa	Elongation at fracture %
≤0.23	≥ 2.5 × C	≤0.035	≤0.035	10	398	528	26
				22	366	526	28
				40	361	556	28
				50	346	544	33

Table 3.5 Dimensions of test specimens and fatigue test results for welded joints [39, 79].

Series	Parent material	Joint type	Condition	Main plate thickness t mm	Attached plate thickness t_p mm	Weld leg length d mm	Flank angle θ degree	Weld toe radius ρ mm	$\Delta\sigma$ at 2 × 10^6cycle MPa
B [39]	SM490A	cruciform	As-welded	10	10	8.2	69.5	0.62	116
				22	22	12.6	59.3	0.62	72
				40	40	16.4	54.6	0.62	70
				50	50	18.0	66.0	0.62	66
G [39]	SM490A	cruciform	Burr grinding	22	22	11.8	41.5	9.35	164
				40	40	17.5	43.8	9.35	155
				50	50	18.8	42.0	9.35	137
U [39]	SM490A	cruciform	HFMI	10	10	8.5	52.7	1.42	226
				22	22	13.2	41.8	1.42	209
				40	40	17.0	42.9	1.42	159
				50	50	19.2	46.3	1.42	167
S [39]	SM490A	cruciform	Shot peening	10	10	7.3	59.2	0.98	157
				40	40	16.7	50.0	0.98	92
				50	50	19.5	70.7	0.98	82
AW[79]	TMCP	cruciform	As-welded	40	22	8.4	45	1	126
				40	80	12	45	1	89
SR[79]	TMCP	cruciform	SR	40	22	8.4	45	1	124
				40	80	12	45	1	106
AWG[79]	TMCP	gusset	As-welded	12	12	6.4	45	1	97
				22	12	6.4	45	1	98
				40	12	6.4	45	1	97
				80	12	6.4	45	1	107

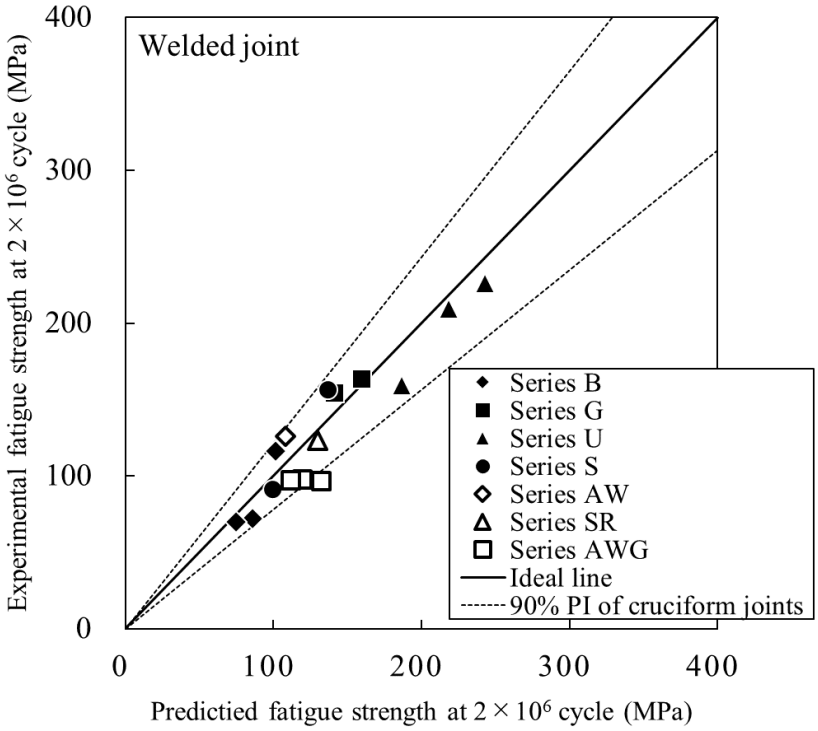

Fig. 3.8 Prediction results of fatigue strength for welded joints.

3.6 Thickness correction exponent *n* based on proposed geometric function

Proposed geometric function *G* can describe thickness correction exponent *n*. In this section, thickness correction exponent *n* for typical welded joints was estimated based on the proposed geometric function *G*. The joint types in this investigation were non-load-carrying cruciform welded joints, Tee welded joints, and out-of-plane gusset welded joints, respectively. Joint types, dimensions and load types for non-load-carrying cruciform welded joints and Tee welded joints are described in Appendix 3, and that of out-of-plane gusset welded joints are shown in Appendix 1. The series names of non-load-carrying cruciform welded joints and Tee welded joints were designed to divide cases based on characteristics of joint types, pattern of changing dimensions, and load types. Figure 3.9 shows schematic drawings of the pattern of changing dimensions for non-load-carrying cruciform welded joints and Tee welded joints. Stress concentration factor α for non-load-carrying cruciform welded joints and Tee welded

joints was calculated using the formula reported by Tsuji (see Appendix 2), and that of out-of-plane gusset welded joints was calculated by finite element analyses, the same as employed in section 3.3. Reference plate thickness was adopted as 22 mm. Thickness correction exponents were calculated by least squares fitting using Eq. (3.19).

$$G^n \cdot t = D \qquad (3.19)$$

where D is the constant. If the trend of the thickness effect deviated from the double logarithmic linear relationship described Eq. (3.19), thickness correction exponent n was not calculated.

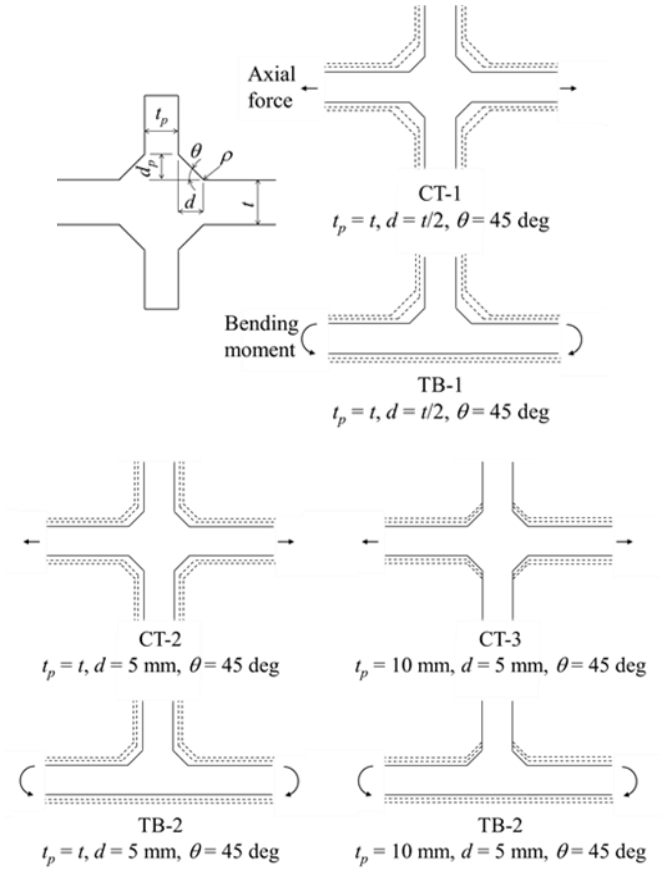

Fig. 3.9. Schematic drawings representing the pattern of changing dimensions.

3.6.1 Non-load-carrying cruciform welded joints

Figure 3.10 indicates the relationships between geometric effects function *G* and main plate thickness *t* for non-load-carrying cruciform welded joints with applied axial loading. Thickness correction exponent *n* for CT-1 ranged from 0.28 to 0.36, and from 0.15 to 0.20 for CT-2 ranges. These results showed that for thickness effect, where weld leg length *d* was the constant value regardless of increasing main plate thickness *t*, a low value of *n* was indicated compare with where weld leg length *d* had increased alongside in main plate thickness *t*. Furthermore, CT-3 which changed only main plate thickness did not almost indicate a decrease of the geometric effect function *G* from the value of the geometric effect function at a reference plate thickness of 22 mm alongside an increase in main plate thickness *t*.

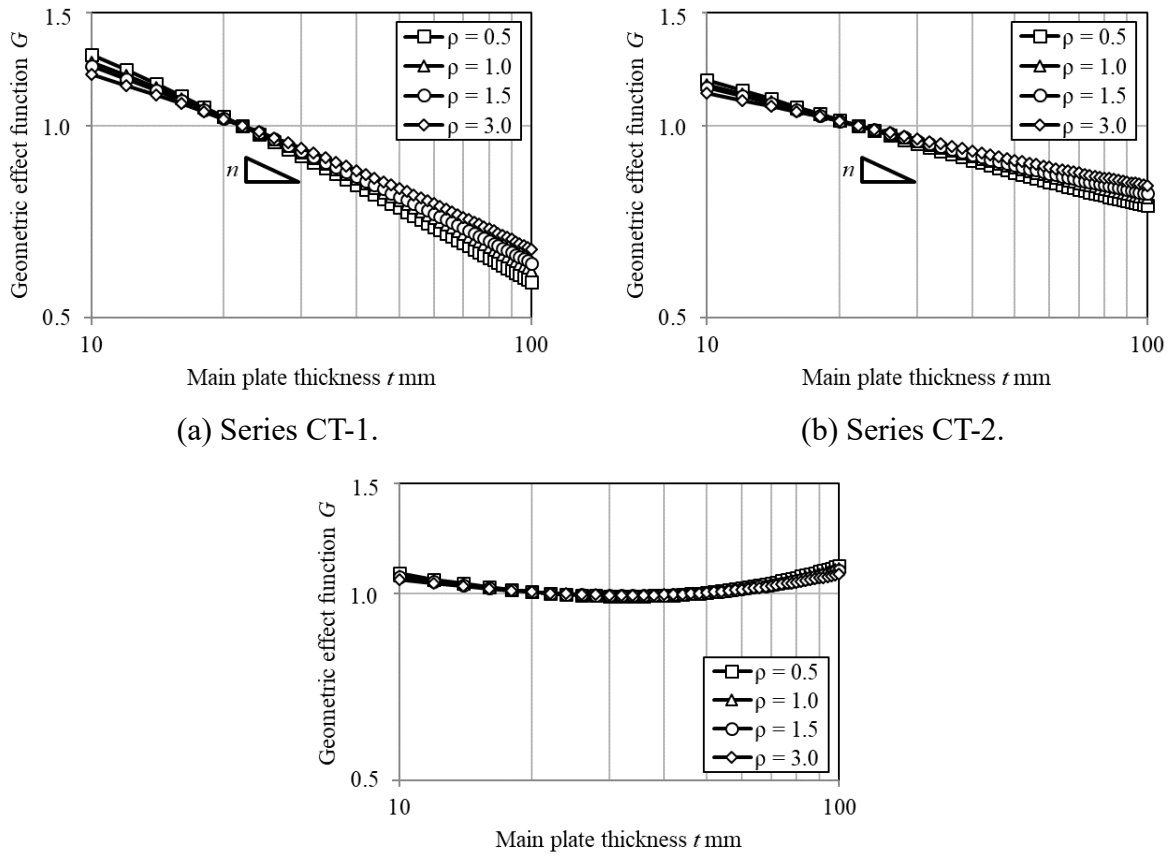

(a) Series CT-1.

(b) Series CT-2.

(c) Series CT-3.

Fig. 3.10. Relationships between geometric effect function and main plate thickness for cruciform welded joints (Axial loading).

3.6.2 Tee welded joints

Figure 3.11 illustrated the relationships between geometric effect function G and main plate thickness t for Tee welded joints, which were applied to bending loading. Thickness correction exponent n for TB-1 ranged from 0.25 to 0.32. The trend of the thickness effect for TB-2 and TB-3 was similar to that for CT-3.

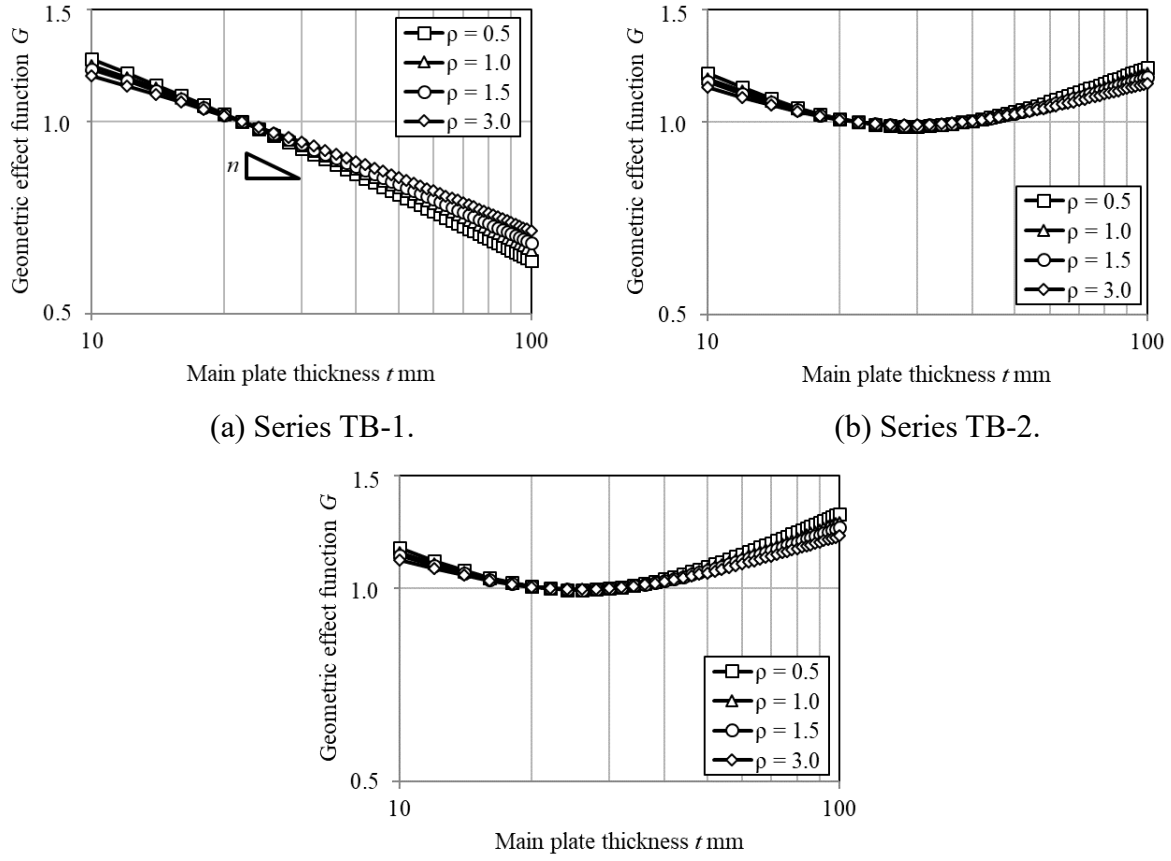

(a) Series TB-1.

(b) Series TB-2.

(c) Series TB-3.

Fig. 3.11. Relationships between geometric effect function and main plate thickness for welded Tee joint (bending loading).

3.6.3 Out-of-plane gusset welded joints

Results for the prediction of thickness correction exponent n in out-of-plane gusset welded joints, which applied axial loading, are shown in Fig. 3.12. The dimensions of out-of-plane gusset welded joints are listed in Table 3.1 (c). Thickness correction exponent n for out-

of-plane gusset welded joints ranged from 0.06 to 0.12, and was lower than that of cruciform welded joints and Tee welded joints. In the IIW recommendations [10], the thickness correction exponent *n* for out-of-plane gusset welded joints is 0.1. The obtained results for thickness correction *n* exponent for out-of-plane gusset welded joints were close to the value of the IIW recommendations [10]. Thickness correction exponent *n* was of little relevance to gusset length *k*. Main plate width *W* slightly affected the thickness correction exponent *n* for out-of-plane gusset welded joints.

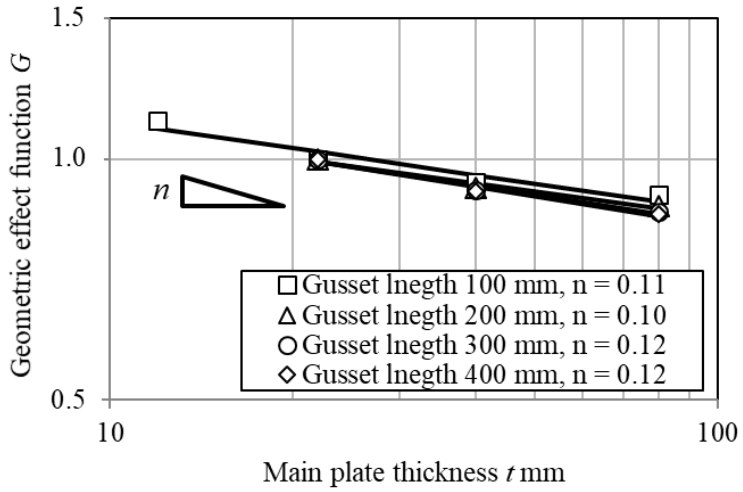

(a) Effect of gusset length.

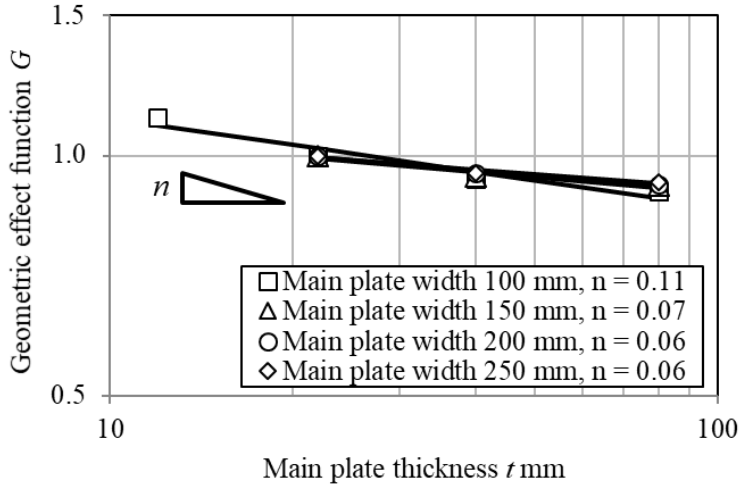

(b) Effect of main plate width.

Fig. 3.12. Relationships between geometric effect function and main plate thickness for out-of-plane gusset welded joints.

3.6.4 Effect of weld toe radius

The relationships between the predicted thickness correction exponents and weld toe radius are shown in Fig. 3.13, where thickness correction exponent indicates a decrease alongside an increase in toe radius ρ.

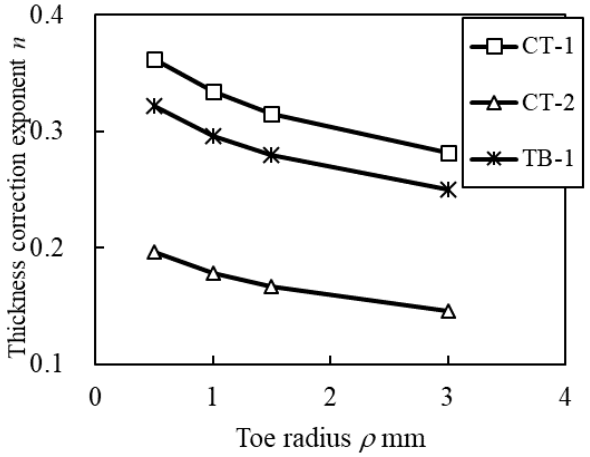

Fig. 3.13. Relationships of thickness correction exponent and toe radius.

3.7 Comparison of axial load and bending load

The fatigue limit ratio in the axial loading condition and in the bending loading condition, based on proposed geometric effect function G (Eq. (3.12)) can be given as follows:

$$\begin{aligned}\gamma &= \frac{\sigma_{wwm}}{\sigma_{wwb}} \\ &= \frac{G_m \sigma_{ww(ref)}}{G_b \sigma_{ww(ref)}} \\ &= \frac{\alpha_b}{\alpha_m} \frac{J_{mi}(\rho)}{J_{bi}(\rho)} \\ &= \frac{\alpha_b}{\alpha_m} \end{aligned} \qquad (3.20)$$

where γ is referred to as the bending correction coefficient, the subscript m indicates the axial loading condition and the subscript b indicates the bending loading condition. In the fatigue design recommendations of the Japanese Society of Steel Construction [80], bending correction

coefficient γ is 0.8, regardless of welded joint types and dimensions of welded joints. Figure 3.14 shows the predicted results of bending correction coefficient γ for non-load-carrying cruciform welded joints, based on proposed geometric effect function G. Figure 3.14(a) illustrates the effect of main plate thickness t on bending correction factor γ. Bending correction factor γ increased alongside an increase in main plate thickness t. In contrast, bending correction factor γ decreased alongside an increase in the sum of attached plate thickness tp and weld leg length d times two, as shown Fig 3.14 (b). Based on Fig. 3.14 (c), weld toe radius did not almost affect the bending correction factor γ.

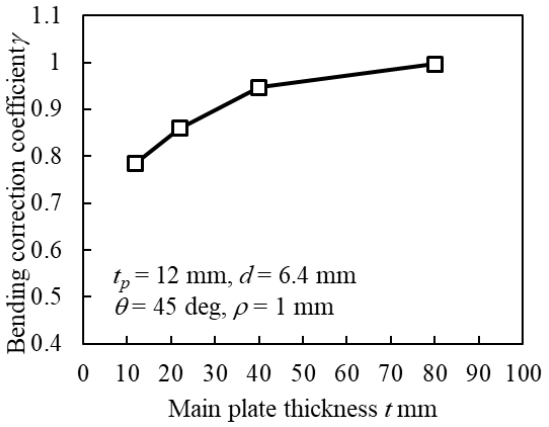

(a) Effect of mail plate thickness t.

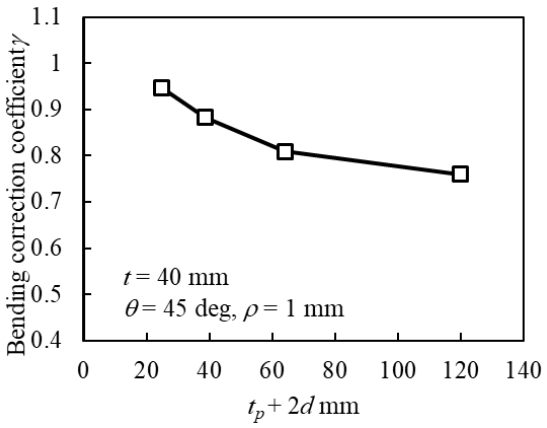

(b) Effect of attached plate thickness t_p and weld leg length d.

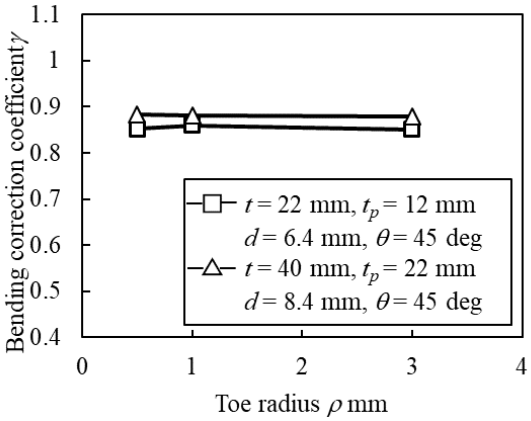

(c) Effect of toe radius ρ.

Fig. 3.14. Bending correction coefficient γ for non-load-carrying cruciform welded joints.

3.8 Discussion

3.8.1 Scatter of fatigue data against prediction results

Fatigue test data for welded joints showed scatter against predicted fatigue strength results, based on proposed geometric effect function G, as shown section 3.5.2. The scatter for welded joints was almost the same as for imitation specimens (see Table 3.3). The reason for these scatter results remains unclear at present, however, scatter of relationship between α/β and χ^* (Siebel diagram as shown in Fig. 3.2) may have been one of the primary causes for this scatter. There is some scatter in the Siebel diagram [75], however, number of data was not enough to conduct statistical analysis. Thus, more experimental work is necessary to clarify this issue.

3.8.2 Thickness correction exponent *n*

Thickness correction exponent n, a slope indicating the double logarithmic linear relationship between geometric effect function G and main plate thickness t, depended on stress concentration factor α at the weld toe, since geometric effect function G was a function of stress concentration factor α, as shown in Eq. (3.12). For cruciform joints and Tee joints, the double logarithmic linear relationships between geometric effect function G and main plate thickness t indicated a negative slope when attached plate thickness t_p and weld leg length d were directly proportional to main plate thickness (Fig. 3.10 (a), Fig. 3.11 (a)). The reason for these results was the increase in stress concentration factor α alongside an increase in main plate thickness t. Thickness correction exponent n indicated a decrease alongside an increase in weld toe radius ρ (Fig. 3.13). This is because a reduction in the degree of an increase of stress concentration factor α with an increase in weld toe radius ρ, as is evident from Tsuji's formula (Appendix 2).

On the other hand, there were instances where the relationship between geometric effect function G and main plate thickness t indicated non-linearity on a double logarithm (Fig. 3.10 (c), Fig. 3.11 (b) and Fig. 3.11 (c)). This occurred because stress concentration factor α represented a decrease alongside an increase in main plate thickness t when attached plate thickness t_p and weld leg length d were sufficiently small, compared with main plate thickness t. The condition in which stress concentration factor α decreased alongside an increase in main plate thickness t was also associated with joint type and loading type.

Thickness correction exponent n for out-of-plane gusset welded joints was low compared with cruciform welded joints and Tee welded joints. The reason for this was that changing rate of the stress concentration factor α for out-of-plane gusset welded joints indicates low level because gusset length k is sufficient long against main plate thickness in this study.

3.8.3. Bending correction factor

Bending correction factor γ was related to geometric dependence of the stress concentration factor α for two kinds of loading types, axial loading, bending loading, respectively, as shown in Eq. (3.20). Main plate thickness t, attached plate thickness t_p and weld leg length d had influence on the bending correction factor γ (Fig. 3.14 (a), Fig. 3.14 (b)), because of the difference of geometric dependence of stress concentration factor α for axial loading and that for bending loading. In contrast, weld toe radius was less effective in the case of bending correction factor γ, as shown Fig. 3.14 (c). The reason for this result is that the geometric dependence of stress concentration factor α for axial loading is nearly the same as that for bending loading.

3.9 Conclusions

This paper clarified that the relative stress gradient of welded joints depended only on weld toe radius, regardless of welded joint and loading type, based on results of stress analyses for non-load-carrying cruciform joints, out-of-plane gusset joints, and welded structural models. Based on these results, we derived the geometric effect function described by the stress concentration factor and the function of weld toe radius. Results of testing the validity of the proposed geometric effect function and the parametric studies of the geometric effect on fatigue strength for welded joints, based on the proposed geometric effect function are summarized below.

- Fatigue test data $\Delta\sigma_{exp}$ were distributed around an ideal line, which denoted fatigue test data $\Delta\sigma_{exp}$ as being equal to prediction results $\Delta\sigma_{pre}$ based on the proposed geometric effect function. The 90% PI for $\Delta\sigma_{exp}/\Delta\sigma_{pre}$ of non-load-carrying cruciform welded joints was 1.00 ± 0.22.

- Parametric studies revealed the trend for geometric effect on fatigue strength for cruciform joints, Tee welded joints, and out-of-plane gusset, respectively. Not only main plate thickness, but attached plate thickness, weld toe radius, and weld leg length also affected the fatigue strength of welded joints.

- Based on the proposed geometric function, it was clarified that the bending correction coefficient had been affected by the geometries of welded joints excluding weld toe

radius. The bending correction coefficient for non-load-carrying cruciform welded joints was also indicated by parametric studies.

Chapter 4 Fatigue life prediction for 9 % Ni steel butt welded joints

4.1 Introduction

The geometric effect, the difference of cyclic stress-strain properties between parent material, the heat affected zone (HAZ), and weld metal, and the mean stress effect by welding residual stress and applied stress influence the fatigue strength of welded joints. Thus, to assess fatigue life for welded structures with high accuracy, it is necessary to comprehensively consider these effects. There exists literature on the investigation of each effect of the fatigue strength of welded joints. However, to the best of the author's knowledge, no reports have comprehensively considered these effects on the assessment of fatigue crack initiation life and fatigue crack propagation life for welded joints.

Lawrence et al. [40] reported assessment of fatigue crack initiation life by focusing on local strain at the weld toe. Similarly, Usami et al. [41] reported about the fatigue crack initiation life of welded joints. These references, however, did not consider the details of welding stress distribution. Teng et al. [42] investigated the mean stress correction method for crack initiation fatigue life. They pointed out that the Smith-Watson-Topper (SWT) mean stress correction approach [43] approximates experimental data better than the Manson-Halford correction [44], which is the modified Morrow correction [45]. Levieil et al. [46] applied the Morrow criterion to show the assessment results of the fatigue crack initiation life for welded T-joints. Some results indicated over-conservative estimations compared with experimental results. Ince et al. [47] investigated the prediction capabilities of Morrow correction and SWT approach for parent materials. They revealed that the prediction results using the SWT approach is good agreement with the experimental results of parent materials. Ladinek et al. [48] assessed the fatigue crack

initiation life for welded test specimens by considering the real weld geometry. They obtained the weld geometry by using a 3D laser scanner. Hiraide et al. [49] simulated the stress-strain behavior for a cruciform welded joint under fatigue loading. This study considered the effect of the stress-strain response of HAZ.

Maddox [51] investigated fatigue crack propagation for a semi-elliptical surface crack at the toe of a longitudinal non-load-carrying gussets fillet weld. Gurney [36] described the effect of the weld leg length on the fatigue strength of welded cruciform joints by using fatigue crack growth analysis, assuming that an initial crack existed at the weld toe. Gadallah et al. [52] studied the effect of welding residual stress on the stress intensity factor and fatigue crack propagation.

Itoh et al. [53] showed the prediction results of the crack initiation life and the crack propagation life for butt welded joint. However, they did not consider the detail of welding residual stress distribution and the effect of the cyclic stress-strain property of HAZ. Zerbst et al. [54] proposed a method to determine the fatigue strength of welded joints based on fracture mechanics. The prediction results based on this method indicate over-conservative or non-conservative estimations for typical welded joints. The reasons for these results have to date not been clearly identified.

In this study, we investigated the prediction method of fatigue life for welded joints, of which the parent material is 9% Ni steel. 9% Ni steel, which has superior fracture toughness at cryogenic temperatures. It is a candidate material for on-land liquefied natural gas (LNG) storage tanks, offshore LNG units, and LNG carrier tanks [81, 82]. Because 9% Ni steel shows the phase transformation during the welding (heating) and cooling process [83–85], similar to

high tensile strength steel, it is necessary to take into account the behavior of the phase transformation in the estimation of welding residual stress distribution. A guide for building and classing for liquefied gas carriers with independent tanks [1] describes the design S-N curves for 9% Ni steel welded joints. Many experiments were conducted on the fatigue strength of 9% Ni steel welded joints [17, 18–22]. However, to our knowledge, the prediction of the fatigue life for 9% Ni steel has not been studied. Gioielli et al. [18, 19] presented fatigue test results for typical welded joints of 9% Ni steel. Lee et al. [17] showed the improvement rates of fatigue life at LNG temperatures compared to room temperature. Tsunenari [20] studied the influence of welding distortion for fatigue strength on 9% Ni steel welded joint. Kishimoto [21] investigated the effect of undercut for fatigue strength on 9% Ni steel. Kamata et al. [22] presented the mean stress effect for fatigue strength on 9% Ni steel welded joints.

This study aimed to propose a prediction method of fatigue life for welded joints, which can be comprehensively considered as the geometric effect, the difference of cyclic stress-strain properties between parent material, the HAZ, and weld metal, and the mean stress effect. We first performed fatigue tests for multi-pass butt welded joints of 9% Ni steel at room temperature, to compare with prediction results. The finite element models to calculate welding residual stress field and stress-strain response under fatigue loading were made based on the real geometry of welded joints. A welding simulation estimated the welding residual stress distribution. The welding simulations were conducted using a thermal elastic-plastic finite element analysis (FEA). The thermal elastic-plastic FEA considered the phase-transformation of 9% Ni steel during the welding process. To clarify the stress-strain behavior of welded joints under fatigue cyclic loading, we conducted a nonlinear structure FEA. The cyclic stress- strain

properties of the structure FEA were divided into the parent material area, the HAZ area, and the weld metal area. Based on the literature data of fatigue crack initiation life, we proposed a new unified relationship between total strain and fatigue crack initiation life, regardless of the material type. We applied the SWT approach to the estimation of fatigue crack initiation life as the mean stress correction. Fatigue crack propagation life was estimated using the Paris-Elber law [86] to consider the mean stress effect. The prediction results of fatigue life using the proposed method were good agreement with the experimental results. Furthermore, to evaluate the validity of the proposed method for fatigue crack initiation life and fatigue crack propagation life, we conducted additional fatigue test and compared it with the prediction results.

4.2 Fatigue test of welded joints

Fatigue tests were conducted for two types of butt welded joints that differ in welding pass sequence and welding conditions.

4.2.1 Material and specimen

Table 4.1 lists the chemical composition of the parent material and the weld metal. Table 4.2 lists the mechanical properties of the parent material and the weld metal. The parent material is 9% Ni steel, and the weld metal is 70% Ni super-alloy. Fig. 4.1 shows the geometry and dimensions of the fatigue test specimen, and Fig. 4.2 shows the welding cross-section and the schematic drawing of the pass sequence. Two kinds of butt welded joints are designated as type S and type M, as shown in Fig. 4.2. Type S was welded by manual metal-arc welding, and

type M was welded by gas-shielded metal-arc welding. Table 4.3 lists the welding conditions. Fig. 4.3 shows the Vickers hardness distribution of the welded joints, showing almost no difference between the Vickers hardness distributions of type S and that of type M. The Vickers hardness of HAZ is higher than that of the parent material and the weld metal, with a range of 322 to 377 HV0.3.

Table 4.1 Chemical composition of parent material and weld metal (%).

(a) 9% Ni steel (parent material).

C	Si	Mn	P	S	Ni
0.05	0.22	0.64	0.003	0.0006	8.96

(b) 70% Ni super-alloy (weld metal).

C	Si	Mn	P	S	Ni
0.08	0.28	2.3	0.003	0.002	67.1
Cu	Mo	Nb	Fe	W	Nb+Ta
13.6	3.9	1.5	10.0	0.7	1.5

Table 4.2 Mechanical properties of parent material and weld metal.

Material	0.2% proof stress MPa	Tensile strength MPa	Elongation at fracture %
9% Ni steel	681	719	30
70% Ni super-alloy	445	698	42

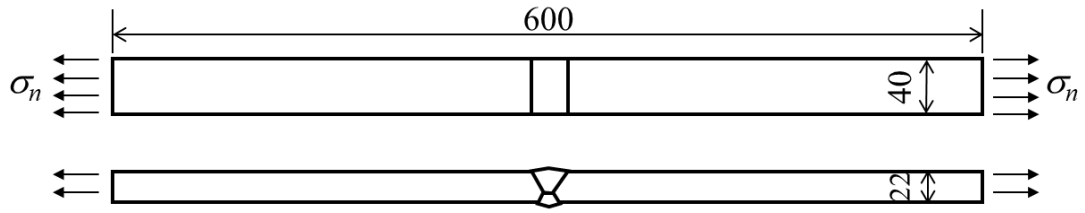

Fig. 4.1. Geometry of welded joint.

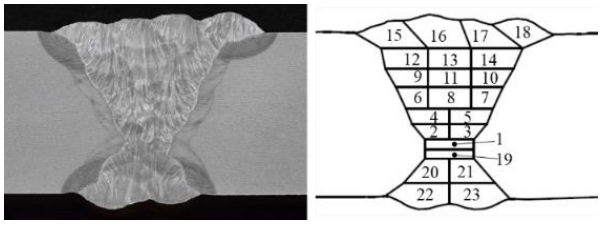

(a) Type S.

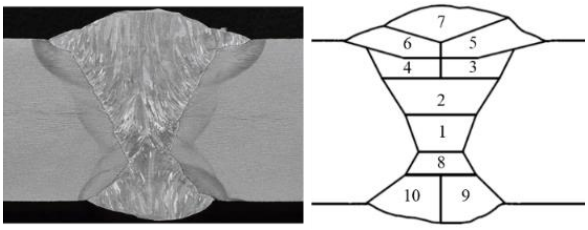

(b) Type M

Fig. 4.2. Welding cross section and pass sequence.

Table 4.3 Welding conditions.

Type	Current A	Voltage V	Speed cm/min
S	125	23 25	12.5 32.3
M	230	32	20.1 48.7

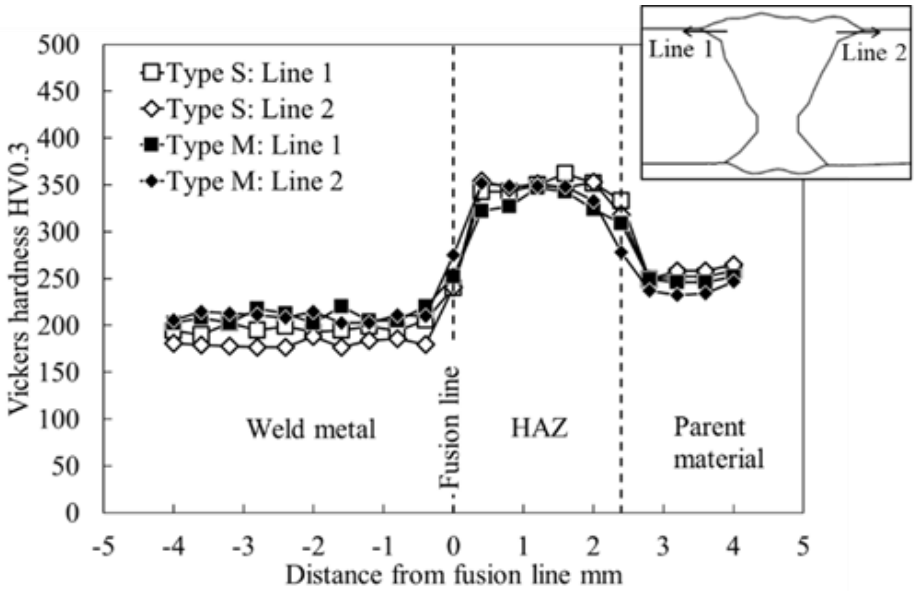

Fig. 4.3. Vickers hardness distribution around weld toe.

4.2.2 Test conditions

The servo-hydraulic actuator conducted the constant amplitude fatigue tests at room temperature under load control. Axial fatigue load was applied to the specimens in a sinusoidal

waveform with a frequency of 3–8 Hz and a stress ratio of R = 0.05. The applied constant nominal stress range $\Delta\sigma_n$ was in the range of 104 to 299 MPa.

4.2.3 Fatigue test results

For all the fractured specimens, the fatigue crack initiated at the weld toe, as shown in Fig. 4.4. Fig. 4.5 shows the fatigue test results including that of the references [20, 21]. The stress ratio and the main plate thickness of the reference data are similar to our fatigue tests. The fatigue test results of the references indicate almost the same level for fatigue strength of our fatigue test. In this section, we shall assume that the effects of the differences in the stress ratio and the main plate thickness are small for these test results, to conduct following statistical analysis. The mean S-N curve of these test results was calculated by the least squares fitting for fatigue test data using Eq. (4.1) to yield the following:

$$\Delta\sigma_n{}^m \cdot N_f = C \qquad (4.1)$$

where Nf is the number of cycles to failure, and m and C are the constants. Table 4.4 lists the constants of the mean S-N curve and that of the mean-minus-two-standard-deviation curve, which is associated with a 97.7% probability of survival. The design S-N curve for 9% Ni steel butt welded joints by the American Bureau of Shipping (ABS) [1], in Fig. 4.5, gives a non-conservative assessment.

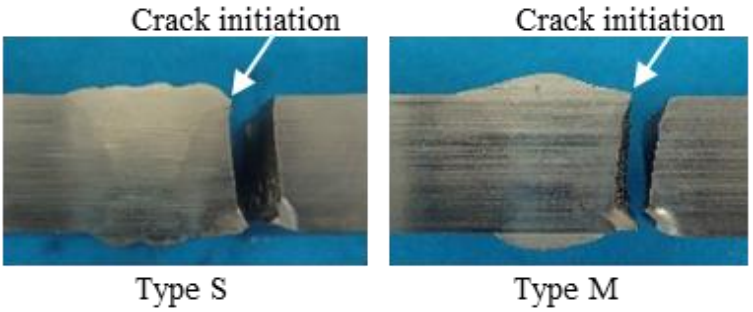

Fig. 4.4. Fatigue crack initiation point.

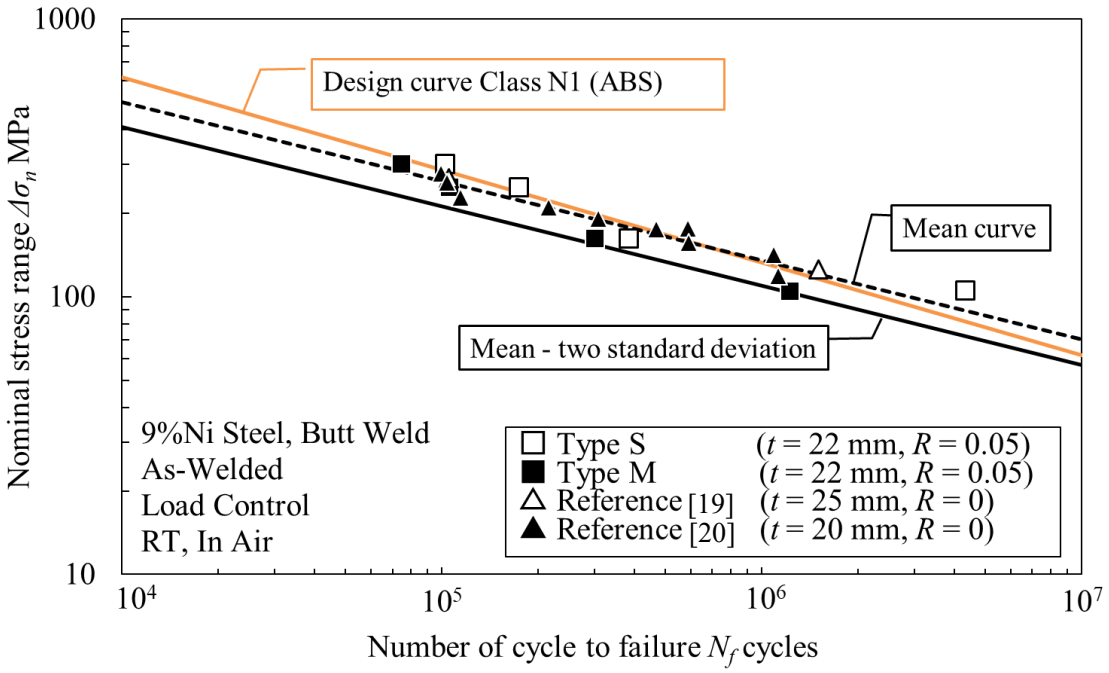

Fig. 4.5. Fatigue test results.

Table 4.4 S-N curve parameters.

	S-N curve parameters		Fatigue strength at 2×10^6 cycle MPa
	C	m	
Mean	2.93×10^{13}	3.51	111
Mean 2 × standard deviation	1.42×10^{13}	3.51	90
Design curve: Class N1 (ABS)	2.34×10^{12}	3.00	105

4.3 Fatigue life prediction method for welded joint

4.3.1 Procedure

Fig. 4.6 shows the flow diagram of the proposed fatigue life prediction method for welded joints. First, a welding simulation that consists of thermal analysis and thermal elastic-plastic analysis calculates the residual stress field. A nonlinear structural analysis then calculates the stress-strain response under cyclic fatigue loading, the first step of which is the welding residual stress field. The strain-life method, which considers the mean stress effect using the SWT mean stress correction approach, is combined with the nonlinear structural analysis result and employed to estimate fatigue crack initiation life. The linear fracture elastic mechanics are employed to estimate fatigue crack propagation life. To calculate the stress intensity factor range under fatigue loading, the calculation method of the stress intensity factor based on the linear fracture mechanics is combined with the structure analysis result. The Paris-Elber law is applied to consider the mean stress effect in the fatigue crack propagation rate. The total fatigue life to failure N_f is described as:

$$N_f = N_c + N_p \qquad (4.2)$$

where N_c is the fatigue crack initiation life, and N_p is the fatigue crack propagation life.

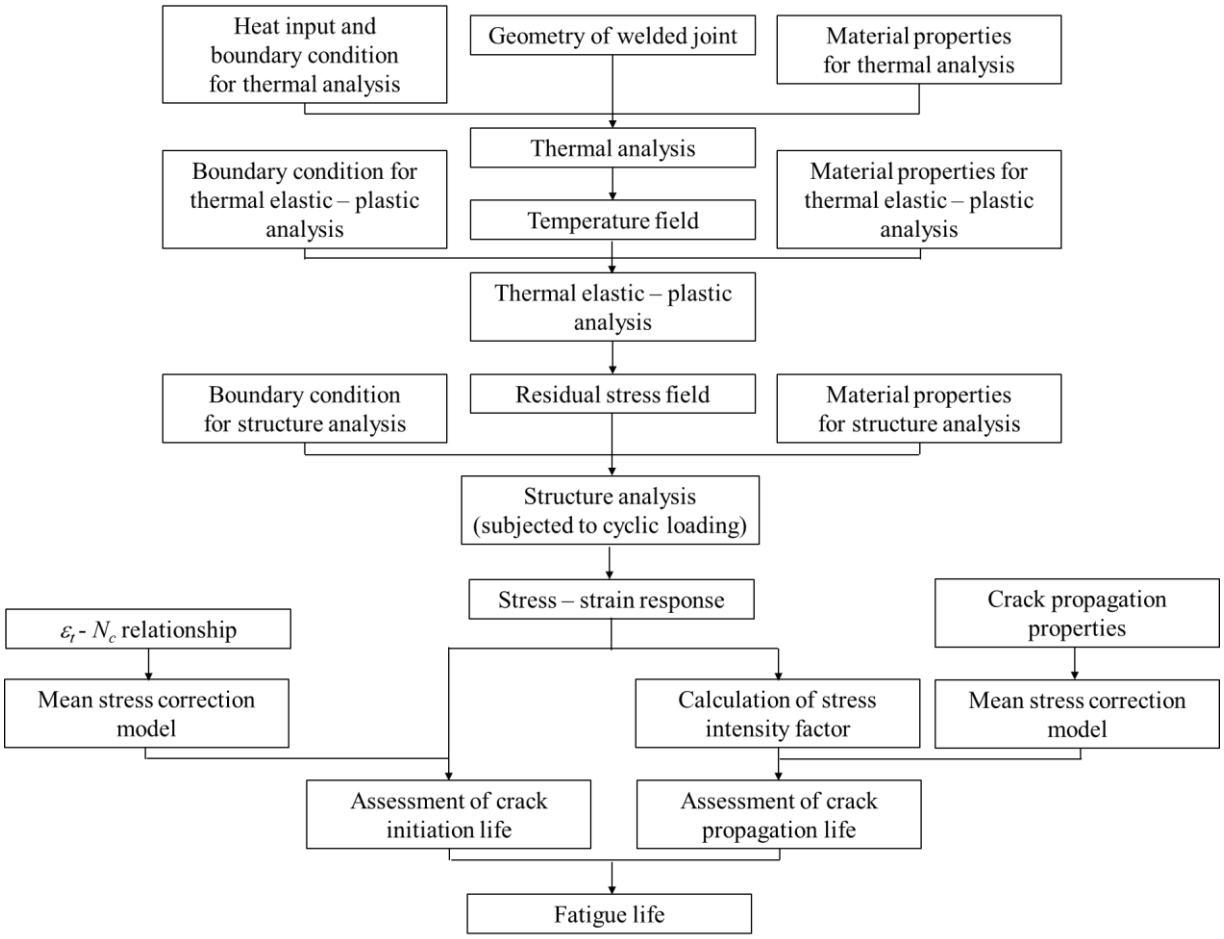

Fig. 4.6. Flow diagram of fatigue life prediction for welded joints.

4.3.2 Finite element analysis

The welding simulation [87, 88], consisting of thermal analysis and thermal elastic-plastic analysis, and the nonlinear structure analysis under fatigue loading, were conducted for type S and type M welded joint specimens using commercial FE code ABAQUS 2018.

4.3.1.1 Finite element model

Fig. 4.7 shows the finite element models of type S and type M welded joint specimens. This study used the two-dimensional symmetric model. To consider the geometric effect, the finite element models were made from the real weld surface geometry that was scanned using the laser scanner HP-L-20.8 on Absolute Arm 7530SE. The element size around the weld toe

was about 0.1 mm which is set by referring to the recommended mesh size for the calculation of effective notch stresses at weld to in the International Institute of Welding (IIW) recommendations [10]

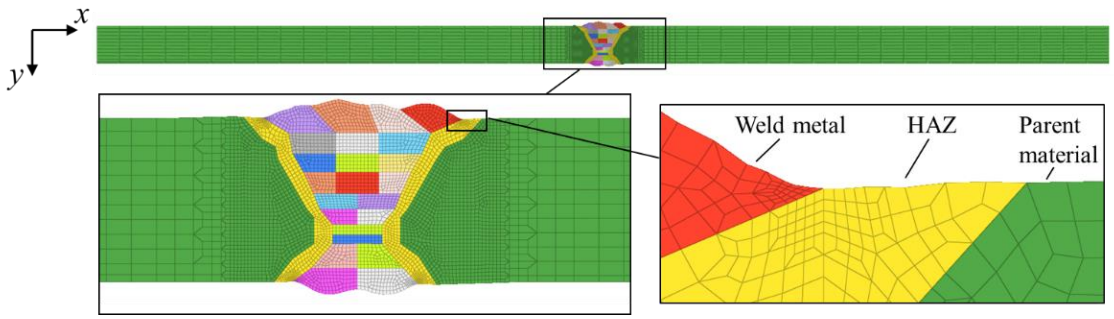

(a) Type S.

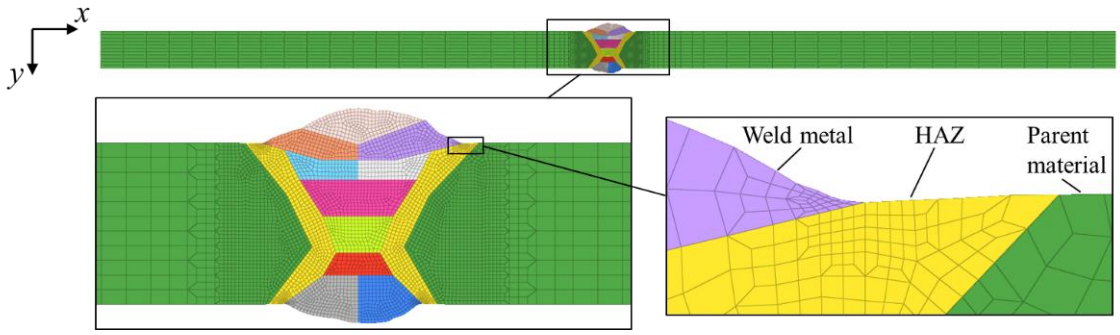

(b) Type M.

Fig. 4.7. Finite element model.

4.3.1.2 Welding simulation

Before the thermal elastic-plastic analysis, thermal analysis which represents the thermal process during welding was performed to obtain the temperature history for all nodes. The welding process was simulated by applying distributed heat flux (DFLUX in ABAQUS) for each pass, which was calculated from the electric power of the arc energy (Table 4.3), the arc efficiency for welding, and the volume of weld pool for each pass. We assumed that the arc efficiency for welding is 70%, as reported by Lee et al. [89].

To simulate weld metal deposition, we used the model change command, which controls removal or addition of elements, in ABAQUS. At the inception of the thermal analysis, the elements of all the welding passes are inactive. Before the first welding pass, the elements of the first pass are activated. The elements of the next welding pass are activated at once after the completion of the previous weld pass. The initial temperature of the specimen and ambient temperature for the thermal analysis was set to 20°C, and the convective heat coefficient on all the surface was assumed the value of 10 W/m^2 K [90]. The element type for the thermal analysis was the 4-node linear heat transfer quadrilateral. Fig. 8 shows the temperature-dependent physical properties that are used in the thermal analysis, as reported in the literature [89].

The thermal elastic-plastic analysis uses temperature distribution and the history obtained from the thermal analysis as input thermal loading to calculate the welding residual stress field. The finite element models of the thermal elastic-plastic analysis, except the element type, were the same as the thermal analysis. The element type for the thermal elastic-plastic analysis was a 4-node plane strain element. The perfect elastic-plastic model was employed to the thermal elastic-plastic analysis. Fig. 4.8 shows temperature-dependent material properties, as reported in the literature [89]. Fig. 4.9 shows the phase transformation in 9% Ni steel occurring during the welding process [83]. In the thermal elastic-plastic analysis, the user subroutine for ABAQUS, which traces the relationship between strain and temperature including the phase transformation, was used for 9% Ni steel. However, the weld metal does not indicate the phase transformation; therefore, the temperature-dependent thermal expansion coefficient, as shown in Fig. 4.8 (b), was applied for the weld metal. The Poisson's ratio of all material was assumed temperature-independent, at the value of 0.3.

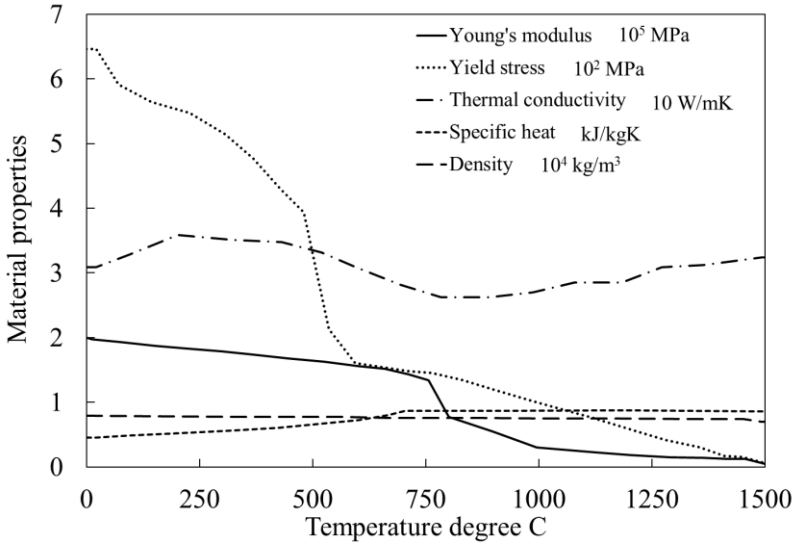

(a) 9% Ni steel (parent material).

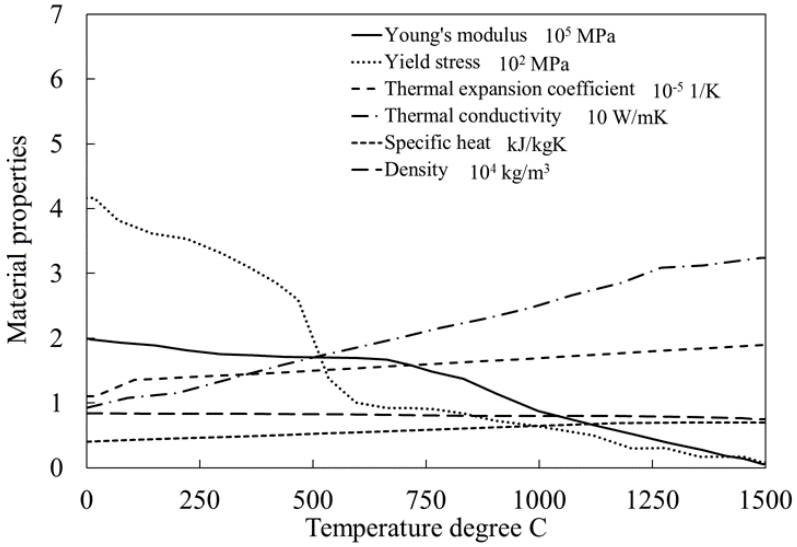

(b) 70% Ni super-alloy (weld metal).

Fig. 4.8. Temperature-dependent material properties [89].

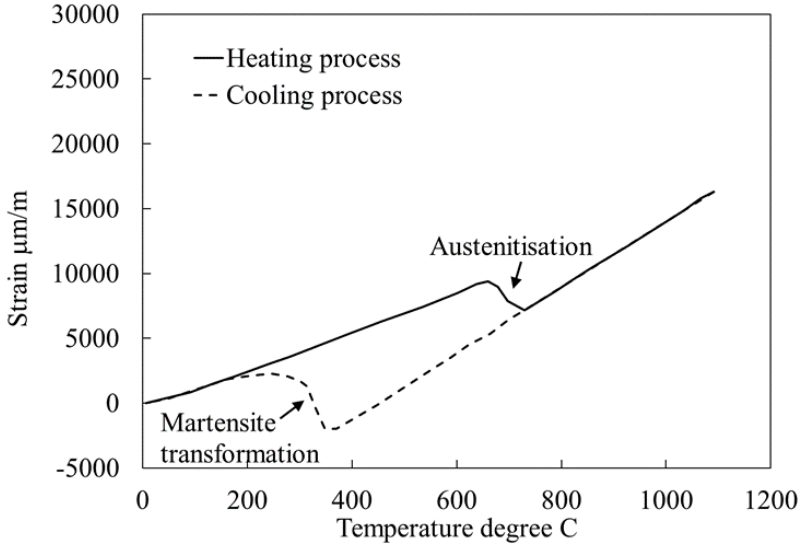

Fig. 4.9. Behaviors of thermal strain of 9% Ni steel [83].

4.3.1.3 Structure analysis

To obtain the stress-strain response under cyclic fatigue loading, the nonlinear structure analysis was performed. The finite element models of the nonlinear structure analysis were the same as the thermal elastic-plastic analysis, including the element type. The first step of the nonlinear structure analysis was the welding residual stress files obtained from the welding simulation. The cyclic fatigue loading was applied using the distribution load command, as shown in Fig. 4.1.

The cyclic stress-strain curves of the materials, namely, the parent material, the HAZ, and the weld metal, are necessary to calculate the stress-strain response of welded joints under cyclic fatigue loading. The cyclic stress-strain curve of the parent material reported by Iida [91] was employed to the nonlinear structure analysis, and the incremental step tests [92, 93] were performed for the weld metal and simulated HAZ to obtain the cyclic stress-strain curves. Fig. 4.10 shows the geometry of the specimens, which is based on the ASTM E606/E606M-19e1 [94], for the incremental step test. Fig. 4.11 shows the schematic drawing of specimen sampling for the weld metal from the butt welded joints. It is difficult to sample the specimen of HAZ

from the butt welded joint; therefore, the incremental step test for the simulated HAZ was conducted.

Fig. 4.12 shows the thermal history for the simulated HAZ sample. The thermal history was determined under the heating and cooling condition that the Vickers hardness of the simulated HAZ falls within the range of the Vickers hardness of the HAZ in the butt welded joints. The Vickers hardness of the simulated HAZ sample is 329 HV0.3. The servo-hydraulic actuator conducted the incremental step tests at room temperature under axial strain control. Fig. 4.13 shows the one block of the strain history in the incremental step test with the strain ratio of $R_\varepsilon = -1$. The triangular waveform with a strain rate of 10^{-3} sec^{-1} was applied. The applied strain range was from 2000 to 30000 μm/m. This block was repeatedly applied to the tested specimen until specimen failure. The cyclic stress-strain curves were determined from the hysteresis loop of the block at half-life as a cyclically stabilized yield property, because stabilized values of stress and strain at the tips of the hysteresis loop in the vicinity of the half-life are usually observed [95-99]. Fig. 4.14 shows the cyclic stress-strain curves of the parent material, the simulated HAZ, and the weld metal. The cyclic stress-strain curves, as the mechanical property, were inputted to the nonlinear structure analysis, which applied the kinematic hardening law. The Poisson's ratio of all materials had a value of 0.3.

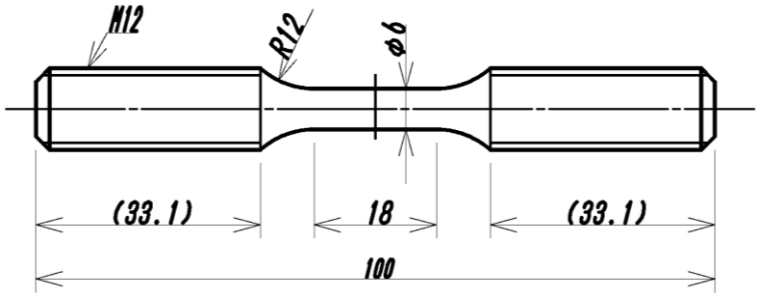

Fig. 4.10. Geometry of the specimen for the incremental step test.

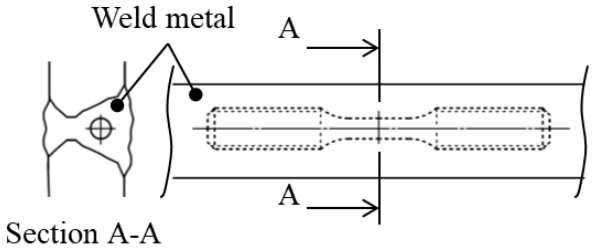

Fig. 4.11. Schematic drawing of specimen sampling for the weld metal.

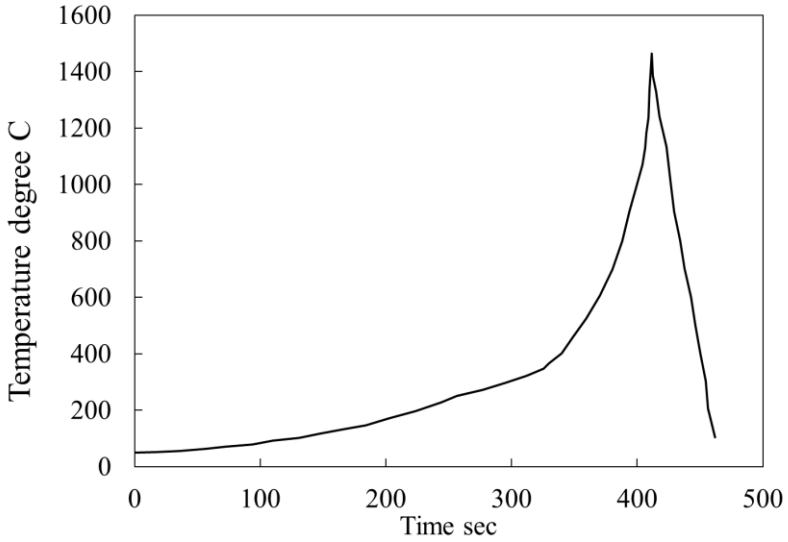

Fig. 4.12. Thermal history for the simulated HAZ sample.

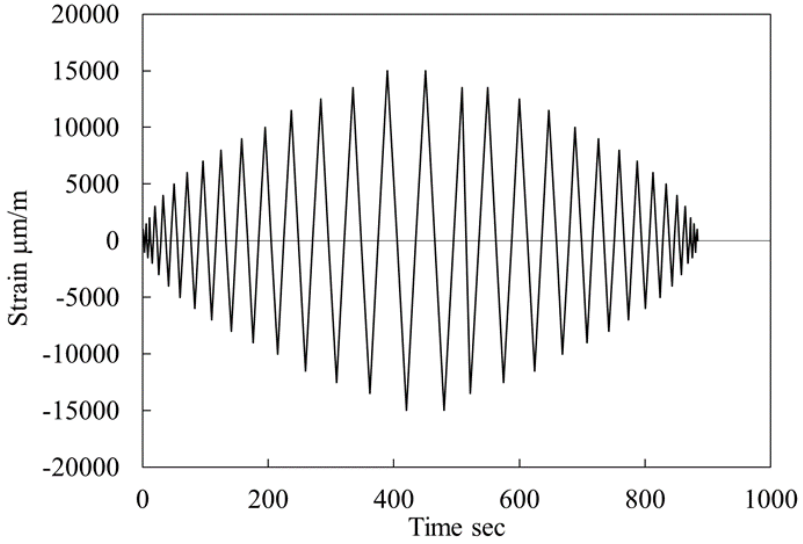

Fig. 4.13. Strain history of cyclic stress-strain test (one block).

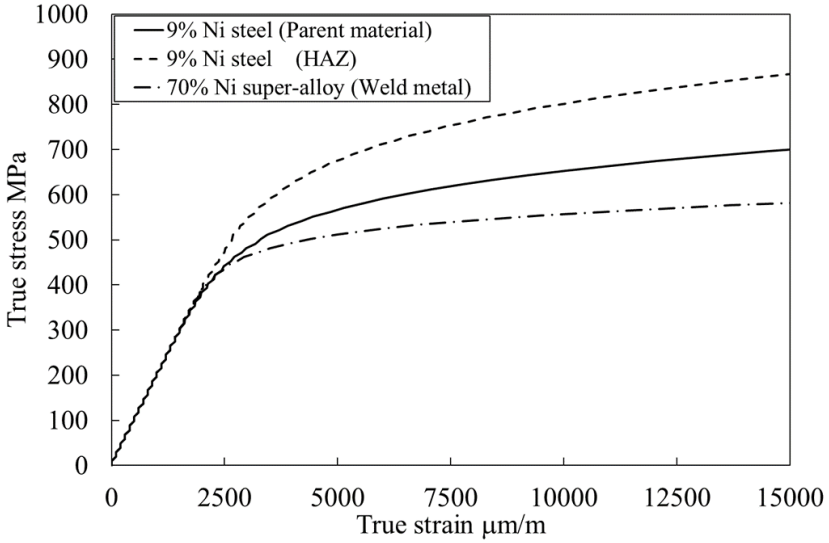

Fig. 4.14. Cyclic stress-strain curves.

4.3.3 Assessment method of crack initiation life

A strain-crack initiation life curve could characterize the fatigue crack initiation life of metals. These curves are obtained by the strain-controlled fatigue test using laboratory specimens. In this study, the fatigue crack initiation life N_c is defined as the number of cycles until the surface fatigue crack width reaches 0.5–1.0 mm. Fig. 4.15 shows the relationship between the total strain amplitude $\Delta\varepsilon_t/2$ and the crack initiation life N_c for 9% Ni steel, mild steel, high tensile steel, and aluminum alloy in the strain ratio of R_ε = -1 [91, 100-105]. The

surface crack width was measured using microscope. Table 4.5 lists the yield stress or the 0.2% proof stress, and the tensile strength of these materials. The strain-crack initiation life curve indicates a small scattering, regardless of the material type and static strength. The unified strain-crack initiation life curve in the strain ratio of $R_\varepsilon = -1$ was proposed, which is described as:

$$\frac{\Delta\varepsilon_t}{2} = 0.35{N_c}^{-0.6} + 0.005{N_c}^{-0.12} \qquad (4.3)$$

Equation (4.3) is based on the Coffin-Manson law [106, 107] and Basquin's equation [108] which can be used to describe the fatigue life. The constants were calculated by the least squares fitting for fatigue test data. The solid line in Fig. 4.15 indicates the proposed unified strain-crack initiation life curve in the strain ratio of $R_\varepsilon = -1$. We assume that the proposed unified strain-crack initiation life curve is valid for HAZ and weld metal of 9% Ni steel welded joints because the proposed unified strain-crack initiation life curve is almost unaffected by the material type and the static strength.

To consider the mean stress effect on the crack initiation life, the SWT approach was employed, described as:

$$SWT = \sigma_{\max}\frac{\Delta\varepsilon_t}{2} = f(N_c) \qquad (4.4)$$

where *SWT* is the SWT parameter, and $\sigma_{\max}$ is the maximum stress that consists of the residual

stress and the stress from the maximum external force. In this study, the direction of maximum stress σ_{max} at weld is a direction parallel to the surface of the specimen. The SWT approach assumes that the SWT parameter at given each fatigue life remains constant for different combinations of the total strain amplitude $\Delta\varepsilon/2$ and the maximum stress σ_{max}. When the strain and the stress distribution for a welded joint under cyclic fatigue loading are given, the fatigue crack initiation life of the welded joint can be calculated using Eqs. (4.3) and (4.4). We note that the fatigue crack initiation life N_c in this study was the number of cycles until the surface fatigue crack width reaches 0.5−1.0 mm.

Table 4.5 Static strength of materials used in the strain-crack initiation life curve.

Reference	Material name	yield stress or 0.2% proof stress MPa	Tensile strength MPa
[100]	9% Ni steel A	676	730
[100]	9% Ni steel B	600	770
[100]	9% Ni steel C	598	698
[100]	9% Ni steel D	722	754
[100]	9% Ni steel E	678	740
[91]	9% Ni steel	692	749
[91]	SM41B	274	451
[91]	HW50	568	647
[91]	HW70	794	843
[101]	HW45	510	627
[101]	Mild steel 1	323	Unknown
[102]	Mild steel 2	278	446
[102]	Mild steel 3	323	461
[102]	HT60	572	663
[103]	SM41A	Unknown	Unknown
[103]	HT60 NORM.	Unknown	Unknown
[103]	N-TUF33 Q.T.	Unknown	Unknown
[104]	5083-O	155	323

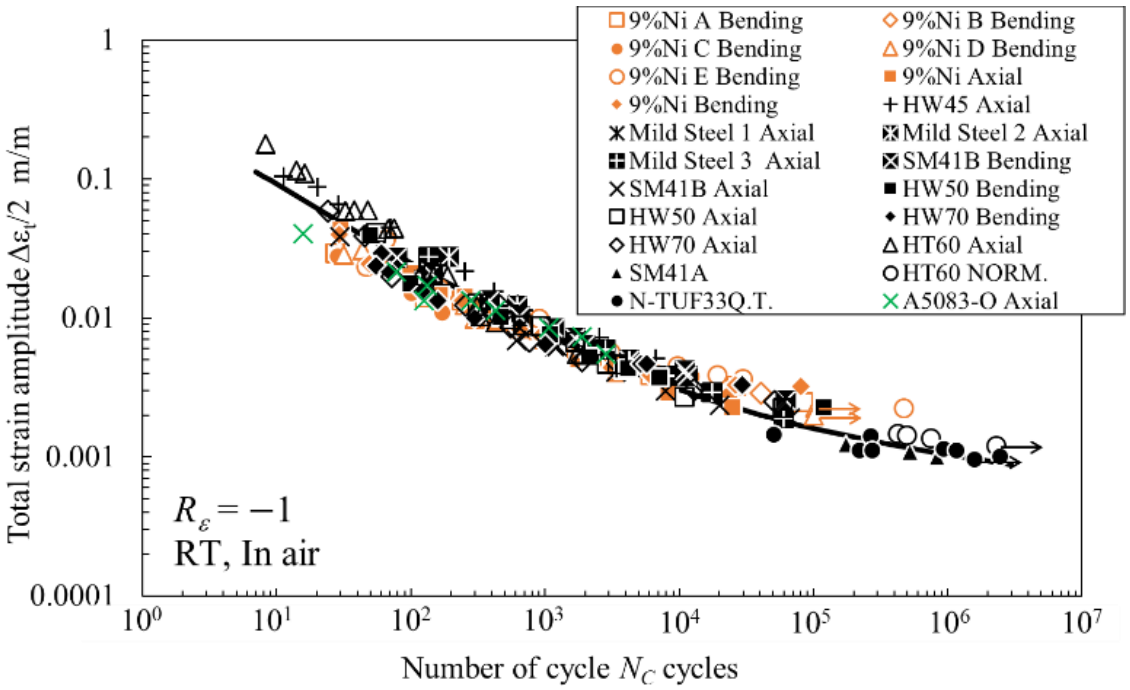

Fig. 4.15. Relationship between the total strain amplitude and the crack initiation life.

4.3.4 Assessment method of crack propagation life

After assessing the crack initiation life, the fatigue crack propagation life was estimated using linear fracture elastic mechanics. The fatigue crack propagation rate is described as a power model as the well-known Paris-Erdogan law [105]. Fig. 16 shows the comparison of the fatigue crack propagation property between 9% Ni steel, the HAZ, and weld metal (high nickel filler) [109–112]. The fatigue crack propagation properties of the HAZ and the weld metal indicate almost the same level as that of the 9% Ni steel. Thus, we assumed that the fatigue crack propagation properties of 9% Ni steel, the HAZ, and the weld metal are identical. The fatigue crack propagation property that considers the threshold stress intensity factor is described as:

$$\frac{da}{dN} = C_c(\Delta K^{m_c} - \Delta {K_{th}}^{m_c}) \qquad (4.5)$$

where a is the crack length, ΔK is the stress intensity factor range, ΔK_{th} is the threshold stress intensity factor, and C_c and m_c are constants. Elber [86] introduced the crack closure and opening concepts, and suggested that the crack closure and opening effects could be characterized by using the effective stress intensity factor range, ΔK_{eff}, defined as:

$$\Delta K_{eff} = K_{\max} - K_{\mathrm{op}} \qquad (4.6)$$

where $K_{\max}$ is the maximum stress intensity factor and K_{op} is the crack opening stress intensity factor. The relationship between the effective stress intensity factor range ΔK_{eff} and the applied stress intensity factor range ΔK is presented by:

$$\Delta K_{eff} = U\Delta K \qquad (4.7)$$

where U is the crack opening ratio. According to Elber approach, the fatigue crack propagation property is described as [113]:

$$\frac{da}{dN} = C_c\left(\Delta K_{eff}{}^{m_c} - \Delta K_{eff,th}{}^{m_c}\right) \qquad (4.8)$$

Much research reported on the crack opening ratio U [27, 54–58]. Elber [86] indicated that the crack opening ratio U is represented by a linear equation of the stress ratio R. Schijve [115] proposed an improved equation for the crack opening ratio U, which is a quadratic equation of

the stress ratio. Furthermore, not only the stress ratio but also the stress intensity factor range affect the crack opening ratio U [115, 117–118]. In this study, to consider the effects of both the stress ratio and the stress intensity factor, the crack opening ratio U was applied using the following equations [117]:

$$U = \min\left\{\frac{1}{R_0 - R} - \frac{K_0}{\Delta K}, 1\right\} \qquad (4.9)$$

$$\Delta K_{th}(R) = \max\left\{\left(\Delta K_{eff,th} + K_0\right) \cdot (R_0 - R), \Delta K_{eff,th}\right\} \qquad (4.10)$$

$$\frac{da}{dN}(R) = C_c((U\Delta K)^{m_c} - \Delta K_{th}(R)^{m_c}) \qquad (4.11)$$

where R_0 and K_0 are the constants. To obtain the values of R_0 and K_0 for 9% Ni steel, we performed accumulation of the experimental data [109, 119-120] of the fatigue crack propagation. Figure 4.17 shows the relationship between the threshold stress intensity factor and stress ratio for 9% Ni steel. From the relationship between the threshold stress intensity factor and stress ratio, we obtained the values of R_0, K_0 and $\Delta K_{eff,th}$ for 9% Ni steel. These values were substituted into Eqs. (4.9), (4.10) to obtained Eqs. (4.12) and (4.13).

$$U = \min\left\{\frac{1}{1.29 - R} - \frac{1}{\Delta K}, 1\right\} \qquad (4.12)$$

$$\Delta K_{th}(R) = \max\{(3.81 + 1) \cdot (1.29 - R), 3.81\} \qquad (4.13)$$

The solid line in Fig. 4.17 indicates Eq. (4.13).

Fig. 4.18 shows the relationship between the crack propagation rate and the stress

intensity factor range for 9% Ni steel, indicating the effect of the stress ratio [109]. Fig. 4.19 shows the relationship between the crack propagation rate and the effective stress intensity factor range by using the values of R_0, K_0 and $\Delta K_{eff,th}$ for 9% Ni steel in the linear relation region on a double logarithm. The relationship between the crack propagation rate and the effective stress intensity factor range indicates a small scattering, regardless of the stress ratio. From the relationship between the crack propagation rate and the effective stress intensity factor range, we obtained the values of C_c and m_c for 9% Ni steel. These values were substituted into Eq. (4.11), we obtained Eq. (4.14).

$$\frac{da}{dN}(R) = 2.1 \times 10^{-12}((U\Delta K)^{3.5} - \Delta K_{th}(R)^{3.5}) \qquad (4.14)$$

To consider the effect of residual stress, the stress ratio for welded joints on fatigue crack propagation is described as:

$$R_K = K_{\min}/K_{\max} \qquad (4.15)$$

where R_K represents the crack tip stress ratio, $K_{\min}$ is the minimum stress intensity factor, and $K_{\max}$ is the maximum stress intensity factor. $K_{\min}$ and $K_{\max}$ for welded joints are calculated by the stress from the external force and the residual stress. The fatigue crack propagation properties of 9% Ni steel welded joints were described as:

$$U_K = \min\left\{\frac{1}{1.29 - R_K} - \frac{1}{\Delta K}, 1\right\} \qquad (4.16)$$

$$\Delta K_{th}(R_K) = \max\{(3.81 + 1) \cdot (1.29 - R_K), 3.81\} \qquad (4.17)$$

$$\frac{da}{dN}(R_K) = 2.1 \times 10^{-12}((U_K \Delta K)^{3.5} - \Delta K_{th}(R_K)^{3.5}) \qquad (4.18)$$

where U_K represents the crack opening ratio based on the crack tip stress ratio.

The initial single fatigue crack width was employed at 1.0 mm, as explained in section 4.3.3. It is necessary to determine the initial fatigue crack depth in order to conduct the fatigue crack propagation analysis. This study assumes the initial fatigue crack depth as 0.25 mm from the relationship between the crack width and the crack depth for welded joints, as shown in Fig. 4.20 [63–65]. Because the initiation of multiple fatigue cracks occurs along the length of the weld toe and are merged, an initial edge crack at a depth of 0.25 mm was applied to the calculation model for the stress intensity factor. Fig. 4.21 shows the calculation model of the stress intensity factor for an edge crack in a plate subjected to nonlinear stress distribution that is obtained from the structural analysis. The stress intensity factor for this model is described as [121]:

$$K = \frac{1}{\sqrt{2\pi c}} \int_0^c \sigma(u) \sum_{i=1}^{5} F_i \left(1 - \frac{u}{c}\right)^{i-\frac{3}{2}} du \qquad (4.19)$$

Crack geometry dimensional limit: $0 < c/t \leq 0.9$

where u is the distance from the crack initiation point along a parallel direction of the crack, $\sigma(u)$ is the stress distribution, and F_i is the coefficients which related with the crack depth c and

the plate thickness t (Appendix 4). For the fracture of the specimen, we assumed the number of cycle which the maximum value of the stress intensity factor K_{max} reaches the fracture toughness of value of 160 MPa$\sqrt{m}$ [66].

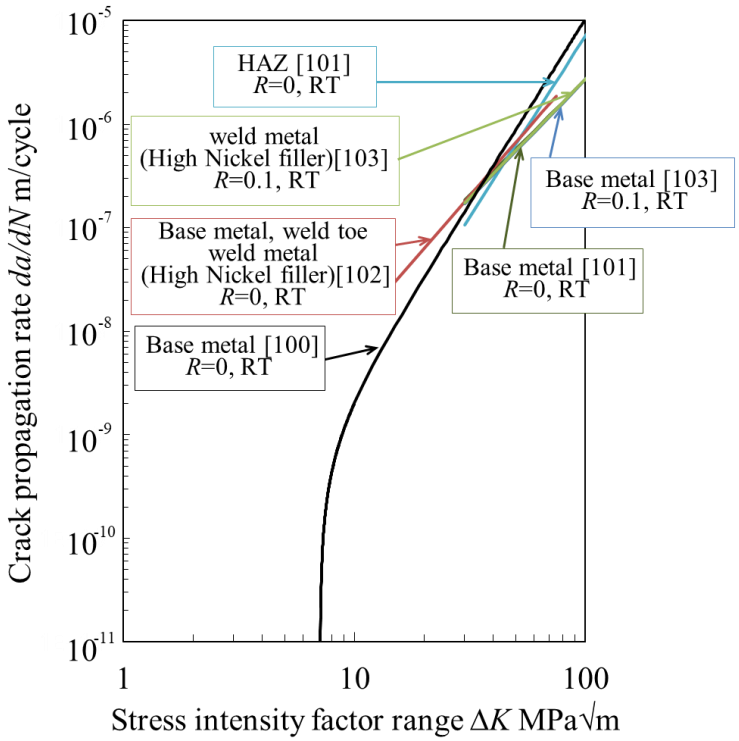

Fig. 4.16. Fatigue crack property comparison between parent material, HAZ and weld metal.

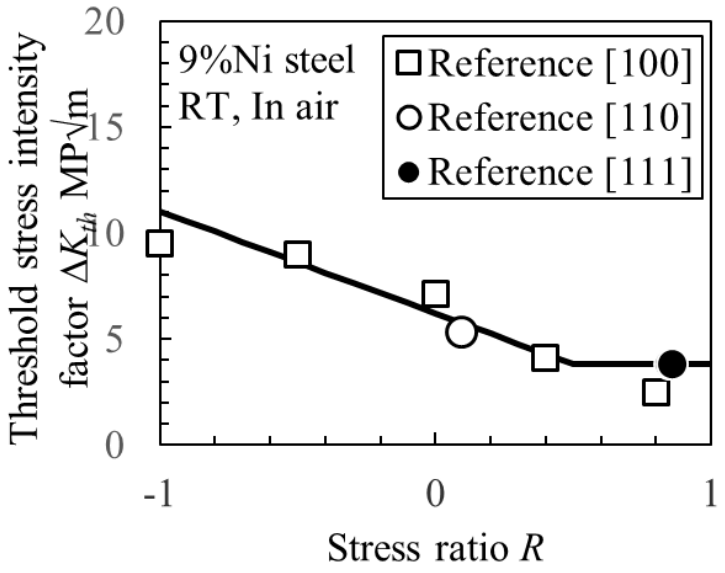

Fig. 4.17. Effect of the stress ratio on the threshold stress intensity factor

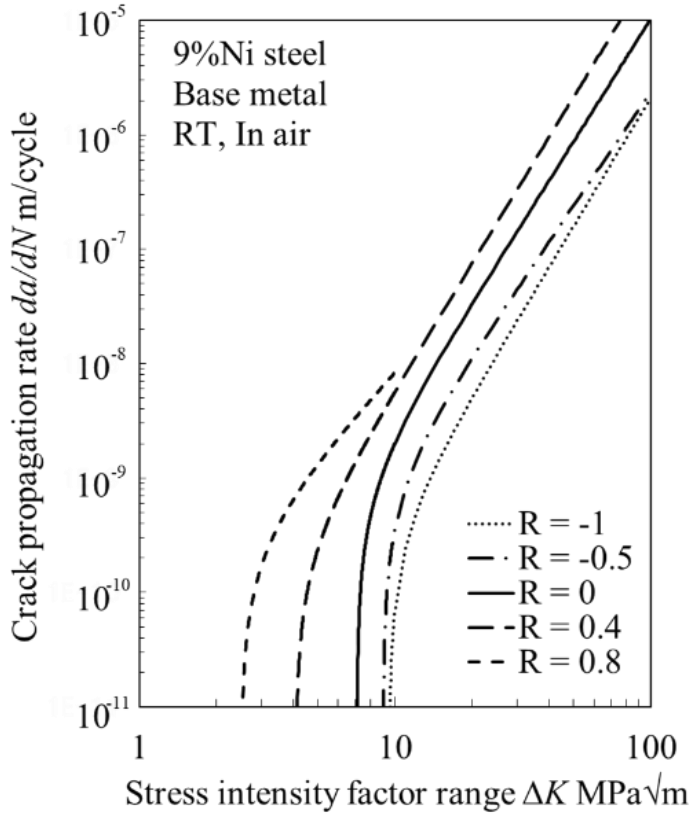

Fig. 4.18. Relationship between crack propagation rate and stress intensity factor range for 9% Ni steel [109].

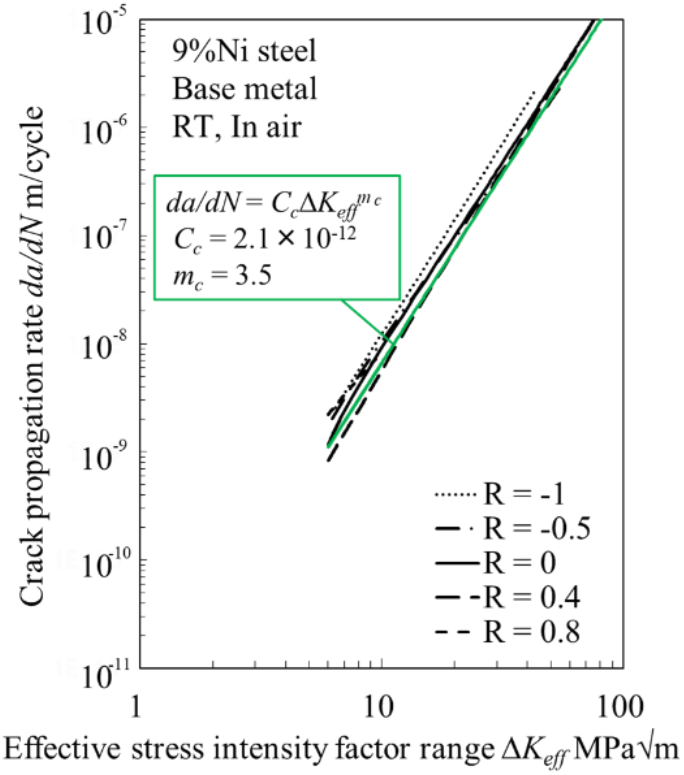

Fig. 4.19. Relationship between crack propagation rate and effective stress intensity factor range for 9% Ni steel.

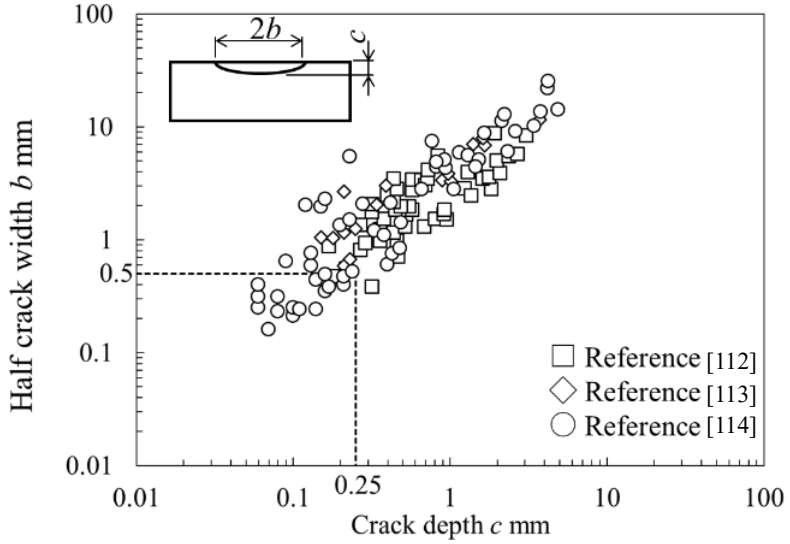

Fig. 4.20. Relationship crack width and crack depth for welded joints.

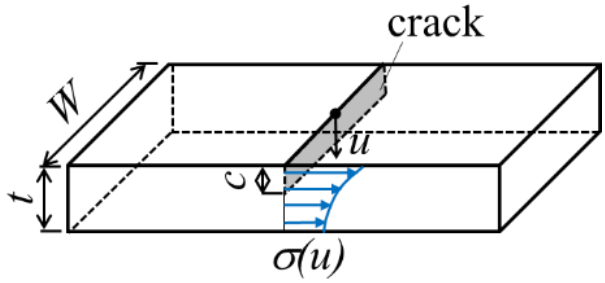

Fig. 4.21. Schematic diagram of calculation model of stress intensity factor.

4.4 Finite element analysis results

Fig. 22 shows the longitudinal welding residual stress distributions that were obtained from the welding simulation. The high tensile stress around the weld toe was observed. On the other hand, the compressive stress around the middle of plate thickness near the welding area, which is balance against the high tensile stress around the weld toe, was observed. These tendencies are slightly strong for the type M welded joint because of the difference between the welding pass sequence and the welding conditions of type S and that of type M.

After applying the first fatigue loading cycle in the range of this investigation, the stress-strain response under cyclic fatigue loading indicates the elastic shakedown. Fig. 4.23 shows the cyclic stress-strain response at the maximum SWT parameter point as a representative response. The maximum SWT parameter point is critical for fatigue crack initiation. The first cycle stress-strain response indicated a nonlinearity because of plastic deformation. The second cycle stress-strain response indicated complete linearity. These results imply that the welded joint specimens under cyclic fatigue loading, excluding the first loading, could be applied to the linear fracture elastic mechanics to estimate the fatigue crack propagation life. Figure 4.24 shows the longitudinal stress distribution $\sigma_x(y)$ from the weld toe under fatigue loading after the first loading cycle. These longitudinal stress distribution $\sigma_x(y)$

were used to calculate the stress intensity factor to estimate the fatigue crack propagation life.

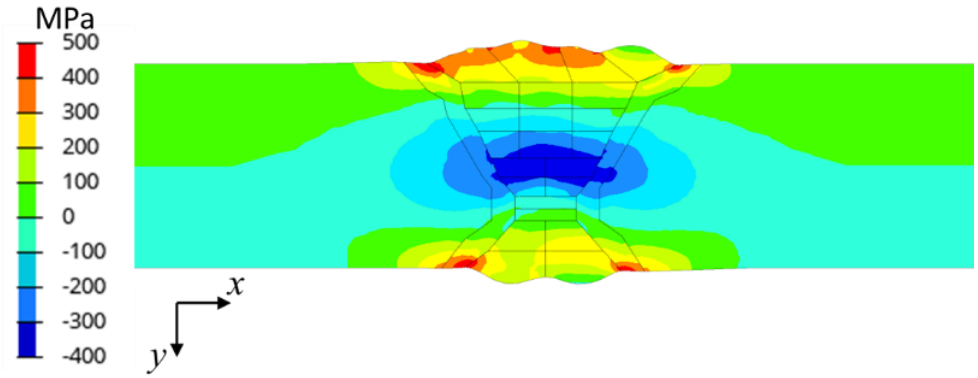

(a) Type S

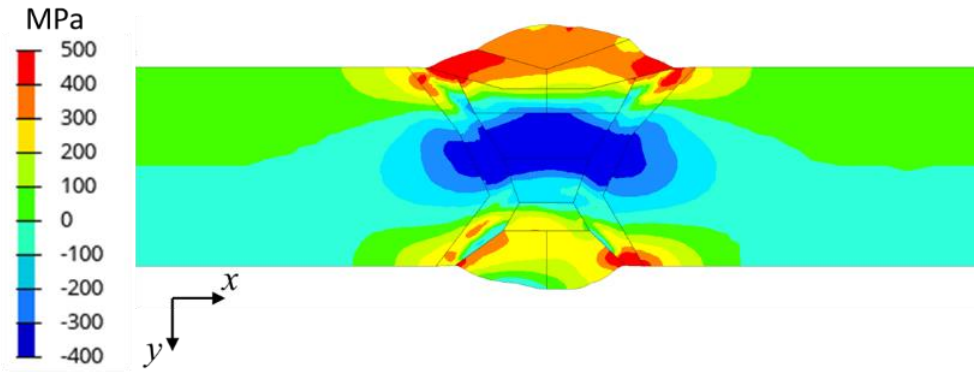

(b) Type M

Fig. 4.22. Contour of longitudinal welding residual stress.

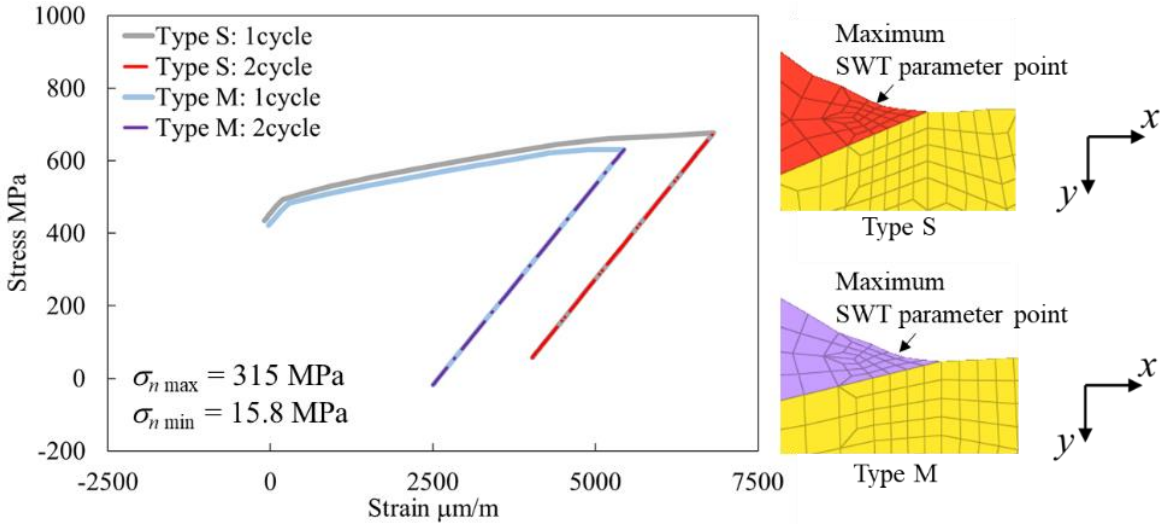

Fig. 4.23. Cyclic stress-strain response at maximum SWT parameter point.

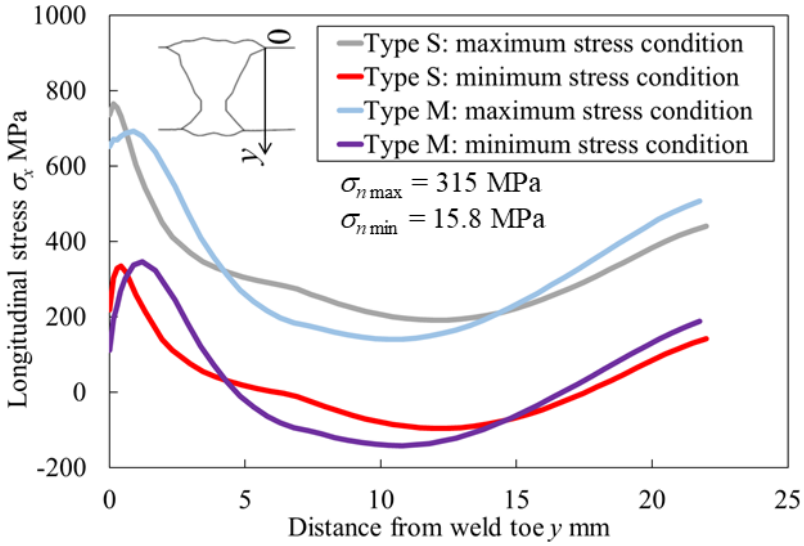

Fig. 4.24. Longitudinal stress distribution under fatigue loading.

4.5 Fatigue life prediction result

The critical area for the fatigue crack initiation was found by the stress-strain field that is obtained by the structural analysis. In the proposed fatigue life prediction method, the fatigue crack initiation point is determined as the maximum SWT parameter point. The maximum SWT point were the weld toe, as shown in Fig. 4.23. Fig. 4.25 shows the results of the fatigue life prediction, namely total fatigue life to failure N_f and the fatigue crack initiation life N_c. The predicted fatigue crack initiation life N_c of type S and that of type M were almost the same. Thus, it was surmised that the influence of the difference between the welding pass sequence and the welding conditions of type S and that of type M is small on the fatigue crack initiation life N_c. Similarly, the predicted total fatigue life to failure N_f of type S and that of type M were almost same up to about the 2×10^6 cycle. However, the predicted total fatigue life to failure N_f of type S indicates to be slightly longer than that of type M from more than about 2×10^6 cycle. The slopes of the predicted S-N curves change at the 2×10^6 cycle because of the effect of the threshold stress intensity factor on the fatigue crack propagation.

Fig. 4.26 shows the predicted crack propagation rate at the initial fatigue crack depth. The predicted crack propagation rates at the initial fatigue crack depth sharply dropped from less than about $\Delta\sigma$ = 110 MPa because of the effect of the threshold stress intensity factor. This tendency, which is more remarkable for type S, influences the predicted fatigue crack propagation life and slope of the predicted S-N curves.

To confirm the accuracy of the proposed method, the prediction results of the total fatigue life to failure N_f are compare with the experimental results. As shown in Fig. 4.25, the fatigue life prediction method achieved a result closer to the fatigue test results of type S and type M.

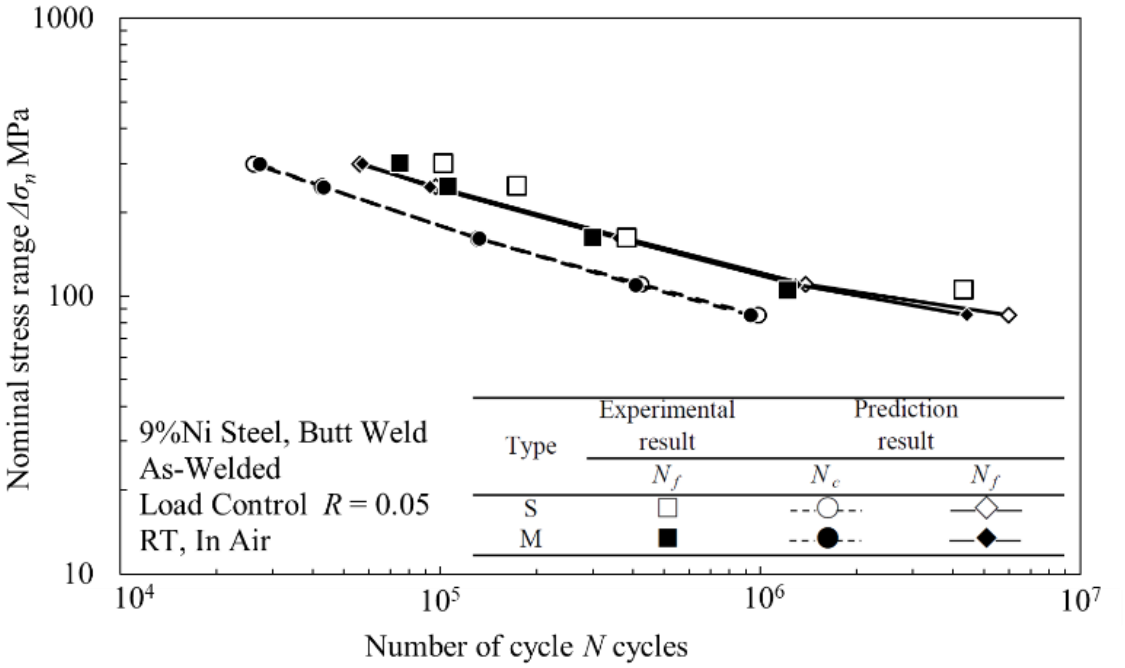

Fig. 4.25. Predicted S-N curve.

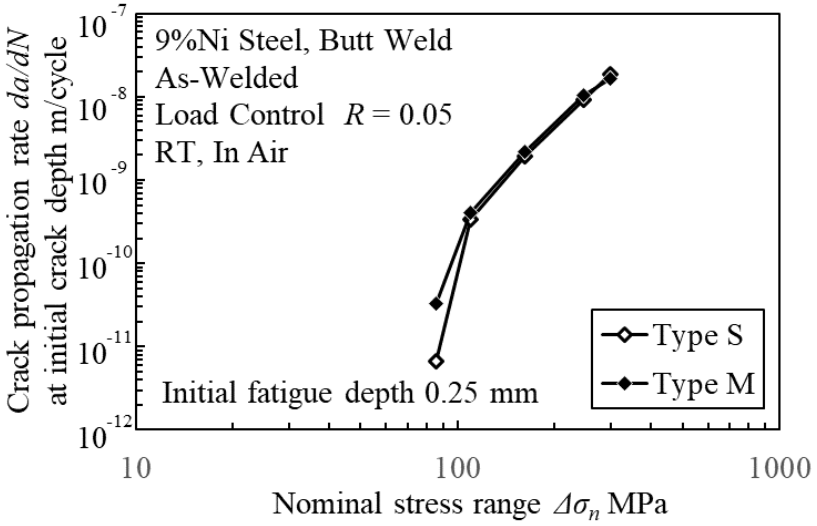

Fig. 4.26. Predicted crack propagation rate at initial fatigue crack depth.

4.6 Discussion

As mention above, the prediction results using the proposed fatigue life prediction method for the welded joints indicates is in good agreement with the fatigue tests results of 9% Ni steel butt welded joints. However, it is necessary that the validity of the estimation of the crack initiation life and the crack propagation life are tested. To test the validity of the estimation of the crack initiation life and the crack propagation life, the additional fatigue test was conducted. The welded joint type of the additional fatigue test was type M, and the test condition was the same as in section 4.2. The applied constant nominal stress range $\Delta\sigma_n$ was 110 MPa. The fatigue life was evaluated by using beach marks of the fracture surface, as shown in Fig. 4.27. Multiple fatigue cracks occurred and merged, and then grew to an edge crack. These behaviors were the same as the assumption on the calculation of the stress intensity factor in section 4.3.4. The crack depth at the 3.9×10^5 cycle, obtained by the additional fatigue test, was about 0.4 mm. These results were almost the same as the fatigue crack initiation prediction results. The proposed method assumed the initial fatigue crack depth at 0.25 mm, and predicted

the fatigue crack initiation life at the 4.1×10^5 cycle. Fig. 4.28 shows the comparison of the fatigue crack propagation rate between the prediction results and the experimental data at the center of the specimen width. The prediction results of the crack propagation rate correspond well with the experimental results.

It is possibility that the proposed fatigue life prediction method can be applied to other welded joint type and other materials, but further experimental and analytical work are necessary to test the validity of the proposed method.

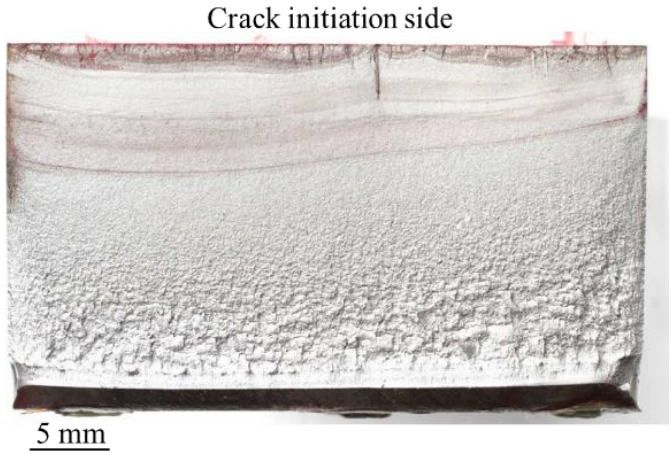

Fig. 4.27. Photo of fracture surface.

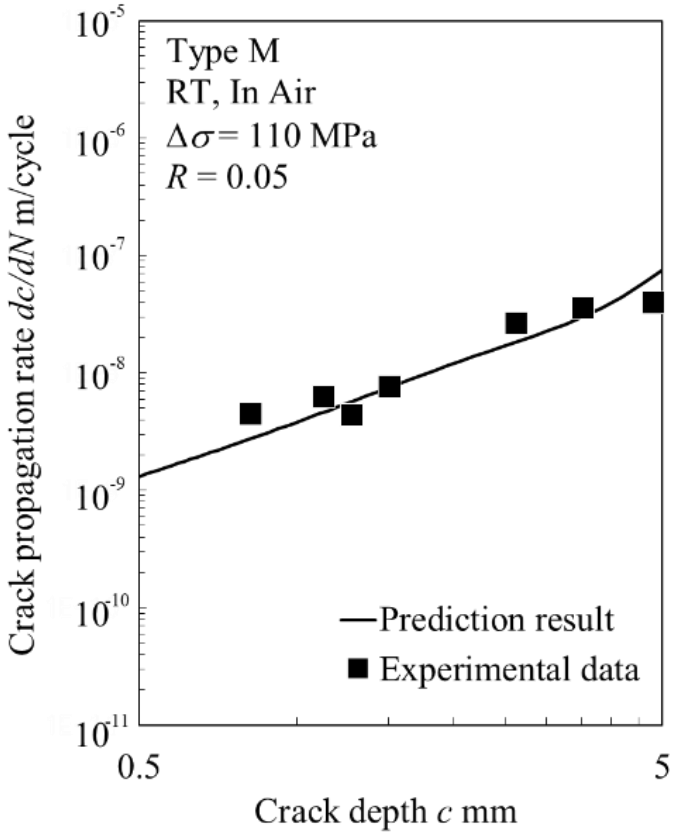

Fig. 4.28. Comparison of fatigue crack propagation rate between prediction result and experimental data.

4.7 Conclusions

This paper proposed the fatigue life prediction method of welded joints, which is considered the geometric effect, the difference of cyclic stress-strain properties between parent material, the HAZ, and weld metal, and the mean stress effect by welding residual stress and applied stress. We evaluated the validity of the proposed method by comparing it with the fatigue test results of 9% Ni steel butt welded joints. The results can be summarized as follow:

- This study combined the finite element analyses, which are the welding simulation and the nonlinear structural analysis applied fatigue loading, and the estimation method of the

fatigue crack initiation and fatigue crack propagation to predict the fatigue life of welded joints. The FEA models were made from the real surface geometry of the welded joints to consider the geometric effects.

- The study proposed the unified strain-crack initiation life curve, regardless of the material type and the static strength. In the fatigue crack initiation life of welded joints, the proposed strain-crack initiation life curve was combined with the mean stress correction approach.
- The fatigue crack propagation properties of 9% Ni steel, which could consider the mean stress effect, were summarized.
- The proposed fatigue life prediction method for welded joints can successfully predict the fatigue life of 9% Ni steel butt welded joints. The proposed method has possibility that can be applied to other welded joint type and other materials. However, further experimental and analytical works are necessary to test the validity of the proposed method.

Chapter 5 Fatigue life prediction for 9 % Ni steel cruciform welded joints based on local stress-strain behavior and crack propagation

5.1 Introduction

9 % Ni steel is candidate material for tanks of liquefied natural gas (LNG) carrier and LNG fuel ship, since 9 % Ni steel have superior fracture toughness at cryogenic temperatures [81, 82]. International Maritime Organization (IMO) requires fatigue analysis for type B independent tank [1, 2]. The American Bureau of Shipping (ABS) gives design S-N curves for 9 % Ni steel fillet welded joints and the thickness effect correction factor *g* (*t*) [1]. The thickness effect correction factor *g* (*t*) is given as:

$$g(t) = \left(\frac{t}{t_{ref}}\right)^{n} \qquad (5.1)$$

$$t_{ref} = 22 \text{ mm}$$

$$n = 0.25$$

where *t* is main plate thickness, t_{ref} is reference plate thickness, and *n* is the thickness correction exponent. When main plate thickness is greater than 22 mm, stress range is to be adjusted by the thickness effect correction factor *g* (*t*). The Lloyd's Register [4, 122] gives the same thickness effect correction factor for cruciform joints as that of the ABS guide.

Whereas, very few studies have been reported on fatigue strength for 9 % Ni steel cruciform welded joints. Only Gioielli et al. [18, 19] have presented fatigue test results for non-load-carrying cruciform joints of 9% Ni steel. Main plate thickness of specimens on these study

are 10 mm and 20 mm. Little is known about the geometric effect, including bead profile, on fatigue strength of 9 % Ni steel cruciform welded joints. Furthermore, to conduct assessment of fatigue life for 9 % Ni steel cruciform welded joints with high accuracy, it is important to consider the mean stress effect by welding residual stress and applied stress, and difference of cyclic stress-strain properties between parent material, heat affected zone (HAZ), and weld metal. However, these effects on fatigue strength for 9 % Ni cruciform welded joints are not apparent in the published study.

The purpose of this study was to reveal fatigue behavior and fatigue life for 9 % Ni steel cruciform welded joints. We first conducted fatigue tests for non-load-carrying cruciform welded joints of 9% Ni steel, the main plate of which are 10 mm, 16 mm and 22mm, at room temperature. Then, we performed finite element (FE) analyses to calculate welding residual stress field and stress-strain response under fatigue loading. The FE models were based on the real geometry of the welded joints. The results of FE analyses, which consist of welding simulation and the nonlinear structure analysis under fatigue loading, clarified stress-strain field of 9 % Ni steel cruciform welded joints under fatigue loading. Fatigue crack initiation life and fatigue crack propagation life for 9 % Ni steel cruciform welded joints was predicted using proposed fatigue life prediction method of welded joints in chapter 4. The fatigue life prediction results were good agreement with the fatigue test results, regardless of main plate thickness and bead profile of cruciform welded joints.

5.2 Fatigue test of welded joints

We conducted fatigue tests for non-load-carrying cruciform joints of 9% Ni steel. The main plate thickness of specimens are 10 mm, 16 mm and 22 mm.

5.2.1 Material and specimen

The parent material is 9% Ni steel, and the weld metal is 70% Ni super-alloy, which are same as that of specimens in chapter 4. Table 5.1 lists the chemical composition of the parent material and the weld metal. Table 5.2 lists the mechanical properties of the parent material and the weld metal. Figure 5.1 shows the geometry and the dimensions of the fatigue test specimen. Figure 5.2 shows the photo of the typical welding cross section. Detail of the bead profile are described in section 5.3.2. The reference value of weld leg length is 5 mm, regardless main plate thickness. Figure 5.3 shows welding sequence. Table 5.3 lists welding conditions. Figure 5.4 shows Vickers hardness distribution of welded joints. There is almost no difference between Vickers hardness distributions of three kinds of specimens. A range of Vickers hardness of HAZ is 320 to 366.

Table 5.1 Chemical composition of parent material and weld metal (%).

(a) 9% Ni steel (parent material).

C	Si	Mn	P	S	Ni
0.05	0.22	0.64	0.003	0.0006	8.96

(b) 70% Ni super-alloy (weld metal).

C	Si	Mn	P	S	Ni
0.08	0.28	2.3	0.003	0.002	67.1
Cu	Mo	Nb	Fe	W	Nb+Ta
13.6	3.9	1.5	10.0	0.7	1.5

Table 5.2 Mechanical properties of parent material and weld metal.

Material	0.2% proof stress MPa	Tensile strength MPa	Elongation at fracture %
9% Ni steel	681	719	30
70% Ni super-alloy	445	698	42

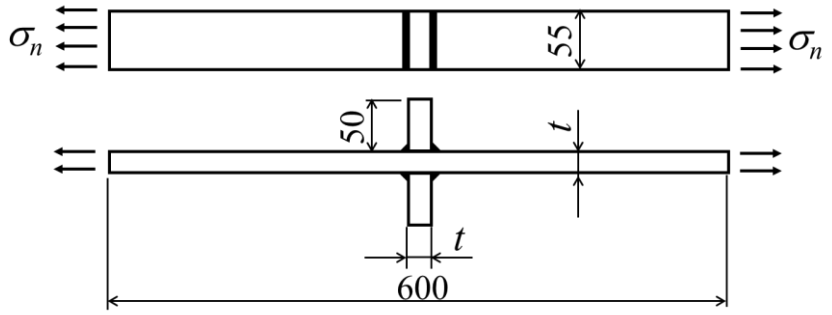

Fig. 5.1. Geometry of welded joint.

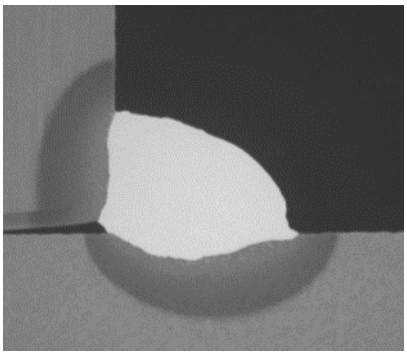

Fig. 5.2. Typical welding cross section (t = 10 mm).

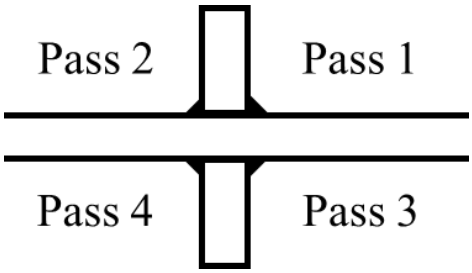

Fig. 5.3. Welding sequence.

Table 5.3 Welding conditions.

Main plate thickness t mm	Current A	Voltage V	Speed cm/min
10	134	24.8	15.4
16	131	24.6	14.6
22	138	23.0	16.2

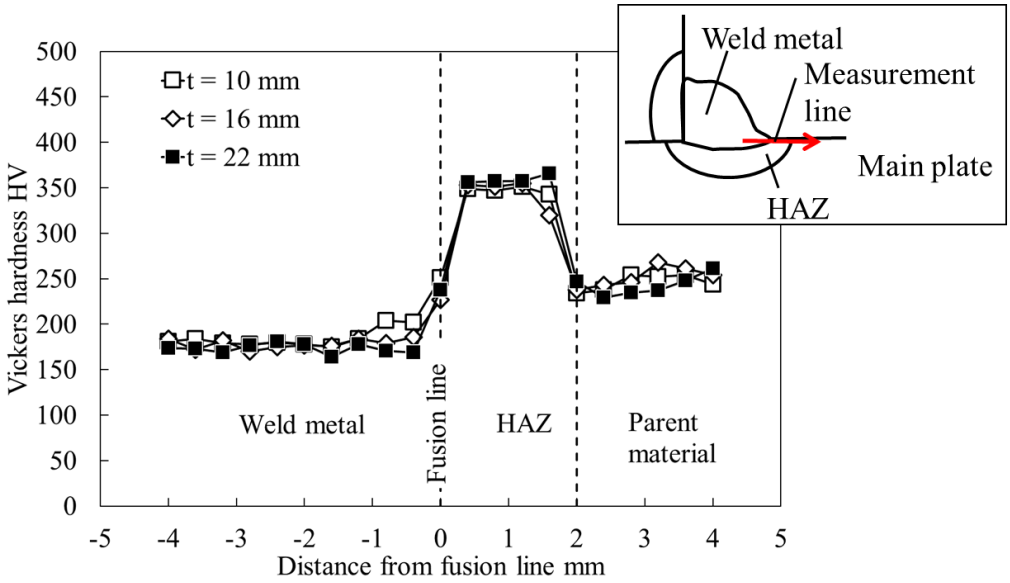

Fig. 5.4. Vickers hardness distribution around weld toe.

5.2.2 Test conditions

The constant amplitude fatigue tests at room temperature were conducted under load control by the servo hydraulic actuator. Axial fatigue load was applied to the specimens in a sinusoidal waveform with the frequency of 4-12 Hz and the stress ratio of $R = 0.5$. The applied constant nominal stress range $\Delta\sigma_n$ was in the range of 90 to 200 MPa.

5.2.3 Fatigue test results

For all the fractured specimens, the fatigue crack initiated at the weld toe, as shown Fig. 5.5. Figure 5.6 shows the fatigue test results. The mean S-N curve of these test results was calculated by least squares fitting for fatigue test data using Eq. (5.2) to yield the following:

$$\Delta\sigma_n{}^m \cdot N_f = C \qquad (5.2)$$

where N_f is the number of cycles to failure, and m and C are the constants. Table 5.4 lists constants of the mean S-N curve. The design S-N curve for non-load-carrying fillet welded joints of 9% Ni steel by the ABS [20], which is shown in Fig. 5.6, gives non-conservative assessment.

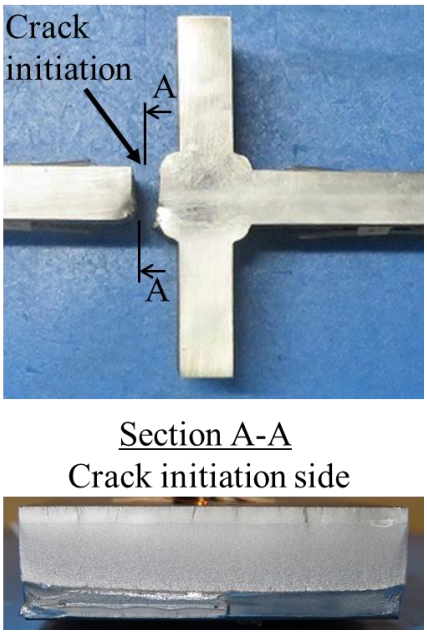

Fig. 5.5. Typical fatigue crack initiation point (t = 16 mm).

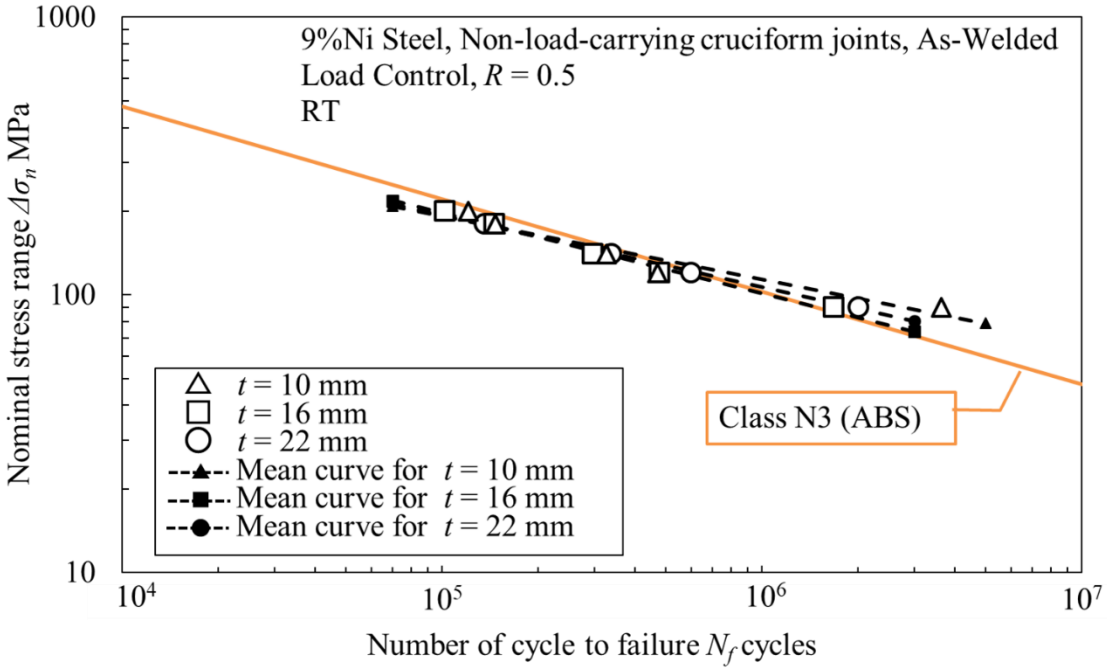

Fig. 5.5. Fatigue test results.

Table 5.4 S-N curve parameters.

	S-N curve parameters		Fatigue strength at 2×10^6 cycle MPa
	C	m	
Mean curve for t = 10 mm	1.08×10^{15}	4.39	97
Mean curve for t = 16 mm	8.62×10^{12}	3.46	83
Mean curve for t = 22 mm	7.53×10^{13}	3.88	89
Design curve: Class N3 (ABS)	1.07×10^{12}	3.00	81

5.3 Fatigue life prediction

The proposed fatigue life prediction method for welded joints in chapter 4 is employed to estimate fatigue life for the non-load-carrying cruciform welded joints of 9 % Ni steel. Detail of the proposed fatigue life prediction method is described in chapter 4.

5.3.1 Finite element analysis

The welding simulation and the nonlinear structure analysis under fatigue loading

were performed for the non-load-carrying cruciform welded joints of 9 % Ni steel using commercial FE code ABAQUS 2018. The analysis procedures and element types are same as that of chapter 4.

Figure 5.6 shows FE models of non-load-carrying cruciform welded joints. The two dimensional symmetric models were used. The FE models were made from the real weld surface geometry which were scanned using the laser scanner HP-L-20.8 on Absolute Arm 7530SE. The element size around the weld toe was about 0.1 mm. Double nodes are defined on the boundary between the main plate and the attached plate, as shown in Fig. 5.6. The boundary between the main plate and the attached plate are not consider contact in these analysis.

Since materials of the cruciform welded joints were same as that in chapter 4, material properties on welding simulation in chapter 4 were applied to welding simulations in this chapter. As shown Fig. 5.7, Vickers hardness of parent material, HAZ, and weld metal of the cruciform welded joints indicate almost same level of that of butt welded joints in chapter 4. Thus, cyclic stress- strain properties of the structure FE analysis for the cruciform welded joints were same as that in chapter 4. The Poisson's ratio of all materials was assumed the value of 0.3.

In the welding simulation, the initial temperature of specimen and ambient temperature for the thermal analysis were set to 20°C. The convective heat coefficient on all the surface was assumed the value of 10 W/m^2 K [90]. We assumed that the arc efficiency for welding is 70% [89].

In the nonlinear structure analysis under fatigue loading, the cyclic fatigue loading was applied using distribution load command, as shown in Fig. 5.1.

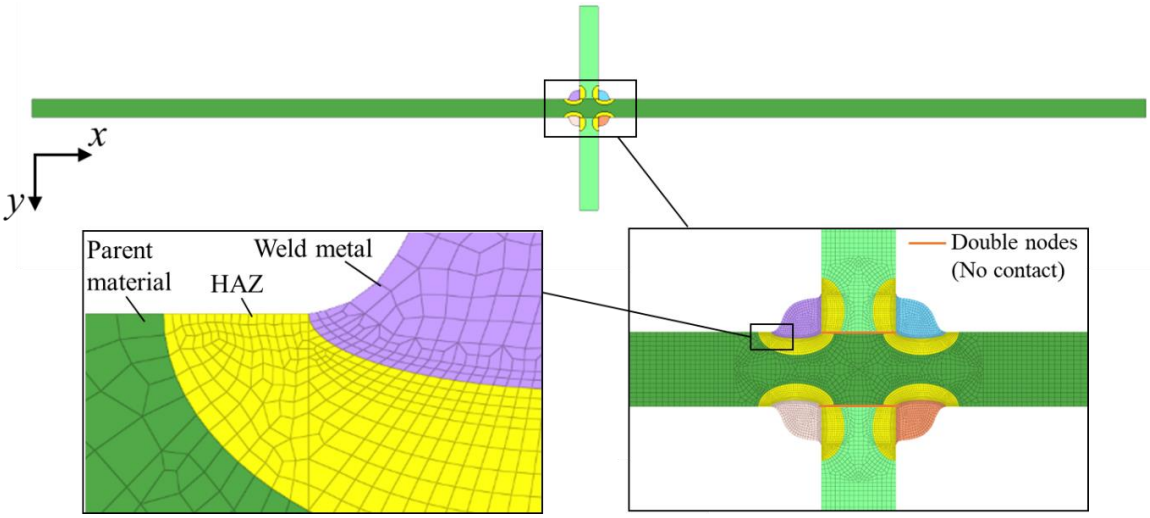

(a) t = 10 mm.

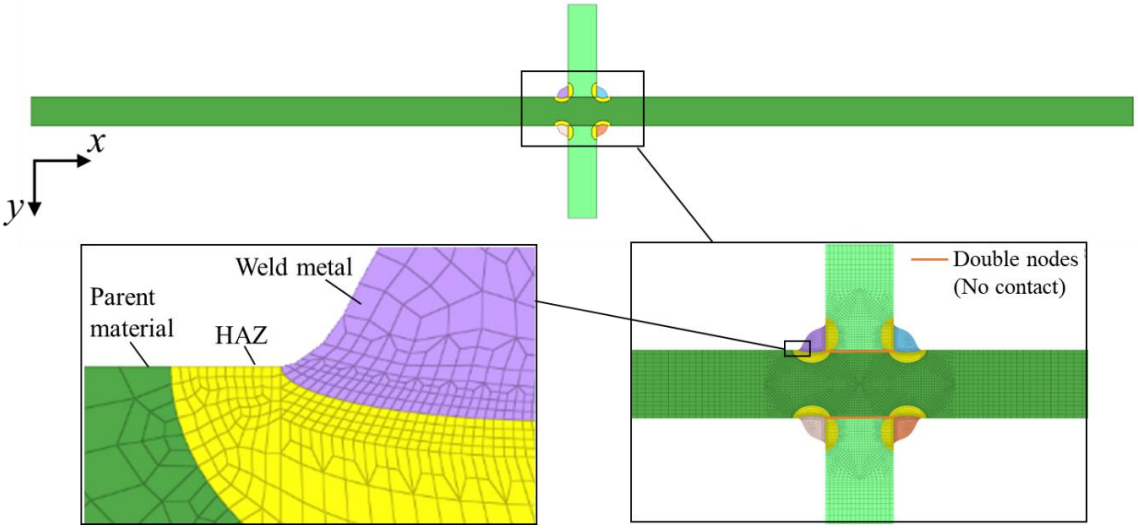

(b) t = 16 mm.

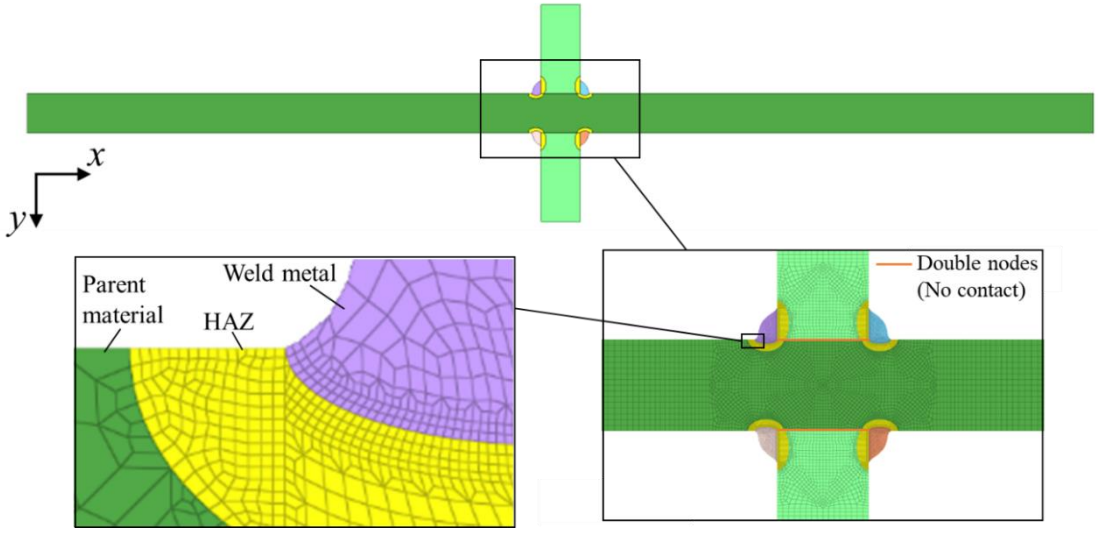

(c) t = 22 mm.

Fig. 5.6. Finite element model.

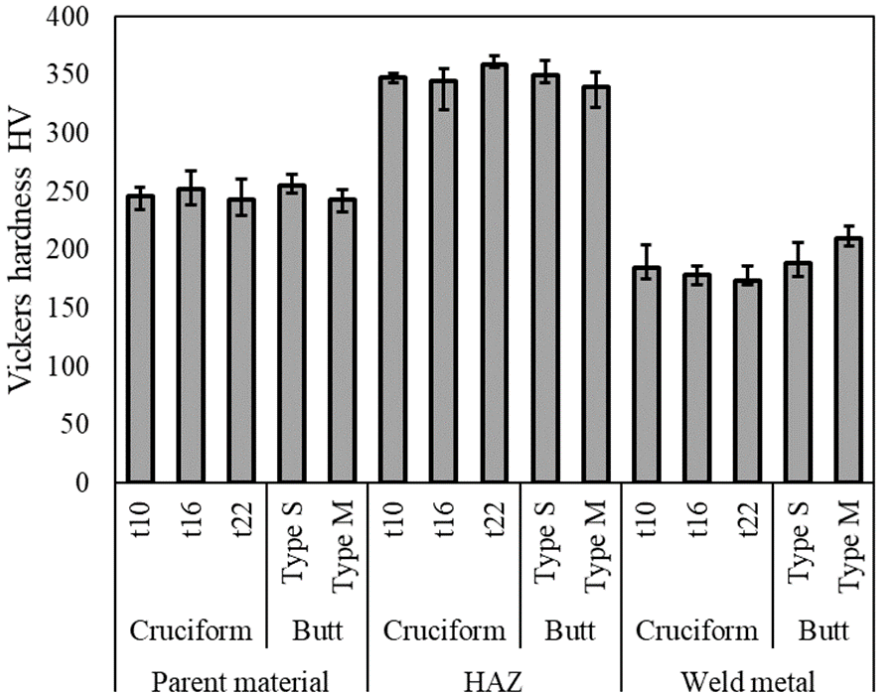

Fig. 5.7 Comparison of Vickers hardness between butt joints and cruciform joints.

5.3.2 Assessment method of crack initiation life and crack propagation life

The assessment method of crack initiation life and crack propagation life for welded joints are same as that in chapter 4.

The fatigue crack initiation life of metals can be characterized by a strain-crack initiation life curve in the strain ratio of R_ε = -1, which is describe as:

$$\frac{\Delta\varepsilon_t}{2} = 0.35{N_c}^{-0.6} + 0.005{N_c}^{-0.12} \qquad (5.3)$$

where $\Delta\varepsilon_t$ is the total strain range and N_c is the number of cycle to fatigue crack initiation life. In this study, the fatigue crack initiation life N_c is defined as the number of cycle until the surface fatigue crack width reaches 0.5-1.0 mm. To consider the mean stress effect on the crack

initiation life, the SWT approach [43] was employed. The SWT approach is described as follows:

$$SWT = \sigma_{\max}\frac{\Delta\varepsilon_t}{2} = f(N_c) \qquad (5.4)$$

where *SWT* is the SWT parameter, and $\sigma_{\max}$ is the maximum stress which consists of the residual stress and the stress by the external force.

After assessment of the crack initiation life, the fatigue crack propagation life was estimated using the linear fracture elastic mechanics. The fatigue crack propagation law for 9 % Ni steel is described as:

$$U_K = \min\left\{\frac{1}{1.29 - R_K} - \frac{1}{\Delta K}, 1\right\} \qquad (5.5)$$

$$\Delta K_{th}(R_K) = \max\{(3.81 + 1)\cdot(1.29 - R_K), 3.81\} \qquad (5.6)$$

$$\frac{da}{dN}(R_K) = 2.1 \times 10^{-12}((U_K\Delta K)^{3.5} - \Delta K_{th}(R_K)^{3.5}) \qquad (5.7)$$

The stress intensity factor for welded joints is calculated by following equation [121]:

$$K = \frac{1}{\sqrt{2\pi c}}\int_0^c \sigma(u)\sum_{i=1}^{5} F_i\left(1 - \frac{u}{c}\right)^{i-\frac{3}{2}} du \qquad (5.8)$$

Crack geometry dimensional limit: $0 < c/t \leq 0.9$

where u is the distance from the crack initiation point along a parallel direction of the crack,

$\sigma(u)$ is the stress distribution, and F_i is the coefficients which related with the crack depth c and the plate thickness t (Appendix 4). For the fracture of the specimen, we assumed the number of cycle which the maximum value of the stress intensity factor K_{max} reaches the fracture toughness of value of 160 MPa$\sqrt{m}$ [66].

The total fatigue life to failure N_f is described as follows:

$$N_f = N_c + N_p \qquad (5.9)$$

where N_c is the fatigue crack initiation life, and N_p is the fatigue crack propagation life.

5.4 Finite element analysis results

Figure 5.8 shows the longitudinal welding residual stress distributions which was obtained by the welding simulation. The high tensile stress around weld toe was observed. These tendency is slightly strong with an increase in the main plate thickness.

Figure 5.9 shows the cyclic stress-strain response at the maximum SWT parameter point, which is the critical area for the fatigue crack initiation, as a representative cyclic stress-strain response. The first cycle stress-strain response indicated a nonlinearity because of a plastic deformation. Then, the second cycle stress-strain response indicated a complete linearity. In the range of this investigation, the stress-strain response under cyclic fatigue loading indicates the elastic shakedown after applying the first fatigue loading cycle. The stress-strain behaviors of three type specimens are different respectively.

Figure 5.10 shows the longitudinal stress distribution $\sigma_x(y)$ from the weld toe under

fatigue loading after the first loading cycle. These longitudinal stress distribution $\sigma_x(y)$ were used to calculate the stress intensity factor to estimate the fatigue crack propagation life.

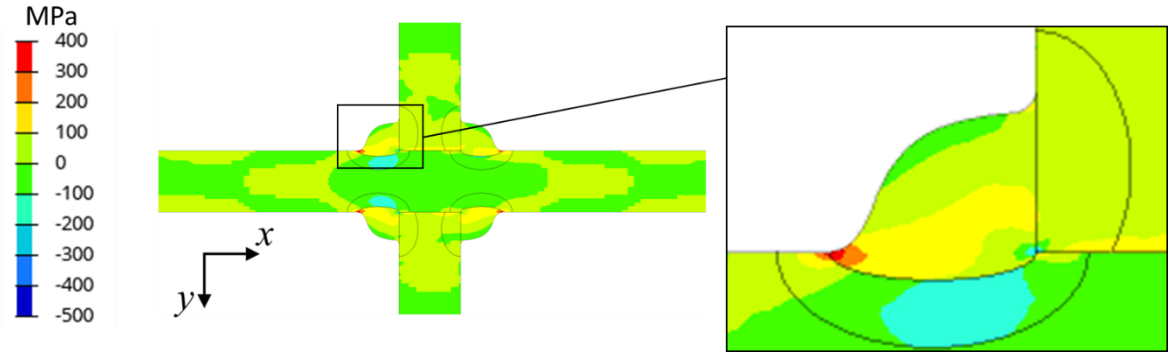

(a) t = 10 mm.

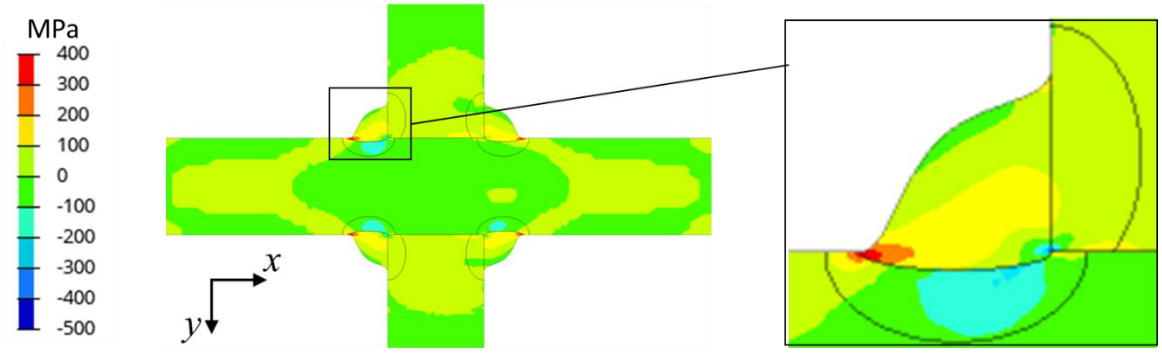

(b) t = 16 mm.

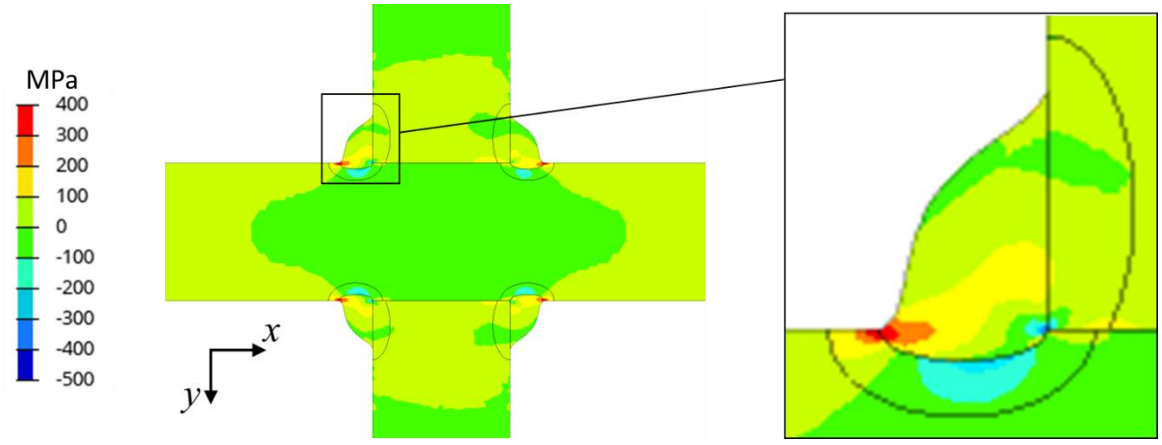

(c) t = 22 mm.

Fig. 5.8. Contour of longitudinal welding residual stress.

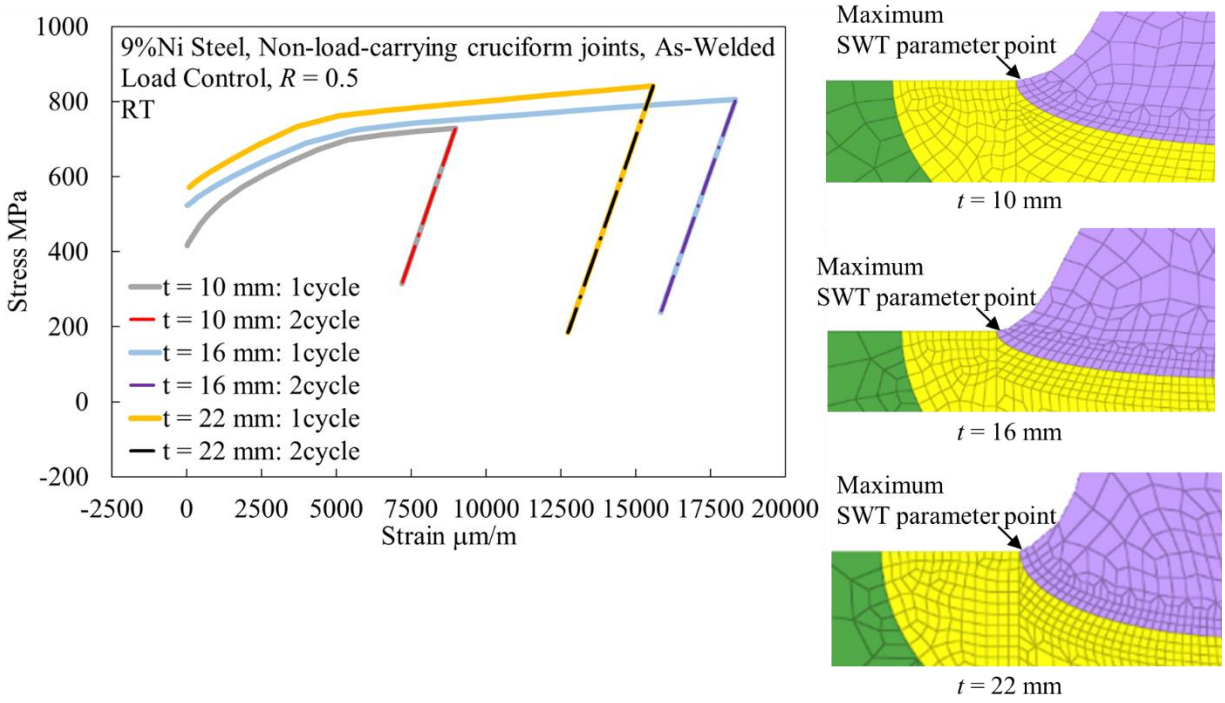

Fig. 5.9. Cyclic stress-strain response at maximum SWT parameter point.

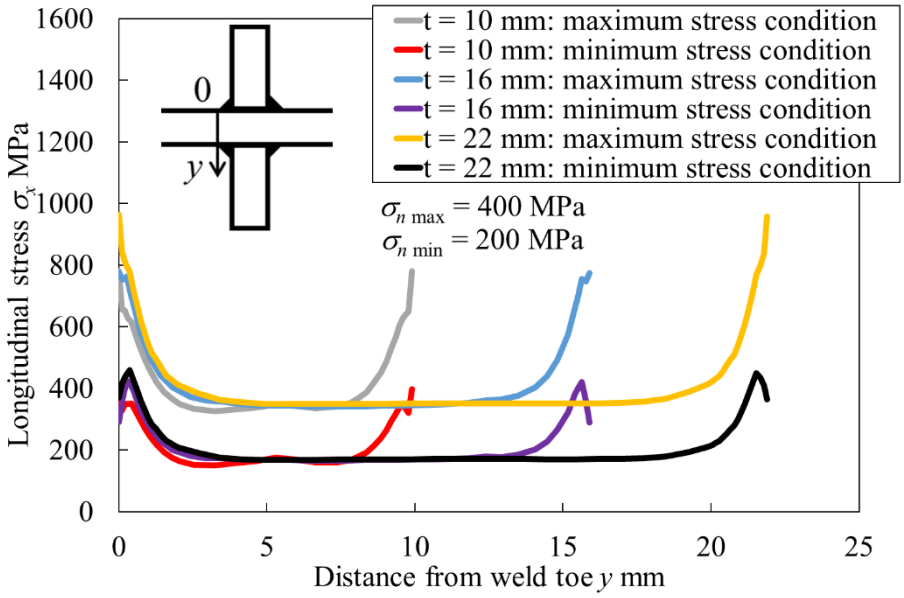

Fig. 5.10. Longitudinal stress distribution under fatigue loading.

5.5 Fatigue life prediction results

Figure 5.11 shows prediction results of S-N curves for non-load-carrying cruciform joints. Figure 5.12 shows comparisons of fatigue strength at 10^5 cycle and 2×10^6 cycle between experimental results and prediction result. These results indicate that the prediction results are good agreement with the experimental results, regardless main plate thickness and bead profile. To evaluate quantitatively accuracy of the prediction results of fatigue life, comparisons between the prediction fatigue life and observed fatigue life were conducted, as shown in Fig. 5.13. Figure 5.13 also includes results of butt welded joints in chapter 4. Observed fatigue life are almost distributed within a band of factor of two against fatigue life prediction results based on the proposed method.

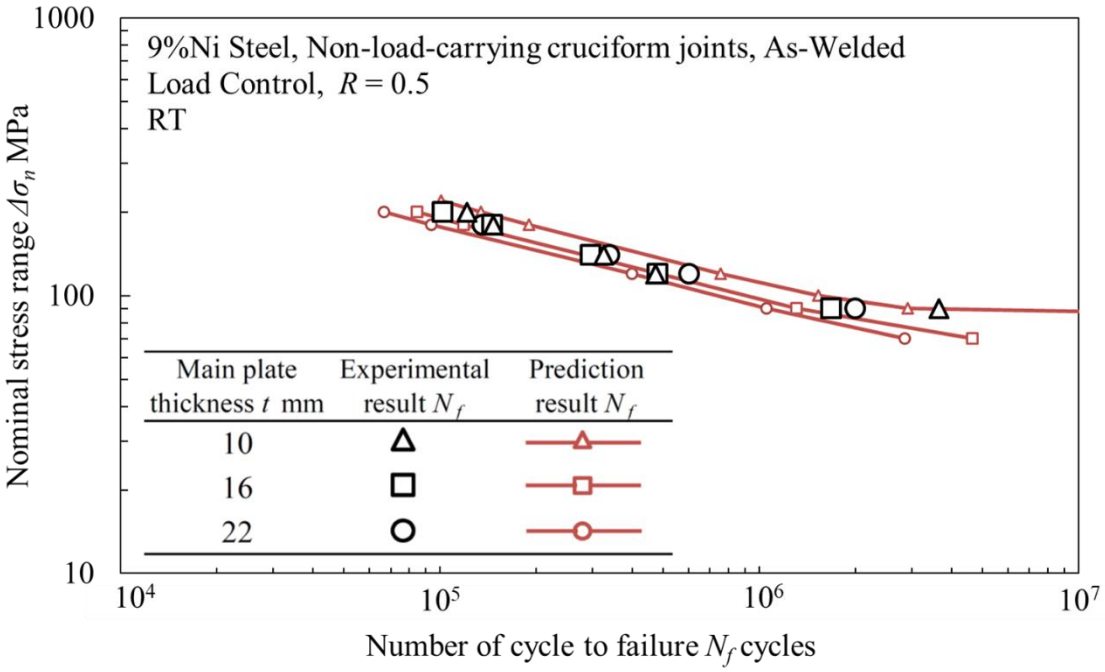

Fig. 5.11. Predicted S-N curve.

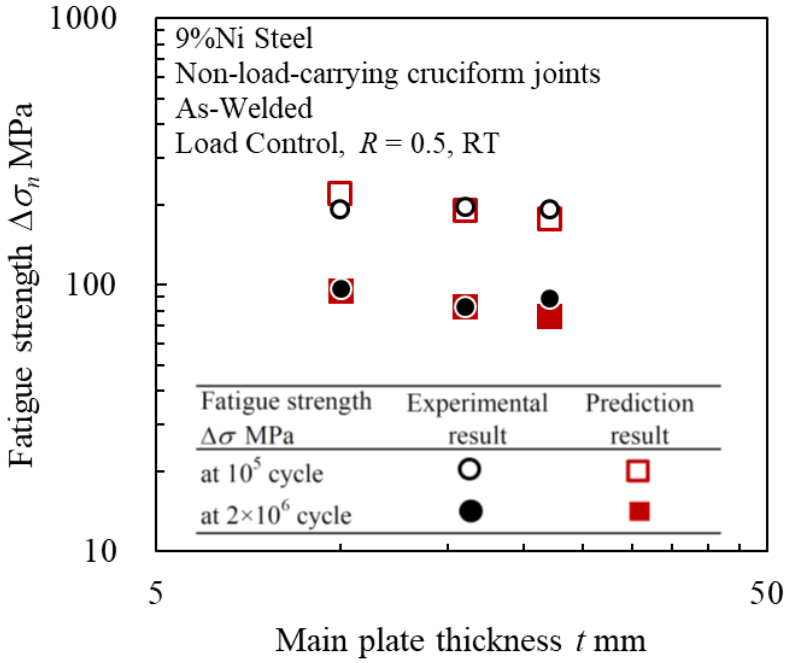

Fig. 5.12. Relationship between fatigue strength and main plate thickness.

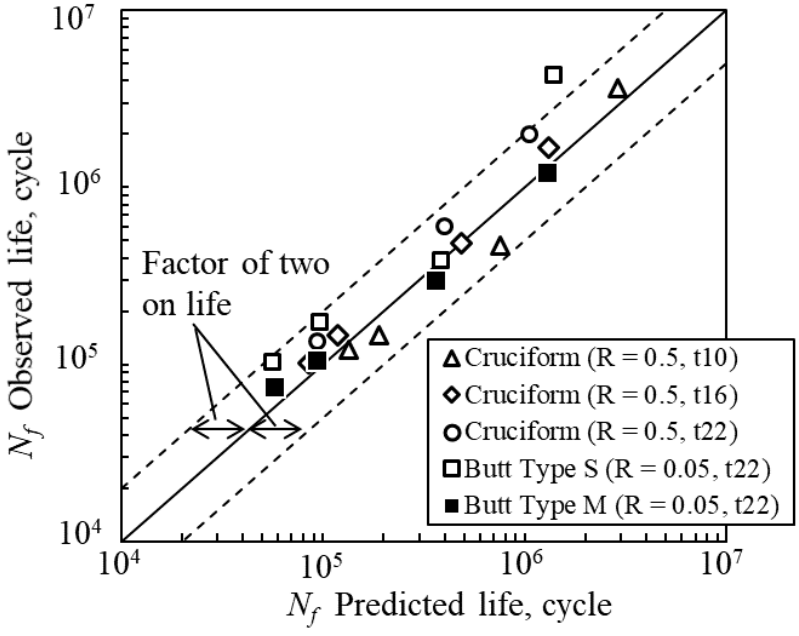

Fig. 5.13. Comparison of fatigue life between prediction and observation.

5.6 Discussion

5.6.1 FE analysis results

In results of welding simulations, the residual tensile stress around weld toe was slightly high with an increase in the main plate thickness, as mentioned in section 5.4. The reason of this tendency was surmised the effect of stiffness of main plate and attached plate.

In results of structure analysis, the stress-strain behaviors of three type specimens are different respectively. The major reason of this is an increase of local stress at weld toe with an increase main plate thickness, as described in chapter 3. Simultaneously, the difference of the welding residual stress distribution affects the stress-strain behavior, because the welding residual stress distribution is the initial condition for the structure analysis.

5.6.2 Fatigue life prediction

To obtain further information on the influence of main plate thickness for fatigue life of non-load-carrying welded joints, detail data analysis on fatigue life prediction were performed.

Figure 5.14 shows the relationships between nominal stress range and the SWT parameter. The SWT parameter clearly shows an increase with an increase in stress range. This tendency is strongly appear for thicker main plate, because local stress increase with an increase main plate thickness.

Figure 5.15 shows the predicted crack propagation rate at initial fatigue crack depth. Due to the effect of the threshold stress intensity factor, the predicted crack propagation rate at initial crack are sharply dropped from less than about $\Delta\sigma$ = 100 MPa. Main plate thickness has a strong influence on this trend.

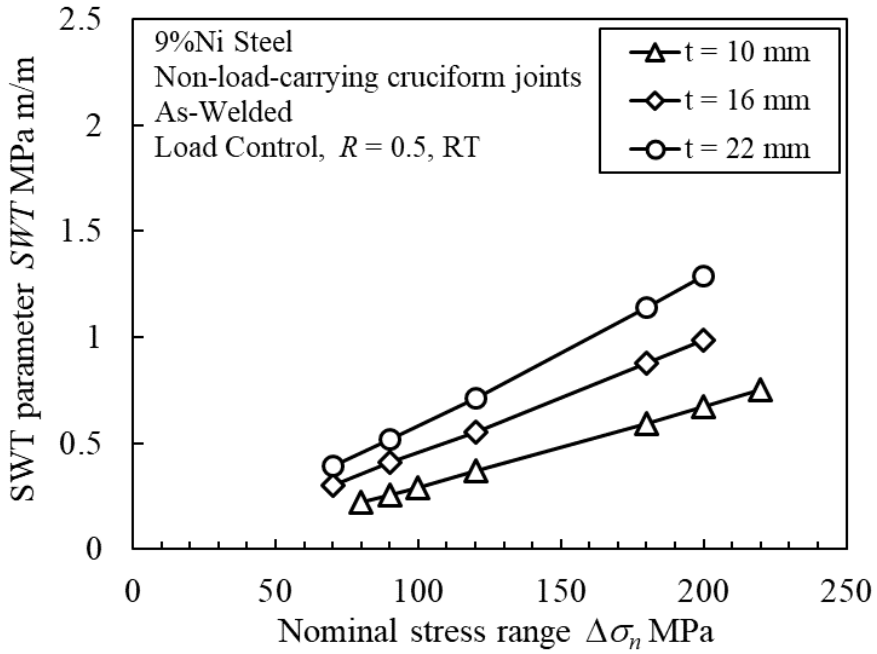

Fig. 5.14. Relationships between nominal stress range and SWT parameter.

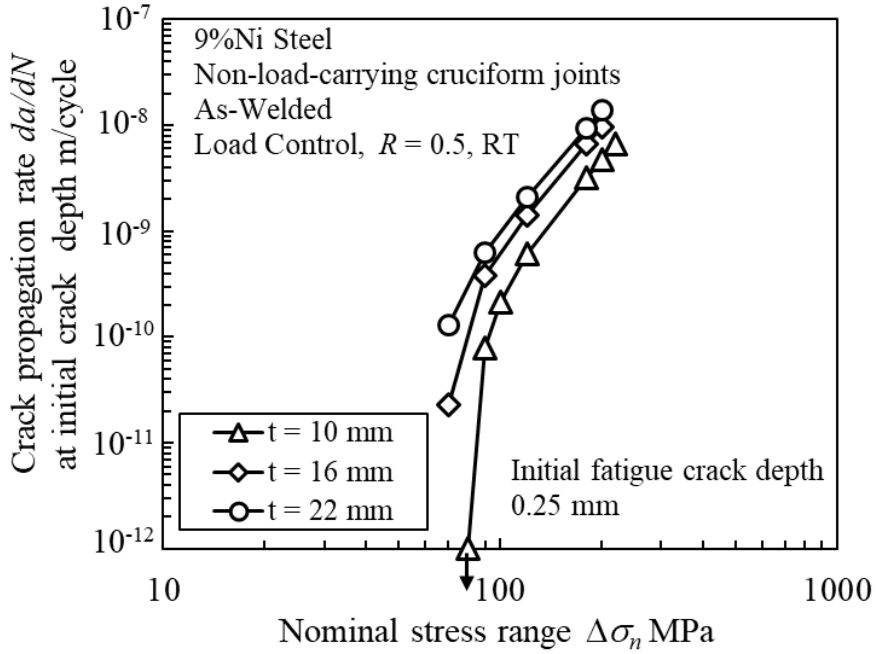

Fig. 5.15. Predicted crack propagation rate at initial fatigue crack depth.

5.7 Conclusions

In this chapter, fatigue test and prediction of fatigue life for 9 % Ni steel cruciform welded joints were conducted to reveal fatigue behavior and fatigue life of 9 % Ni steel cruciform welded joints. The results obtained can be summarized as follow:

- Welding simulation and structural analysis revealed the stress-strain behavior under cyclic fatigue loading of three kinds of non-load-carrying cruciform welded joints with different main plate thickness and bead profile.
- The fatigue life prediction method, which is proposed in chapter 4, can successfully predict the fatigue life for 9 % Ni steel cruciform welded joints, regardless main plate thickness and bead profile.
- It is presented that main plate thickness and bead profile affect the fatigue crack initiation life and fatigue crack propagation life for 9 % Ni steel cruciform welded joints.

Chapter 6 Conclusion

This chapter summarized this thesis and identifies the major contribution by this study. Directions for future work are presented at the end of this chapter.

6.1 Conclusions and contributions

The thickness effect of hot spot S-N curves for aluminum welded joints

- The fatigue test results obviously indicated the thickness effect on aluminum welded joints up to t = 25 mm.
- The hot spot design S-N curve based on the research work on the thickness effect was proposed.
- The proposed hot spot S-N curves provide a roughly suitable assessment for welded structures.

The geometric effect function based on the relative stress gradient

- This study clarified that the relative stress gradient of welded joints depended only on weld toe radius, regardless of welded joint and loading type, based on results of stress analyses.
- Based on analysis results, we derived the geometric effect function described by the stress concentration factor and the function of weld toe radius.
- Fatigue test data were distributed around prediction results using the proposed geometric effect function.
- Parametric studies using the proposed geometric function revealed the trend for geometric effect on fatigue strength for cruciform joints, Tee welded joints, and out-of-plane gusset,

respectively. Not only main plate thickness, but attached plate thickness, weld toe radius, and weld leg length also affected the fatigue strength of welded joints.

- Based on the proposed geometric function, it was clarified that the bending correction coefficient had been affected by the geometries of welded joints excluding weld toe radius. The bending correction coefficient for non-load-carrying cruciform welded joints was also indicated by parametric studies.

Fatigue life prediction method for welded joints considering the geometric effect, material properties, and mean stress effect

- The fatigue life prediction method of 9% Ni steel welded joints, which is considered the geometric effect, difference of cyclic stress-strain properties between parent material, HAZ, and weld metal, and the mean stress effect by welding residual stress and applied stress, were proposed
- This study combined the finite element analyses, which are the welding simulation and the nonlinear structural analysis applied fatigue loading, and the estimation method of the fatigue crack initiation and the fatigue crack propagation, to predict the fatigue life for welded joints. The finite element analysis models were made from the real surface geometry of the welded joints, to consider the geometric effects.
- The unified strain-crack initiation life curve, regardless of the material type and the static strength, were proposed. In the fatigue crack initiation life of welded joints, the proposed strain-crack initiation life curve was combined the mean stress correction approach.
- The fatigue crack propagation properties of 9% Ni steel, which can consider the mean stress effect, were summarized.

- The proposed fatigue life prediction method for welded joints can successfully predict the fatigue life of 9% Ni steel butt welded joints.

Fatigue behavior and fatigue life of 9 % Ni steel cruciform welded joints

- Welding simulation and structural analysis revealed the stress-strain behavior under cyclic fatigue loading of three kinds of non-load-carrying cruciform welded joints with different main plate thickness and bead profile.
- The fatigue life prediction method, which is proposed in chapter 4, can successfully predict the fatigue life for 9 % Ni steel cruciform welded joints, regardless main plate thickness and bead profile.

6.2 Recommendations

As the future work, the following issue need to be investigated.

- To appropriately assess the fatigue strength of real welded structures, more experimental or analytical work is necessary.
- The proposed methods of prediction of fatigue life for 9% Ni steel welded joints has possibility that can be applied to other welded joint type and other materials. In order to that, further experimental and analytical work are necessary to test the validity of the proposed methods.

References

[1] ABS. Guide for Building and Classing for Liquefied Gas Carriers with Independent Tanks. 2019.

[2] Lloyd's Register. Guidance notes for liquefied gas carriers adopting IMO Type B independent tanks primarily constructed of plane surfaces. 2012.

[3] Kawasaki heavy industries Ltd. https://www.khi.co.jp/stories/articles/vol55/ (accessed 2020-6-23).

[4] Kawasaki heavy industries Ltd. https://www.khi.co.jp/mobility/marine/ships/lng.html (accessed 2020-6-23).

[5] Tom O. Kleppestø. LNG as marine fuel, Status and trends in Norway. 2019.

[6] Kawasaki heavy industries Ltd. https://global.kawasaki.com/en/corp/newsroom/news/detail/20120118_2.html (accessed 2020-6-23).

[7] Kawasaki heavy industries Ltd. https://www.khi.co.jp/news/detail/2016_08_24_01.html (accessed 2020-6-23).

[8] DNV, G. L. DNVGL-CG-0129: Fatigue Assessment of Ship Structures. 2018.

[9] DNV, G. L. DNVGL-RP-C203: Fatigue Design of Offshore Steel Structures, no. DNVGL-RPC203, 2016.

[10] IIW (2016) Recommendations for Fatigue Design of Welded Joints and Components. IIW document IIW-2259-15.

[11] European committee for standardization (2005) BS EN 1993-1-9: 2007 Eurocode 3: Design of steel structures – Part 1-9: Fatigue

[12] European committee for standardization (2007) BS EN 1999-1-3: 2007 Eurocode 9: Design of aluminium structures – Part 1-3: Structures susceptible to fatigue.

[13] STANDARD, British. BS7608-1993 Fatigue design and assessment of steel structures. 1999.

[14] Japanese society of steel construction (2012). Fatigue design recommendations for steel structures. (in Japanese)

[15] Tveiten B W, Xiaozhi W, Berge S (2007) Fatigue Assessment of Aluminum Ship Details by Hot-Spot Stress Approach. ABS Technical Papers : 255-271.

[16] Maddox S J (1995) Scale Effect in Fatigue of Fillet Welded Aluminum Alloys. 6th Int Conf on Al. Weldments.

[17] Lee JS, You WH, Yoo CH, Kim KS and Kim Y. An experimental study on fatigue performance of cryogenic metallic materials for IMO type B tank. International Journal of Naval Architecture and Ocean Engineering 2013; 5(4): 580-597.

[18] Gioielli PC and Zettlemoyer N. SN fatigue tests of 9% nickel steel weldments. In The Seventeenth International Offshore and Polar Engineering Conference 2007. International Society of Offshore and Polar Engineers.

[19] Gioielli PC. and Zettlemoyer N. Cryogenic fatigue tests of 9% nickel steel weldments. In The Eighteenth International Offshore and Polar Engineering Conference 2008. International Society of Offshore and Polar Engineers.

[20] Tsunenari T. Influence of welding distortion for fatigue strength –Report 1: Butt welded joints of 9% Ni steel-. Preprints of the National Meeting of JWS 1973; 13: 286-287 (in Japanese).

[21] Kishimoto K, Hukuoka, and Kamio Z. Fatigue strength for butt welded joints of 9% Ni steel with welding defects. Preprints of the National Meeting of JWS 1976; 18: 274-275 (in Japanese).

[22] Kamata T. and Morita H. Fatigue Properties of 9% Ni Steel and Its Welded Joint at Room and Liquid Nitrogen Temperatures. Journal of the Society of Materials Science, Japan 1980; 29(323): 835–841.

[23] Gurney TR (1977) Theoretical analysis of the influence of toe defects on the fatigue strength of fillet welded joints. Welding Institute, Cambridge, UK.

[24] Ribeiro AS, de Jesus AM, Feup I (2011) Fatigue behaviour of welded joints made of 6061-T651 aluminium alloy. Aluminium Alloys, Theory and Applications, ed. T. Kvackaj, 135-156.

[25] Bloem C, Salvador M, Amigó V, Vergara M (2011) Aluminium 7020 alloy and its welding fatigue behaviour. Aluminium alloys, theory and applications. Rijeka, Croatia: InTech, 115-134.

[26] Coughlin R, Walbridge S (2012). Fatigue testing and analysis of aluminum welds under in-service highway bridge loading conditions. Journal of Bridge Engineering, 17(3), 409-419.

[27] Partanen T, Niemi E (1999) Hot Spot S-N Curves Based on Fatigue Tests of Small MIG-Welded Aluminum Specimens. Welding in the World 43 (1) : 16-22.

[28] Zamzami I A, Susmel L (2017) On the Accuracy of Nominal, Structural, and Local Stress Based Approaches in Designing Aluminium Welded Joints against Fatigue. Int J Fatigue 101 : 137-158.

[29] Johnston GO. The influence of plate thickness on the fatigue strength of welded joints. Weld Inst Report 3549/3/78 (unpublished);1978.

[30] Gurney TR. Some Comments on Fatigue Design rules for offshore structures, Integrity of

Offshore Structures, Glasgow;1981.

[31] Japan Ship Technology Research Association. Study on Fatigue Design Method and Quality of Welding for Offshore structures;1991.

[32] Yagi J, Machida S, Tomita Y, Matoba M and Soya I. Influencing Factors on Thickness Effect of Fatigue Strength in As-welded Joints for Steel Structures. Journal of the Society of Naval Architects of Japan 1991;169:289-299.

[33] Yagi J, Machida S, Tomita Y, Matoba M and Soya I. Thickness Effect Criterion for Fatigue Evaluation of Welded Steel Structures. Journal of the Society of Naval Architects of Japan 1991;169:301-309.

[34] Seto A, Soya I and Tanaka Y. Enhancement and Thickness Effect of Fatigue Strength in Steel Joints with Improved Weld. Journal of the Society of Naval Architects of Japan 1992;172:617-626.

[35] Shiratsuchi T, Izumi N, Imai T, Nishimoto S, Hasegawa Y, and Osawa N. Study on Hot Spot SN Curve for Welded Aluminum Joints With Various Plate Thicknesses. In The 28th International Ocean and Polar Engineering Conference. Sapporo:Japan;2018.

[36] Gurney TR. The Fatigue Strength of Transverse Fillet Welded joints. Abington Publishing, Cambridge, England; 1991.

[37] Zerbst U, Madia M, Schork B, Hensel J, Kucharczyk P, Ngoula D, and Beckmann C. Fatigue and Fracture of Weldments. In Fatigue and Fracture of Weldments. Springer, Cham. 2019.

[38] Yamamoto N, Mouri M, Okada T, and Mori T. An analytical and experimental study on the thickness effect of fatigue strength in large-scale-welded models. Welding in the World

2014;58(3):329-337.

[39] Tatsuta K, Okada T, and Kawamura Y. A study on the size effect of cruciform joint for fatigue strength subjected to bending and axial stress. Conference proceedings, the Japan Society of Naval Architects and Ocean Engineers 2016;22:457-462.

[40] Lawrence FV, Burk JD, Mattos RJ, and Higashida Y. Estimating the fatigue crack initiation life of welds. In Fatigue testing of weldments. ASTM International. 1978: 134-158.

[41] Usami S, Kimoto H and Kusumoto S. Cyclic Strain and Fatigue Strength at the Toes of Heavy Welded Joint: Fracture Mechanics Analysis of Fatigue Strength of Welded Joints, 3rd Report. Transactions of the Japan Welding Society 1978; 9(2): 118-127.

[42] Teng TL and Chang PH. Effect of residual stresses on fatigue crack initiation life for butt-welded joints. Journal of Materials Processing Technology 2004; 145(3): 325-335.

[43] Smith KN, Watson P and Topper TH. A Stress-strain Function for the Fatigue of Materials. Int. J. Mater. 1970; 5(4): 767-778.

[44] Manson SS and Halford GR. Practical implementation of the double linear damage rule and damage curve approach for treating cumulative fatigue damage. International journal of fracture 1981; 17(2): 169-192.

[45] Morrow J. Fatigue Design Handbook, Advances in Engineering, Society of Automotive Engineers, Warrendale, PA, 1968: 21–29.

[46] Levieil B, Bridier F, Doudard C, Thevenet D, Calloch S and Ezanno A. Numerical simulation of low-cycle fatigue behavior of welded joints for naval applications: influence of residual stresses. Welding in the World 2017; 61(3): 551-561.

[47] Ince A, and Glinka G. A modification of Morrow and Smith-Watson-Topper mean stress correction models. Fatigue & Fracture of Engineering Materials & Structures 2011; 34(11): 854-867.

[48] Ladinek M, Niederwanger A, Lang R, Schmid J, Timmers R, and Lener G. The strain-life approach applied to welded joints: Considering the real weld geometry. Journal of Constructional Steel Research 2018; 148: 180-188.

[49] Hiraide T, Igi S, Handa T, Tagawa T, Ikeda R, Morikita K, Fincato R and Tsutsumi S. Effect of heat affected zone microstructure behavior under cyclic loading on fatigue life of weld joint. Quarterly Journal of the Japan Welding Society 2018; 36(2): 145-151.

[50] Tsutsumi S, Kiyokawa Y, Fincato R, Ogino Y, Hirata Y, and Asai S. Assessment of fatigue crack initiation life of joints by using weld poor and cyclic plasticity analysis. Journal of JSCE Division A2 2018; Vol. 74 No. 2: I_337-I_347. (in Japanese)

[51] Maddox, S. An analysis of fatigue cracks in fillet welded joints. International Journal of Fracture 1975; 11(2): 221-243.

[52] Gadallah R, Osawa N, Tanaka S and Tsutsumi S. Critical investigation on the influence of welding heat input and welding residual stress on stress intensity factor and fatigue crack propagation. Engineering Failure Analysis 2018; 89: 200-221.

[53] Itoh Y, Nagata K, Kohsaki Y, Fukaura J and Mori T. Initiation and Propagation Behaviors of Fatigue Cracks at the Toes of Butt Welded Joints. Journal of the Society of Materials Science, Japan 1984; 33(368): 578–583.

[54] Zerbst U, Madia M, Schork B, Hensel J, Kucharczyk P, Ngoula D and Beckmann C. Fatigue and Fracture of Weldments. In Fatigue and Fracture of Weldments. Springer, Cham. 2019.

[55] Tsutsumi S, Morita K, and Fincato R. Numerical study on the effect of weld bead shape on the fatigue crack initiation and propagation lives. Journal of structural engineering 2017; Vol. 63A: 609-618.

[56] Tsutsumi S, Shibata H, and Fincato R. Effect of local materials and geometries of weld joint root on fatigue crack initiation and propagation life. Journal of JSCE Division A2 2019; Vol. 75 No. 2: I_467-I_476. (in Japanese)

[57] Japanese Industrial Standards Committee (2014) JIS H 4000. Aluminium and aluminium alloy sheets, strips and plates.

[58] Japanese Industrial Standards Committee (2009) JIS Z 3232. Aluminium and aluminium alloy welding rods and wires.

[59] Lihavainen V M (1996) Result of Fatigue Strength of MIG-welded Aluminium Extrusions. Fatigue Design 1996, Technical Research Centre of Finland.

[60] Hakuli K (1996) Hot Spot Fatigue Tests of Fillet Welds of AlMgSi1 (6082-T6) Aluminium. Fatigue Design 1996, Technical Research Centre of Finland.

[61] Japan Ship Technology Research Association (1991) Study on Fatigue Design Method and Quality of Welding for Offshore structures (in Japanese).

[62] Davidson CJ, Griffiths JR, Machin AS (2002) The effect of solution heat‐treatment time on the fatigue properties of an Al‐Si‐Mg casting alloy. Fatigue & Fracture of Engineering Materials & Structures, 25(2), 223-230.

[63] Yamada K, Makino T, Kikuchi Y. (1979) Fracture Mechanics Analysis of Fatigue Cracks Emanating from Toe of Fillet Weld. In Proceedings of the Japan Society of Civil Engineers, 292, 1-12.

[64] Yamada K., Albrecht P (1977) Practical aspects of fatigue analysis of a weldment. Fracture 1977, Vol. 2. In Proc. of Fourth International Conference on Fracture, 959-966.

[65] Abtahi A, Albrecht P, Irwin GR (1976) Fatigue of periodically overloaded stiffener detail. Proc. of ASCE, Vol. 102, No. ST11, 2103-2119.

[66] Mann D (1977) LNG Materials and Fluids. National Bureau of Standards, Boulder, Colo. 80302. 1977, Sections paged separately (Book).

[67] Warzynek PA, Carter BJ, Banks-Sills L (2005) The M-integral for computing stress intensity factors in generally anisotropic materials. NASA/CR-2005-214006.

[68] Rice JR (1968) A Path Independent Integral and the Approximate Analysis of Strain Concentration by Notches and Cracks, Journal of Applied Mechanics, 35, 379~386.

[69] ASTM international (2008) ASTM E647-08, Standard Test Method for Measurement of Fatigue Crack Growth Rates.

[70] Hirukawa H, Matsuoka S, Takeuchi E, Nishijima S (1996) Fatigue properties of JIS aluminum alloys for welded structures, Transactions of the Japan Society of Mechanical Engineers (A), 62, 601, 1966-1971.

[71] Takenouchi K (1999) Fatigue strength design of welded aluminum structures, Japan light metal welding association (in Japanese).

[72] Atzori B, Indrio P (1976) Comportamento a fatica dei ciunti saldati in Al Zn Mg1, Al Zn4 Mg1 ED Al Mg Si. University of Bari, Italy, Report No. 76/5.

[73] Jacoby G (1961) Uber das Verhalten von Schweissverbindungen aus Alumininumlegierungen bei Schwingbeansprunchung. Dissertation, Technische Hochschule, Hannover.

[74] Sidhom N, Laamouri A, Fathallah R, Braham C, Lieurade HP (2005) Fatigue strength improvement of 5083 H11 Al-alloy T-welded joints by shot peening: experimental characterization and predictive approach. International journal of fatigue, 27(7), 729-745.

[75] Siebel E, Stieler M. Ungleichformige Spannungsverteilung bei schwingender Beanspruchung. -VDI-Z 1955;97(5):121-126.

[76] Endo K. A study on fatigue strength evaluation method for out-of-plane gusset welded joints failing from weld root. Transactions of Graduate School of engineering and design, Hosei University 2014;vol. 3.

[77] Filippini M. Stress gradient calculations at notches. International Journal of Fatigue 2000;22(5):397-409.

[78] Tsuji I. Estimation of stress concentration factor at weld toe of non-load carrying fillet welded joints. Transactions of the West-Japan Society of Naval Architects 1990;80:241-251.

[79] Iwata T, Niwa T, Tanaka Y, Ando T and Anai Y. Thickness Effect on Fatigue Strength of Welded Joint Improved by HFMI. Quarterly Journal of the Japan Welding Society 2016;34(4):249‐259.

[80] Japanese Society of Steel Construction. Fatigue design recommendations for steel structures 2012.

[81] Pahuta P, JanÍk Z, HyspeckÍ L and Mazanec K. Structure of 9Ni and 9NiMo steels for cryogenic applications. Transactions of the Iron and Steel Institute of Japan 1986; 26(7): 649-654.

[82] Lee JS, You WH, Yoo CH, Kim KS and Kim Y. An experimental study on fatigue performance of cryogenic metallic materials for IMO type B tank. International Journal of Naval Architecture and Ocean Engineering 2013; 5(4): 580-597.

[83] Lee HT, Kim HG, Kim GG and Shin SB. A Study on the Prediction of Welding Distortion of 9% Ni Steel for the Offshore LNG Storage Tank. In The Seventeenth International Offshore and Polar Engineering Conference 2007. International Society of Offshore and Polar Engineers.

[84] Ueda Y, Kim YC, Chen C and Tang YM. Mathematical Treatment of Phase Transformation and Analytical Calculation Method of Restraint Stress-Strain (Welding Mechanics, Strength & Design). Transactions of JWRI 1985; 14(1): 153-162.

[85] Muramatsu Y. Detection of Strain Behavior during Phase-Transformation in Welds by the Laser Speckle Method -Application of the Laser Speckle Method to Strain Measurement in the Welding Process (Report 3)-. Quarterly Journal of the Japan Welding Society 1996; 14(4): 741-747.

[86] Elber W. The significance of fatigue crack closure. In Damage tolerance in aircraft structures. ASTM International 1971.

[87] Y. Ueda, H. Murakawa and N. Ma. Welding Deformation and Residual Stress Prevention, Butterworth-Heinemann, Elsevier, 1st Edition, March 26, 2012, ISBN 978-0-12-394804-5.

[88] Y. Ueda, Y. and T. Yamakawa. Analysis of Thermal Elastic-Plastic Stress and Strain during Welding by Finite Element Method. Trans. of Japan Welding Society 1971; 2(2), 90-100.

[89] Kim YK, Kim YW, and Kim JH. Welding Residual Stress and Strength of Thick 9% Nickel Steel Plate. Journal of the Korea Society for Power System Engineering 2014; 18(4): 85-90.

[90] Zhang M, Zhou Y, Huang C, Chu Q, Zhang W, and Li J. Simulation of Temperature Distribution and Microstructure Evolution in the Molten Pool of GTAW Ti-6Al-4V Alloy. Materials 2018; 11(11), 2288.

[91] Iida K, Matsumoto Y, and Nagai H. Difference in Low Cycle Fatigue Strength by Strain Controlled Axial Load and Deflection Controlled Bending Load. Journal of the Society of Naval Architects of Japan 1975; 137: 307-315.

[92] Landgraf RW, Morrow JD, and Endo T. Determination of the cyclic stress strain curve. J. Mater. 1969; ASTM 4(1): 176–188.

[93] Polák J and Hájek M. Cyclic stress-strain curve evaluation using incremental step test procedure. International journal of fatigue 1991; 13(3): 216-222.

[94] ASTM international. ASTM E606/E606M-19e1, Standard test method for strain-controlled fatigue test. 2019.

[95] Nishikawa H and Furuya Y. Cyclic yield characterization for low-carbon steel with HAZ microstructures. Material Transaction 2019; 60 (2): 207-212.

[96] Nachtigall AJ. Cyclic stress-strain curve determination for D6AC steel by three methods. NASA TM-73815 1977.

[97] Cook TS. Stress-strain behavior of Inconel 718 during low cycle fatigue. Journal of Engineering Materials and Technology 1982; vol. 104:186-191.

[98] Cowles BA, Sims DL, and Warren JR. Evaluation of the cyclic behavior of aircraft turbine disk alloys. NASA CR-159409 1978.

[99] Fournier D, and Pineau A. Low cycle fatigue behavior of Inconel 718 at 298 K and 823 K. Metallurgical Transactions A 1977; 8(7): 1095-1105.

[100] Iida K, Kho Y, and Nagai H. Low Cycle Reversed Bending Fatigue Curves of 9% Ni Steel and Weld Metal. Journal of the Society of Naval Architects of Japan 1975; 138: 403-409.

[101] Iida K. Micro-Crack Initiation Life and Micro-Fractographic Analysis in Strain Cycling Fatigue of a 60 kg/mm^2 High Strength Steel. Journal of the Society of Naval Architects of Japan 1970; 128: a331-a342.

[102] Japan Society of Mechanical Engineers. Book, J. D. Fatigue of Metals IV, Low Cycle Fatigue Strength. 1983, Tokyo.

[103] The Japan welding engineering society, Memorial publication for Prof. Dr. Hiroshi Kihara's 70th birthday, KOKI celebration 1980, Seishinsya Printing Co., Ltd.

[104] Iida K, Minoda K, and Kho, Y. A Study on Low Cycle Fatigue Strength of Aluminum Alloy A 5083 PO Butt Welded Joints. Journal of the Society of Naval Architects of Japan 1978; 144: 371-380.

[105] Paris P and Erdogan F. A critical analysis of crack propagation laws. ASME. J. Basic Eng. 1963; 85(4): 528-533.

[106] Fournier D, and Pineau A. Low cycle fatigue behavior of Inconel 718 at 298 K and 823 K. Metallurgical Transactions A 1977; 8(7): 1095-1105.

[107] Manson SS. Behavior of materials under conditions of thermal stress. NACA TR-1170. 1954.

[108] Basquin OH. The exponential law of endurance tests. Proc Am Soc Testing Mater 1910;10: 625-30.

[109] National Research Institute for Metal (NRIM). Fatigue data sheet Technical document No. 8 Fatigue crack propagation properties for welded joints of structural steels and steels for pressure vessels 1995.

[110] Kim YW et al. An Experimental Study for Fatigue Performance of 7% Nickel Steels for Type B Liquefied Natural Gas Carriers. Journal of Offshore Mechanics and Arctic Engineering 2016; 38(3).

[111] Ikeda K, Aoki M, and Kiuchi A. Study on welded joints of 9% Ni Steel using similar composition metal filler 2nd report. Preprints of the National Meeting of JWS 1980; 26: 10-11 (in Japanese).

[112] Yoon YK, Kim JH, Shim KT, and Kim YK. (2012). Mechanical characteristics of 9% Ni steel welded joint for LNG storage tank at cryogenic. International Journal of Modern Physics: Conference Series 2012; 6: 355-360. World Scientific Publishing Company.

[113] Klesnil M and Lukáš, P. Effect of stress cycle asymmetry on fatigue crack growth. Materials Science and Engineering 1972; 9: 231-240.

[114] Schijve J. Some formulas for the crack opening stress level. Engineering Fracture Mechanics 1981; 14(3): 461-465.

[115] Katoh A; Kurihara M; and Kawahara M. An Expression of Fatigue Crack Propagation Rates under Wide Ranged Stress Ratios. Journal of the Society of Naval Architects of Japan 1983; 153: 336-343.

[116] Kumar R. Review on crack closure for constant amplitude loading in fatigue. Eng. Fract. Mech 1992; 42: 389–400.

[117] Tanaka Y and Soya I. Effects of stress ratio and stress intensity factor range on fatigue crack closure in steel plate. Quarterly journal of the Japan Welding Society 1987; 5(1): 119-126.

[118] Correia JA, De Jesus AM, Moreira PM, and Tavares PJ. Crack closure effects on fatigue crack propagation rates: application of a proposed theoretical model. Advances in Materials Science and Engineering 2016.

[119] Jeong DH, Lee SG, Yoo JY, Lee JS, and Kim S. (2015). Comparative studies on near-threshold fatigue crack propagation behavior of high manganese steels at room and cryogenic temperatures. Materials Characterization 2015; 103: 28-36.

[120] Shipbuilding Res. Assoc. of Japan. Survey report on safety standards of LNG carrier. 1978 (in Japanese).

[121] Wu Xue-Ren. Weight functions and stress intensity factor solutions. 1st ed. Oxford ; New York : Pergamon Press, 1991.

[122] Lloyd’s Register. Fatigue design assessment. Level 3 procedure: Guidance on direct calculations. 2009.

Appendix 1

Table A1.1 shows the dimensions of the welded joints discussed in section 3.3. Definition for dimensions are shown in Fig. 3.3. Table A1.1 also indicates the results of evaluated relative stress gradient χ^* and stress concentration factor α of the welded joints.

Table A1.1 Stress gradient $\chi*$ and stress concentration factor α of welded joints
(a) Cruciform (axial loading).

Load type	Main plate thickness t mm	Attached plate thickness t_p mm	Weld leg length d mm	Flank angle θ degree	Weld toe radius ρ mm	Stress concentration factor α (FEM)	Relative stress gradient χ^* mm^{-1}
Axial	12	12	6.4	45	1	2.56	2.26
	22	12	6.4	45	1	2.78	2.28
	40	12	6.4	45	1	2.82	2.28
	80	12	6.4	45	1	2.81	2.29
	40	22	8.4	45	1	3.23	2.27
	40	40	12	45	1	3.62	2.26
	40	80	20	45	1	3.87	2.25
	22	22	8.4	45	1	3.04	2.26
	80	80	20	45	1	4.48	2.25
	22	12	6.4	45	0.5	3.44	4.18
	22	12	6.4	45	3	2.01	1.00
	40	22	8.4	45	0.5	4.00	4.19
	40	22	8.4	45	3	2.31	1.00

(b) Cruciform (bending loading).

Load type	Main plate thickness t mm	Attached plate thickness t_p mm	Weld leg length d mm	Flank angle θ degree	Weld toe radius ρ mm	Stress concentration factor α (FEM)	Relative stress gradient χ^* mm^{-1}
Bending	12	12	6.4	45	1	2.01	2.34
	22	12	6.4	45	1	2.39	2.30
	40	12	6.4	45	1	2.67	2.29
	80	12	6.4	45	1	2.80	2.28
	40	22	8.4	45	1	2.85	2.28
	40	40	12	45	1	2.93	2.27
	40	80	20	45	1	2.94	2.27
	22	22	8.4	45	1	2.43	2.28
	80	80	20	45	1	3.66	2.25
	22	12	6.4	45	0.5	2.93	4.20
	22	12	6.4	45	3	1.71	0.82
	40	22	8.4	45	0.5	3.53	4.19
	40	22	8.4	45	3	2.03	0.80

(c) Out-of-plane gusset (axial loading).

Load type	Main plate thickness t mm	Main plate width W mm	Attached plate thickness t_p mm	Weld leg length d mm	Gusset length k mm	Flank angle θ degree	Weld toe radius ρ mm	Stress concentration factor α (FEM)	Relative stress gradient χ^* mm^{-1}
Axial	12	100	12	6.4	120	45	1	3.90	1.87
	22	100	12	6.4	120	45	1	4.35	1.89
	40	100	12	6.4	120	45	1	4.64	1.89
	80	100	12	6.4	120	45	1	4.82	1.89
	22	150	12	6.4	120	45	1	4.43	1.89
	22	200	12	6.4	120	45	1	4.49	1.89
	22	250	12	6.4	120	45	1	4.51	1.88
	40	150	12	6.4	120	45	1	4.70	1.89
	40	200	12	6.4	120	45	1	4.72	1.89
	40	250	12	6.4	120	45	1	4.74	1.89
	80	150	12	6.4	120	45	1	4.83	1.89
	80	200	12	6.4	120	45	1	4.87	1.88
	80	250	12	6.4	120	45	1	4.86	1.89
	22	100	12	6.4	200	45	1	4.69	1.88
	22	100	12	6.4	300	45	1	4.80	1.88
	22	100	12	6.4	400	45	1	4.81	1.88
	40	100	12	6.4	200	45	1	5.10	1.88
	40	100	12	6.4	300	45	1	5.25	1.89
	40	100	12	6.4	400	45	1	5.28	1.88
	80	100	12	6.4	200	45	1	5.37	1.89
	80	100	12	6.4	300	45	1	5.59	1.89
	80	100	12	6.4	400	45	1	5.63	1.89
	10	120	16	8	160	45	1	3.7	2.22
	10	120	16	7.5	160	45	5.4	2.38	0.38
	10	120	16	15.2	160	45	5	2.29	0.40

(d) L-type structural model.

Load type	Main plate thickness t mm	Weld leg length d mm	Weld leg length on attached plate d_p mm	Flank angle θ degree	Weld toe radius ρ mm	Relative stress gradient χ^* mm^{-1}
Bending	22.5	13.35	17.18	52.2	1.81	1.16
	40.5	13.32	19.14	55.4	1.48	1.59
	81.0	13.23	21.49	58.4	1.63	1.29

(e) I-type structural model.

Load type	Main plate thickness t mm	Weld leg length d mm	Weld leg length on attached plate d_p mm	Flank angle θ degree	Weld toe radius ρ mm	Relative stress gradient χ^* mm^{-1}
Bending	22.5	10.52	6.98	33.5	0.98	2.77
	40.5	10.31	7.57	36.3	0.84	3.15
	81	9.76	7.40	37.1	0.98	2.73

Appendix 2

The formula for calculation of stress concentration factor α at weld toe, as reported by Tsuji [78], is described as follows:

For non-load-carrying cruciform joints that apply axial loading:

$$\alpha = 1 + \left\{1.348 + 0.397\ln\left(\frac{t_p + 2d}{t}\right)\right\} Q^{0.467} f_\theta \qquad \text{(A2.1)}$$

For Tee joints that apply bending loading:

$$\alpha = 1 + \left\{0.629 + 0.058\ln\left(\frac{t_p + 2d}{t}\right)\right\} \left(\frac{\rho}{t}\right)^{-0.431} \tanh\left(\frac{6d_p}{t}\right) \cdot f_\theta \qquad \text{(A2.2)}$$

$$Q = \frac{1}{2.8\left(\frac{V}{t}\right) - 2}\left(\frac{d_p}{\rho}\right) \qquad \text{(A2.3)}$$

$$f_\theta = \frac{1 - \exp\left(-0.9\sqrt{\frac{V}{2d_p}} \cdot \theta\right)}{1 - \exp\left(-0.9\sqrt{\frac{V}{2d_p}} \cdot \frac{\pi}{2}\right)} \qquad \text{(A2.4)}$$

$V = t + 2d_p$ for cruciform joints

$V = t + d_p$ for Tee joints

Fig. A2.1 presents definitions for the symbols employed in Eqs. (A2.1)–(A2.4).

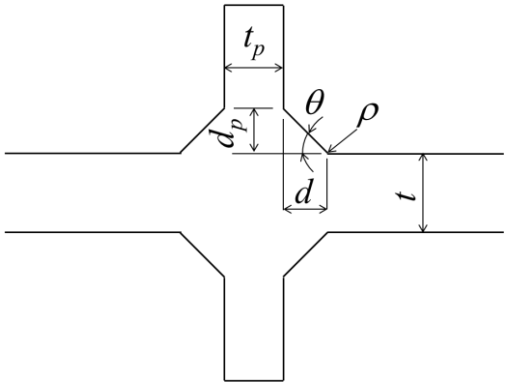

Fig. A2.1. Symbol definitions.

Appendix 3

Table A3.1 presents the joint types and dimensions of welded joints, and load types for cruciform welded joints and Tee welded joints discussed in section 3.6. The definitions of dimensions for cruciform welded joints are shown in Fig. 3.9. Dimension definitions for Tee welded joints are the same as for cruciform welded joints. Table A3.1 also shows thickness correction exponent n.

Table 3.1 Dimensions and thickness correction exponent of welded joints.

Joint type	Series	Load type	Main plate thickness t mm	Attached plate thickness t_p mm	Weld leg length d mm	Flank angle θ degree	Weld toe radius ρ mm	Thickness correction exponent n
Cruciform	CT-1	Axial	10-100	t	t/2	45	0.5	0.36
							1.0	0.33
							1.5	0.32
							3.0	0.28
	CT-2	Axial	10-100	t	5	45	0.5	0.20
							1.0	0.18
							1.5	0.17
							3.0	0.15
	CT-3	Axial	10-100	10	5	45	0.5	-
							1.0	-
							1.5	-
							3.0	-
T-joint	TB-1	Bending	10-100	t	t/2	45	0.5	0.32
							1.0	0.30
							1.5	0.28
							3.0	0.25
	TB-2	Bending	10-100	t	5	45	0.5	-
							1.0	-
							1.5	-
							3.0	-
	TB-3	Bending	10-100	10	5	45	0.5	-
							1.0	-
							1.5	-
							3.0	-

Appendix 4

Table A4.1 shows coefficients F_i of Eq. (4.19).

Table A4.1 Coefficients F_i of Eq. (4.19).

c/t	F_1	F_2	F_3	F_4	F_5
0.01	2.000	0.977	1.142	0.350	0.091
0.05	2.000	1.093	1.151	0.366	0.082
0.10	2.000	1.419	1.138	0.355	0.076
0.15	2.000	1.906	1.156	0.343	0.069
0.20	2.000	2.537	1.238	0.348	0.056
0.25	2.000	3.311	1.403	0.370	0.039
0.30	2.000	4.238	1.680	0.410	0.019
0.35	2.000	5.337	2.119	0.478	0.005
0.40	2.000	6.636	2.805	0.611	0.039
0.45	2.000	8.177	3.867	0.867	0.102
0.50	2.000	10.02	5.500	1.340	0.218
0.55	2.000	12.26	8.005	2.174	0.425
0.60	2.000	15.04	11.88	3.607	0.786
0.65	2.000	18.56	18.00	6.078	1.421
0.70	2.000	23.18	28.03	10.50	2.587
0.75	2.000	29.52	45.51	18.93	4.883
0.80	2.000	38.81	78.75	36.60	9.871
0.85	2.000	53.85	151.2	79.01	22.27
0.90	2.000	82.69	351.0	207.1	60.86

Publications related to this Thesis

Peer-review publications

1. Shiratsuchi, T., Izumi, N., Imai, T., Nishimoto, S., Hasegawa, Y., and Osawa, N. (2018, July). Study on Hot Spot SN Curve for Welded Aluminum Joints with Various Plate Thicknesses. In The 28th International Ocean and Polar Engineering Conference. International Society of Offshore and Polar Engineers.
2. Shiratsuchi, T., and Osawa, N. (2020). Investigation of thickness and bead profile effects on fatigue strength of welded joints based on relative stress gradient. International Journal of Fatigue, 134, 105520.
3. Shiratsuchi, T., Izumi, N., Imai, T., Nishimoto, S., Hasegawa, Y., and Osawa, N. (2020). The thickness effect of Hot Spot S-N curves for welded aluminum joints. Welding in the world. https://doi.org/10.1007/s40194-020-00936-w.
4. Shiratsuchi, T., and Osawa, N. (2020). Fatigue life prediction for 9 % Ni steel butt welded joints. International Journal of Fatigue.

Acknowledgments

First of all, I would like to express my utmost gratitude to Professor Naoki Osawa, for giving me the opportunity to join the laboratory of Ocean Material Engineering of the Department of Naval Architecture and Ocean Engineering of Osaka University, also for all the experience and knowledge he offered me during my research.

I would like to express my sincere gratitude to Professor Ninshu Ma, Professor Masahiko Fujikubo and Professor Seiichiro Tsutsumi for participating as members of the dissertation committee and providing corrections and valuable suggestions to improve the quality of this work.

I am deeply grateful to Dr. Hiroshi Nakatani, General Manager Corporate Technology Division of Kawasaki heavy industries, Ltd., and Mr. Takumi Kawasaki, General Manager Technical Institute of Kawasaki heavy industries, Ltd., for giving me the opportunity to admit Ocean Material Engineering of the Department of Naval Architecture and Ocean Engineering of Osaka University.

Finally, I would like to express the deepest appreciation to the members of Ship & Offshore Structure Company of Kawasaki Heavy Industries, Ltd., and the members of Strength research department of Kawasaki Heavy Industries, Ltd., for the support and help in realizing this research work.